Title
First-principles studies of electron-phonon induced superconductivity and beyond

Author
Bazhirov, Timur T.

Publication Date
2013

Peer reviewed|Thesis/dissertation

First-principles studies of electron-phonon induced superconductivity and beyond

Timur T. Bazhirov

A dissertation submitted in partial satisfaction of the requirements for the degree of

Doctor of Philosophy

in
Physics

in the
Graduate Division
of the
University of California at Berkeley

Committee in charge:

Professor Marvin L. Cohen, chair
Professor John Clarke
Professor Norman E. Phillips

Fall 2013

Abstract

First-principles studies of electron-phonon induced superconductivity and beyond

by

Timur T. Bazhirov

Doctor of Philosophy in Physics

University of California, Berkeley

Professor Marvin L. Cohen, Chair

The prospect of precisely predicting the behavior of solids entirely by means of theory and computations is enticing. This dissertation presents the results of the application of the first-principles physical approaches to study superconductivity in a set of materials.

In the first chapter a brief overview of the key concepts used in this manuscript in given. A description of the theoretical methodology and the key computational techniques used in this work constitute the subject of chapter 2. Studies of class-I/conventional and class-II/non-conventional superconducting materials are contained in chapters 3 and 4 respectively. In particular, precise calculations of the electron-phonon interaction and superconducting parameters of elemental lithium at ambient conditions and under pressure, and lithium-intercalated borocarbide compounds are presented. In addition, the application of first-principle techniques to study iron selenide in multiple configurations is given.

A discussion of superconductivity in complex oxides is presented in chapter 5 with emphasis on the importance of oxygen octahedra tilts. And, finally, concluding remarks from the author are given in the last chapter.

To my family

Acknowledgements

I would like to acknowledge the great support coming from my advisor, my dearest mother, my family and friends at Berkeley and elsewhere. All members of the Cohen/Louie research group were always helpful and supportive, and this work would have been impossible without their direct or indirect participation.

Contents

Chapter 1

Introduction

Superconductivity is a macroscopic physical phenomenon defined by the observance of zero electrical resistance in certain materials when cooled below a characteristic critical temperature T_c. Ever since its discovery in 1911 by Kamerling-Onnes [1], superconductivity attracted much attention from scholars, yet even a century later there are still many unanswered questions about the nature of this phenomenon. The purpose of this thesis is to give several examples of how superconductivity can be studied theoretically on the basis of the first-principles studies.

First-principles studies characterize a theoretical scientific field where conclusions are made on the basis of established scientific facts directly, without any assumptions, empirical models or fitting parameters. Starting from Bloch's pioneering works on the electronic band theory [2] and Hartree's attempts to describe the wave mechanics of the atom [3], numerous techniques were developed to achieve accurate physical descriptions of the electronic structure of materials from the first principles.

Materials under consideration in this work include simple metals, borocarbides, complex oxides, and iron compounds. The specific motivation for choosing these materials is described later inside each corresponding chapter. One thing that unites all studied cases: a complete theoretical description of superconductivity has not yet been achieved for these materials. The materials chosen here are simple enough for a fully first-principle study to be computationally feasible at the time of this writing.

Much of the first-principles techniques applied in this work is based on the density functional theory [4]. Discussion of this methodology in given chapter 2.

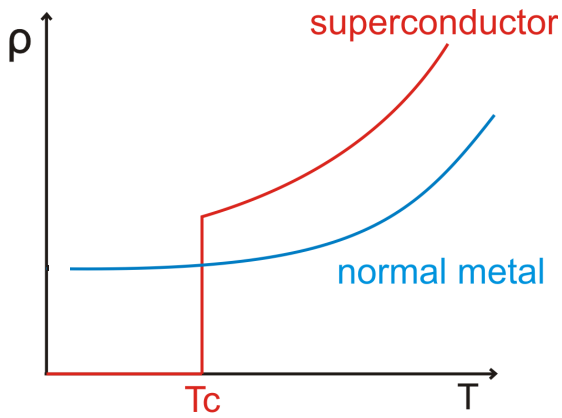

Figure 1.1: Schematic plot of the temperature dependence of electrical resistance for normal metals and superconductors. T_c denotes the critical temperature of a superconducting transition.

The manuscript is organized as follows: the "introduction" section gives a brief overview of the key concepts considered in this work this work, a description of the theoretical methodology, and the key computational techniques used in this work are given in "models and methods", studies of class-I and class-II superconducting materials are combined in chapters 3 and 4 respectively, the discussion of complex oxides is presented separately in chapter 5, and concluding remarks from the author are given in the last chapter.

1.1 Superconductivity and electron-phonon interactions

Soon after its discovery, it was realized that superconductivity involves a formation of a new physical state in which conduction electrons behave collectively and coherently. The microscopic nature of the driving force behind the formation of this new state was unclear until the pioneering works of Bardeen and Pines in 1955 [5] and Bardeen, Cooper and Schrieffer in 1957 [6]. More than half-a-century later, at the time of this writing, the only well-established cause of superconductivity remains the same. It's origin is related to the interactions between electrons in conduction bands and the vibrations of atoms of the crystal lattice: electron-phonon interaction.

1.1.1 Bardeen-Cooper-Schrieffer theory (BCS)

The two main concepts of the Bardeen-Cooper-Schrieffer theory are: the so called "Cooper pair" - two electrons with opposite spins bound together, and the "energy gap" - a gap that forms in the electronic structure of the material when it becomes superconducting. A third important concept is the nature of the interaction responsible for pairing. A conduction band electron in a metal normally behaves as a free particle. The electron is repelled from other electrons due to their negative charge, but it also attracts the positive ions that make up the rigid lattice of the metal. This attraction distorts the ion lattice, moving the ions slightly toward the electron. This increases the positive charge density of the lattice in the vicinity, and this positive charge can attract other electrons. At long distances the attraction between electrons due to the displaced ions can overcome the electrons' repulsion arising from their negative charge, and cause them to pair. The effect is due to electron-phonon interactions (see Fig. 1.2 for illustration).

Without going into much detail, let us state below the main equations of the BCS theory. The first one is the equation for a superconducting gap at T=0:

$$\Delta_{\mathbf{k}} = -\frac{1}{2}\sum_{\mathbf{k}'} \frac{V_{\mathbf{k},\mathbf{k}'}\Delta_{\mathbf{k}'}}{E_{\mathbf{k}'}}. \tag{1.1}$$

Here $\Delta_{\mathbf{k}}$ is the energy gap in momentum-space, $E_{\mathbf{k}'}$ is the quasiparticle energy and $V_{\mathbf{k},\mathbf{k}'}$ is the pairing interaction between electrons at vectors $\mathbf{k}$ and $\mathbf{k}'$.

A useful relationship can be obtained by solving (1.1)) at finite temperatures for an isotropic Fermi surface average of the pairing interaction V and the density of

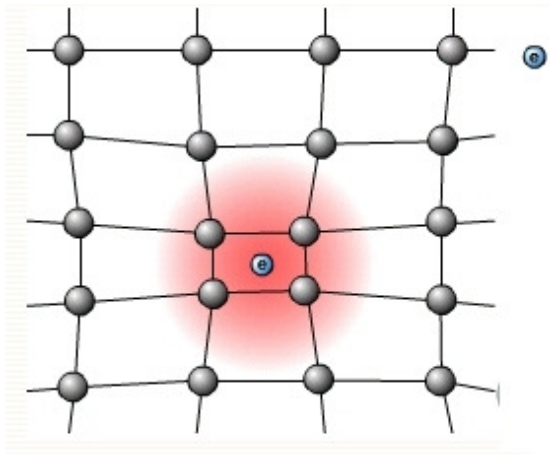

Figure 1.2: A cartoon explanation of the electron-phonon interaction based nature of the formation of Cooper pair.

states at the Fermi level $N(0)$

$$T_c = 1.13\omega_D exp\{-1/N(0)V\}, \tag{1.2}$$

where ω_D is used for the characteristic frequency of atomic vibrations, or the Debye frequency. This is the BCS model solution.

The great power and the beauty of the BCS theory is partly in its ability to quantitatively describe properties of the superconductors discovered before 1957 using effectively two parameters only: the Debye frequency and the electron-phonon coupling $\lambda = N(0)V$.

1.1.2 Beyond the BCS model

Refinements in the BCS theory were made by Gorkov and Eliashberg in 1957-1960 [7, 8]. A full description of the results of their theory is beyond the scope of this dissertation, we list some of the main concepts and implications. The reader can consult the original papers or review articles for more information (e.g. [9]).

First, a central quantity in Eliashberg's formalism is the spectral function $\alpha^2 F$. It has all the information about how individual scattering events for electronic states scattering from $\mathbf{k}$ to $\mathbf{k}'$ with an energy transfer of ω are coupled to the crystal vibrations.

Second, equation (1.2) can be transformed into the following form (McMillan's equation [10]):

$$T_\mathrm{c} = \frac{\omega_\mathrm{log}}{1.20} \exp\left[-\frac{1.04(1+\lambda)}{\lambda - \mu^*(1+0.62\lambda)}\right]. \tag{1.3}$$

Here $\omega_{\log}$ is the logarithmic frequency moment of the Eliashberg spectral function $\alpha^2 F$ and μ^* is a dimensionless parameter characterizing the screened Coulomb interaction strength.

Eliashberg theory has proven very successful in describing superconducting properties of various compounds that the original BCS theory was unable to describe because of its weak-coupling nature. We note that: even though originally Eliashberg theory was constructed to describe electron-phonon interactions for pairing, it has been applied for other types of pairing interactions. In eq. (1.3) above, for example, lambda can be considered to refer to other mechanisms of Cooper pairing.

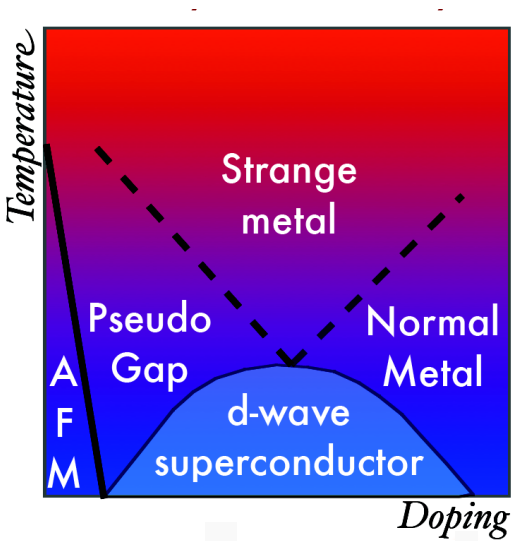

Figure 1.3: Superconducting phase diagram of copper oxides. AFM is the anti-ferromagnetic phase.

1.2 Non-conventional superconductivity

In 1986 Bednorz and Muller discovered a set of copper-based compounds that attracted much attention because of their high superconducting transition temperature [11]. It was soon found that the copper oxides differ significantly from the superconductors explained by the BCS theory. In particular, there are two main differences that can be pointed out: the gap in electronic dispersion is formed well before the system become superconducting (the "pseudogap") and a characteristic feature of the BCS model called "isotope effect" was absent for some cases. A schematic representation of the phase diagram for copper oxides is given in Fig. 1.3.

The isotope effect in the BCS theory characterizes the dependence of superconducting transition temperature T_c on the ionic mass of the superconducting isotope, and this originally served as a key argument supporting the electron-phonon picture. Since for copper oxides the isotope effect was not always observed, many researchers suggested that a pairing interaction of some other nature is present.

1.2.1 Spin-fluctuations induced pairing

Studies of the interplay of magnetic spin fluctuations and superconductivity began as a way to understand the suppression of T_c in some of the traditional

metals. Spin fluctuations which had provided a mechanism for pairing in ^{3}He, were later suggested as a pairing mechanism for some organic superconductors, heavy-fermion systems, and possibly copper oxides [12]. The paramagnon exchange interaction $V_S(q)$ for ^{3}He is repulsive, yet averaging this interaction over the Fermi surface with a p-wave form factor for the gap gives a positive (attractive) effective pairing interaction strength because $V_S(q)$ is peaked at small momentum transfers. In 1986 it was suggested that short range spin fluctuations can initiate pairing for copper oxides and the topology of the Fermi surface plays an important role [13]. For an up to date overview of the subject, the reader may consult Ref. [14].

1.2.2 Superconductivity in Fe-based compounds

An important discovery of a new system of superconducting materials was made in 2008 when iron-base superconductors emerged as a high-T_c class of materials [15]. The phase diagram for Fe-based compounds and their physical properties are similar to those of copper oxides, except for the fact that Fe-based compounds show no pseudogap (the current established picture) and the parent compounds for Fe-superconductors are metallic [16]. Examples of the crystal structures of these materials are given in Fig. 1.4

A theoretical description of the pairing mechanism for these systems was attempted shortly after discovery [17]. It was proposed that an isotropic pairing interaction symmetry with changing signs between different parts of the Fermi surface ("s±-theory") was present [17]. In other words, it was proposed that eq. (1.1) could be solved for the interaction $V_{\mathbf{k},\mathbf{k}'}$ that is repulsive, possesses s-wave symmetry and changes signs for scattering involving states on different parts of the Fermi surface. Further discoveries of FeSe based compounds with different Fermi surface topologies posed new questions, which are still open at the time of this writing [18].

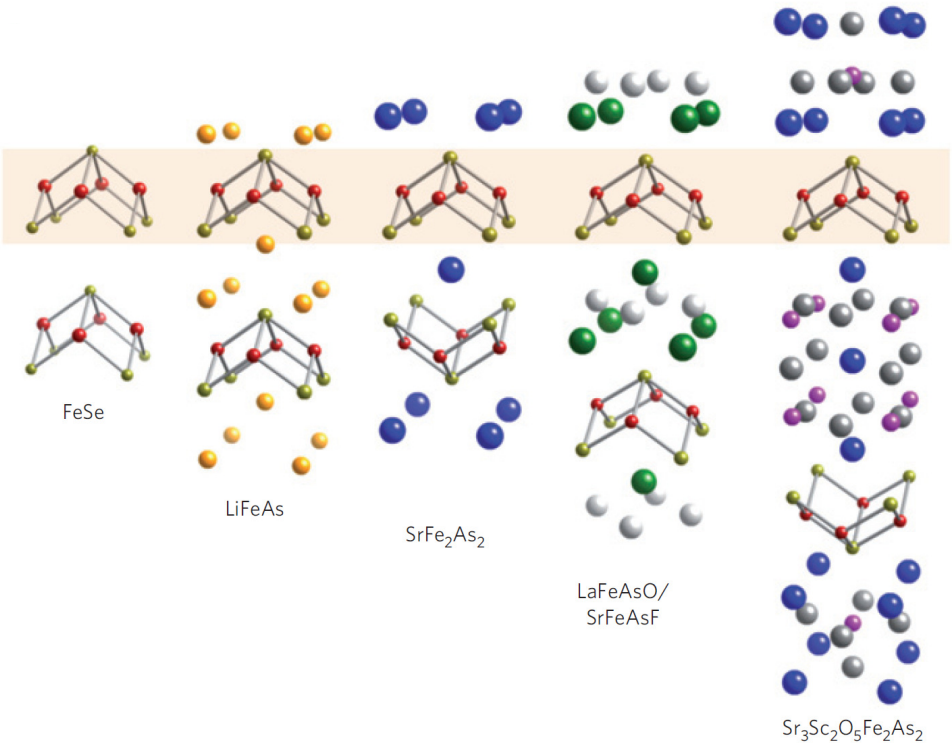

Figure 1.4: The crystal structures known to support superconductivity for the Fe-based compounds [16]. Fe atoms are colored red.

Chapter 2

Models and methods

This chapter has a brief description of the underlying theory for the first-principles techniques utilized in the current work. We start with an overview of the density functional theory with a focus on its application to superconductivity. We continue with a short description of the calculation of the electron-phonon interaction and how inclusion of magnetic properties affects it. We then proceed with a discussion of a particular technique called "Wannier interpolation" that is used to facilitate high precision results. And finally we present a calculational approach for the quasiparticle properties of materials by discussing possible ways to calculate spin susceptibility.

2.1 Density functional theory in application to superconductivity

Density functional theory (DFT) was established in 1964-65 by Hohenberg and Kohn, and Kohn and Sham [4, 19]. It allowed studies of many materials based solely on the fundamental first-principle input parameters: atomic numbers and crystal structures. The theory reduced the problem of studying a system of N electrons interacting with each other to the case of a system of N non-interacting electrons in an external potential. This was done by introducing the electronic density $n(\mathbf{r})$ as the main variable instead of the full electronic wavefunction:

$$\Psi\{\mathbf{r}_1, ...\mathbf{r}_N\} \rightarrow n(\mathbf{r}) = \sum_i |\varphi_i(\mathbf{r})|^2 \quad , \tag{2.1}$$

so that the Schrodinger's equation for the system takes the following form (Kohn-Sham equation):

$$\left[-\frac{\hbar^2}{2m}\nabla^2 + V(\mathbf{r}) + \int \frac{e^2 n(\mathbf{r}')}{|\mathbf{r}-\mathbf{r}'|} d^3r' + \mu_{\mathrm{XC}}[n(\mathbf{r})]\right] \varphi_i(\mathbf{r}) = \varepsilon_i \varphi_i(\mathbf{r}). \tag{2.2}$$

The external potential is called the exchange and correlation potential and is denoted above as $\mu_{\mathrm{XC}}[n(\mathbf{r})]$. The nature of this external potential defines the physical properties of the system and thus is extremely important. Ground state electronic energies ϵ_i and wavefunctions $\varphi_i = |i, \mathbf{k}\rangle$ can be obtained as the result of the DFT calculation.

In many cases very good agreement with experiment is achieved when the exchange and correlation potential is treated using the rather simple local density approximation (LDA) [20, 21]. A large variety of important scientific results have been and are still being obtained using LDA and the generalized gradient approximations (GGA). Below we explain how to apply DFT to study vibrational properties of crystals.

2.1.1 Density Functional Perturbation Theory formalism

Density functional perturbation theory (DFPT) is a perturbative approach to obtaining physical properties of materials from first principles [22]. The basic ansatz behind DFPT is that quantities such as the wavefunction, electron density, or potential may be written as a perturbation series

$$X(\lambda) = X^{(0)} + \lambda X^{(1)} + \lambda^2 X^{(2)} + \dots \tag{2.3}$$

where $X(\lambda)$ is a generic physical quantity that could, for example, be the Kohn-Sham orbital $\varphi(\lambda)$, the total energy $E(\lambda)$, or the electronic density $n(\lambda)$, and λ is a perturbing parameter, assumed to be small. The expansion coefficients are given by

$$X^{(n)} = \frac{1}{n!}\frac{d^n X}{d\lambda^n}\bigg|_{\lambda=0}. \tag{2.4}$$

It is convenient to express the energy of the crystal as

$$E_{tot}(\Delta\tau) = E_{tot}^{(0)} + \sum_{a\kappa\alpha}\sum_{b\kappa'\beta}\frac{1}{2}\left(\frac{\partial^2 E_{tot}}{\partial\tau^a_{\kappa\alpha}\partial\tau^b_{\kappa'\beta}}\right)\Delta\tau^a_{\kappa\alpha}\Delta\tau^b_{\kappa'\beta} + \dots \tag{2.5}$$

where the $E_{tot}^{(1)}$ term has been ignored, as this term yields the force acting on the atom, which is equal to zero at the minimum. Here $\Delta^a_{\kappa\alpha}$ is the displacement of atom κ from its equilibrium position τ_κ in the cell labeled a (with lattice vector $\mathbf{R}_a$) in the Cartesian direction α. In the harmonic approximation, this expansion is truncated after the second term. The force on a given atom is then

$$F^{ab}_{\kappa\alpha} = -\sum_{\kappa',\beta} C_{\kappa'\beta}(a,b)\Delta\tau^b_{\kappa'\beta} \tag{2.6}$$

where the matrix of force constants is defined through

$$C_{\kappa\alpha,\kappa'\beta}(a,b) = \left(\frac{\partial^2 E_{tot}}{\partial\tau^a_{\kappa\alpha}\partial\tau^b_{\kappa'\beta}}\right). \tag{2.7}$$

The Fourier transform of this is then

$$\tilde{C}_{\kappa\alpha,\kappa'\beta}(\mathbf{q}) = \frac{1}{N}\sum_{ab} C_{\kappa\alpha,\kappa'\beta}(a,b)e^{-i\mathbf{q}\cdot(\mathbf{R}_a-\mathbf{R}_b)} \tag{2.8}$$

where N is the number of periodic cells in the crystal, and $\mathbf{q}$ is the wavevector of the phonon perturbation. This is connected to the dynamical matrix $\tilde{D}_{\kappa\alpha,\kappa'\beta}(\mathbf{q})$ through

$$\tilde{D}_{\kappa\alpha,\kappa'\beta}(\mathbf{q}) = \tilde{C}_{\kappa\alpha,\kappa'\beta}(\mathbf{q})/(M_\kappa M_{\kappa'})^{1/2}. \tag{2.9}$$

This is a Hermitian matrix, as one would expect from Newton's second law, and its eigenvalues yield the phonon frequencies

$$\sum_{\kappa',\beta} \tilde{D}_{\kappa\alpha,\kappa'\beta}(\mathbf{q}) e_{m\mathbf{q}}(\kappa',\beta) = \omega^2_{m\mathbf{q}} e_{m\mathbf{q}}(\kappa\alpha) \tag{2.10}$$

where $\omega_{m\mathbf{q}}$ is the phonon frequency associated with mode m, and $e_{m\mathbf{q}}(\kappa\alpha)$ is the phonon eigenvector for the same mode. It is easy to see that the connection between the dynamical matrix and the second order energy term is then

$$\tilde{C}_{\kappa\alpha,\kappa'\beta}(\mathbf{q}) = 2E^{\tau^\star_{\kappa\alpha}\tau_{\kappa'\beta}}_{tot,-\mathbf{qq}} \tag{2.11}$$

where we have adopted the notation

$$E^{\tau^\star_{\kappa\alpha}\tau_{\kappa'\beta}}_{tot,-\mathbf{qq}} = \frac{1}{2}\frac{\partial^2 E_{tot,-\mathbf{qq}}}{\partial\tau^\star_{\kappa\alpha}\partial\tau_{\kappa'\beta}}. \tag{2.12}$$

The subscript $\mathbf{q}$ labels the phonon wavevector at which the second order energy has been calculated.

Thus, having the energies of the electronic system from DFT calculation and applying DFPT formalism described here, one can obtain phonon frequencies of a crystal.

2.1.2 Electron-phonon interaction

When the electronic energies, the wavefunctions and the phonon dynamical matrices of a crystal are obtained, one can proceed to calculate the parameters of the electron-phonon interaction. For a complete overview of theoretical background on this subject we refer the reader to Ref. [9] and Ref. [23]. Here we will cover the basics relevant for the first principle calculations.

An electron on the Fermi level interacts with the vibrations of the atoms of the crystal lattice. This process can be understood through an electron-phonon scattering exchange. An example diagram is given in Fig. 2.1. The phonon self-energy is responsible for many quantifiable physical effects in crystals. For example, it's contribution to the effective mass of an electron can be measured in heat capacity experiments [24]. A key component of the self-energy diagram is the matrix element for electron-phonon scattering:

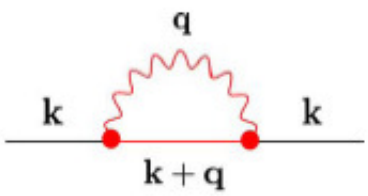

Figure 2.1: Diagrammatic representation of the electron self-energy arising from phonon exchange.

$$M^{[\nu]}_{\mathbf{k},\mathbf{k}+\mathbf{q}} = (\frac{\hbar}{m\omega_{\mathbf{q},\nu}})^{1/2}\langle\mathbf{k}|\delta_\nu V|\mathbf{k}+\mathbf{q}\rangle. \tag{2.13}$$

Here $\omega_{\mathbf{q},\nu}$ is the phonon frequency, $\delta_\nu V$ is the phonon perturbation for a particular mode ν and $\langle\mathbf{k}|$ is the Kohn-Sham (eq. 2.2) electronic eigenstate (phonon-related quantities are color-coded).

Obtaining the matrix elements allows us to calculate the wavevector-specific coupling parameter $\lambda_{\mathbf{q},\nu}$ within the isotropic Migdal approximation [9, 23, 25]:

$$\lambda_{\mathbf{q},\nu} = \frac{2}{N(0)\omega_{\mathbf{q},\nu}}\frac{1}{N}\sum_{\mathbf{k}}|M^{[\nu]}_{\mathbf{k},\mathbf{k}+\mathbf{q}}|^2\delta(\epsilon_{\mathbf{k}})\delta(\epsilon_{\mathbf{k}+\mathbf{q}}), \tag{2.14}$$

where $N(0)$ is the density of states at the Fermi level, and $\delta(\epsilon_{\mathbf{k}})$ is the energy conserving delta-function.

We can further divide eq. (2.14)) into three main components. The first one being the Fermi surface nesting function $\xi_{\vec{q}}$,

$$\xi_{\mathbf{q}} = \frac{1}{N}\sum_{\mathbf{k}}\delta(\epsilon_{\mathbf{k}})\delta(\epsilon_{\mathbf{k}+\mathbf{q}}). \tag{2.15}$$

The nesting function is a geometrical property of the Fermi surface and is particularly large for wavevectors which connect parallel portions of the surface. The second contribution arises from the phonon eigenfrequency $\omega_{\mathbf{Q},\nu}$. The final component, which contributes to the electron-phonon coupling strength, is the matrix element $M^{[\nu]}_{\mathbf{k},\mathbf{k}+\mathbf{q}}$, which accounts for the details of the interaction between electronic eigenstates and lattice vibrations.

The Eliashberg spectral function can be obtained through a Brillouin zone integral of $\lambda_{\mathbf{q},\nu}$ as

$$\alpha^2F(\omega) = \frac{1}{2}\sum_{\mathbf{q}}\omega_{\mathbf{q},\nu}\lambda_{\mathbf{q},\nu}\delta(\omega-\omega_{\mathbf{q},\nu}). \tag{2.16}$$

The frequency moments of the spectral function are related to the characteristic phonon frequency ($\omega_l og$ in eq. 1.3) and are calculated as [26]

$$\omega_n = 2 \int \omega^{n-1} \alpha^2 F(\omega) d\omega, \tag{2.17}$$

and

$$\omega_{log} = exp \left[\frac{2}{\omega_0} \int \frac{d\omega}{\omega} \alpha^2 F(\omega) \ln \omega \right]. \tag{2.18}$$

The integrals are taken from 0 to infinity in the two last expressions. We then use the frequency moments and the average coupling

$$\lambda = 2 \int \omega^{-1} \alpha^2 F(\omega) d\omega = 1/N \sum_{\mathbf{q},\nu} \lambda_{\mathbf{q},\nu} \tag{2.19}$$

in the the McMillan equation (see eq. 1.3). [10, 26] to estimate the superconducting transition temperature T_c.

2.1.3 Magnetism

In this section we show the main differences between the spin-independent and spin-resolved calculations. Magnetic interactions are treated within the local spin density approximation (LSDA).

Fot the calculations without spin, the main parameters of the system are wavefunctions and electron density, i.e. $\psi_{\mathbf{k},n} = |\mathbf{k}, n\rangle$ and $n(\mathbf{r})$. There is no total magnetization: $m(\mathbf{r}) = 0$. Phonon frequencies are not calculated including interaction between electronic spins: $\omega = \omega_{\mathbf{q},\nu}$. The matrix element for electron-phonon coupling is spin-independent:

$$M^{[\nu]}_{\mathbf{k},\mathbf{k}+\mathbf{q}} \rightarrow \langle \mathbf{k} | \delta_\nu V | \mathbf{k} + \mathbf{q} \rangle.$$

For the spin-polarized case the electronic wavefunctions and electron density are spin-dependent, hence

$$\psi_{\mathbf{k},n,\sigma} = |\mathbf{k}, n, \sigma\rangle,$$
$$n(\mathbf{r}) = n_\uparrow(\mathbf{r}) + n_\downarrow(\mathbf{r}).$$

The total magnetization is non-zero

$$m(\mathbf{r}) = n_\uparrow(\mathbf{r}) - n_\downarrow(\mathbf{r}),$$

and the phonon frequencies *are* calculated taking magnetic interaction between spins into account, i.e. $\omega = \omega'_{\mathbf{q},\nu}$. The matrix element for electron-phonon coupling is therefore spin-dependent:

$$M^{[\nu,\sigma]}_{\mathbf{k},\mathbf{k}+\mathbf{q}} \rightarrow \langle \mathbf{k}, \sigma | \delta_{\nu,\sigma} V | \mathbf{k} + \mathbf{q}, \sigma \rangle.$$

2.2 Wannier interpolation and precise calculations of electron-phonon parameters

The nature of the electron-phonon interaction λ is such that the sums in eq. 2.14 converge very slow with respect to the sampling over the electronic states inside the Brillouin zone. This fact makes a precise calculation of λ computationally very expensive. An interpolation technique is required to make the calculation efficient, robust and precise. Below we describe some of the basics underlying the Wannier interpolation scheme for electronic states and electron-phonon matrix elements.

2.2.1 Maximally localized Wannier functions

A Wannier function $\phi_{m,\mathbf{R}}(\mathbf{r})$ is defined as the Fourier transform of the Bloch function $\psi_{n,\mathbf{k}}(\mathbf{r})$ for electronic states generalized to include band mixing [27],

$$\phi_{m,\mathbf{R}}(\mathbf{r}) = \sum_{n,\mathbf{k}} U_{nm,\mathbf{k}} e^{-i\mathbf{k}\cdot\mathbf{R}} \psi_{n,\mathbf{k}}(\mathbf{r}). \tag{2.20}$$

Whenever the mixing matrix $U_{nm,\mathbf{k}}$ is unitary, the Wannier states turn out to be orthonormal. The usefulness of the Wannier representation relies on the spatial localization of the electronic states. Equation 2.20 indicates that there is considerable freedom associated with the transformation from Bloch to Wannier functions, since one has to choose both the manifold of the initial Bloch states and the unitary rotation associated with such a manifold. When the system under consideration presents a composite set of bands isolated from other bands by finite energy gaps, the choice of the Bloch manifold is natural and all that is required is the choice of the unitary transform $U_{nm,\mathbf{k}}$. The most convenient choice for the purposes of the present work is the one leading to maximally localized Wannier functions [28]. In this case, the unitary transform is determined by requiring that the resulting Wannier functions minimize the Berry-phase spatial spread operator. Wannier functions determined according to this procedure exhibit exponential localization is space [28–30].

2.2.2 Interpolation of electron-phonon matrix elements

Wannier functions can be used to interpolate the values of matrix elements from (2.13). For this we first need to express the matrix element in the Wannier basis (omitting the prefactor multiplier in braces from (2.13)):

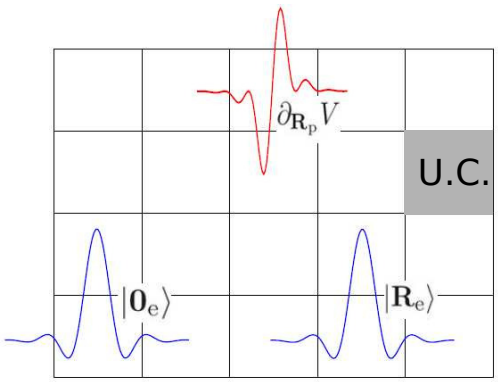

Figure 2.2: Cartoon illustrating how two electronic states centered on different atoms interact via a phonon in real space. Both electronic states and the phonon perturbation are localized in space within two unit cell (U.C.) distances. The square lattice indicates the unit cells of the crystal, the red lines shows the electron Wannier functions and the blue line shows the phonon perturbation in the Wannier representation. Whenever two of these functions are centered on distant unit cells, the e-ph matrix element in the Wannier representation vanishes.

$$M^{[\nu]}_{\mathbf{0},\mathbf{R}} = \langle \mathbf{0} | \delta_\nu V | \mathbf{R} \rangle. \tag{2.21}$$

Again, the phonon-related quantities are color-coded, and $\langle \mathbf{0}|$ and $\langle \mathbf{R}|$ are the electronic Wannier states centered at the corresponding points in the real space, $\delta_\nu V$ is the phonon perturbation (centered elsewhere in real space). The striking feature of the matrix element in Wannier representation (2.21) is the localization in both the electron and phonon variables. As illustrated in Fig. 2.2, the matrix element in the Wannier representation vanishes whenever points $\mathbf{0}, \mathbf{R}$ or the spatial location of the phonon perturbation corresponds to a unit cell sufficiently distant from the origin of the reference frame. As a consequence, to accurately describe the e-ph interaction in a given system, we only need to know a small number of matrix elements in the Wannier representation. This elementary observation constitutes the core of this section.

Performing the following set of transforms illustrates the interpolation scheme. First, a Fourier transform is performed from original Bloch to Wannier space involving coarse **k**-vector sampling grid. Second, truncating the calculation supercell containing the matrix element localized in space at the distance when the value of the matrix element in Wannier representation (2.21) is small, the matrix elements are obtained everywhere in the Wannier space. Finally, the Fourier transform back to reciprocal (Bloch) space to an arbitrary size final **k**-sampling

grid is done. After the interpolation, the summation in 2.3 is performed to obtain the electron-phonon coupling.

2.3 Electron-electron interaction mediated by spin fluctuations

Quasiparticles are emergent physical phenomena that occur when a microscopically complicated system, such as a solid, behaves as if it contained different weakly interacting particles in free space. We have already discussed phonons which represent collective excitations of the solid. Now let us briefly discuss the physical nature of applying the quasiparticle formalism to studying spin-fluctuations induced electron-electron interactions in crystals. As was mentioned in the "Introduction" part of this dissertation, spin-fluctuations may be responsible for the superconducting pairing in class-II (or non-conventional) superconducting materials. Is this section we discuss the electronic states that interact through exchange of spin fluctuations, and refer to these electronic states as quasiparticles.

2.3.1 Magnetic response of a solid

Consider a system of N electrons in a solid with an external magnetic perturbation originating from an external magnetization density $\delta\mathbf{m}_{ext}(\mathbf{r})$. System's response to this magnetization can be computed in a similar manner to how it is done for the screened Coulomb interaction in the GW approximation [31, 32]. The magnetization $\delta\mathbf{m}_{ext}(\mathbf{r})$ causes an external magnetic field $\delta\mathbf{B}_{ext}$ and an induced magnetic field $\delta\mathbf{B}_{ind}$ to be present. The direct "external" field is given by

$$\delta B_{\alpha}^{ext}(\mathbf{r}) = \sum_{\beta} \int d^3\mathbf{r}' I_{\alpha\beta}(\mathbf{r},\mathbf{r}')\delta m_{\beta}^{ext}(\mathbf{r}'). \tag{2.22}$$

The induced magnetic field is similarly given by $\delta B_{ind} = I\delta m^{ind}$ with

$$\delta m_{\alpha}^{ind}(\mathbf{r}) = \sum_{\beta} \int d^3\mathbf{r}' \chi_{\alpha\beta}^{S}(\mathbf{r},\mathbf{r}')\delta B_{\beta}^{ext}(\mathbf{r}'), \tag{2.23}$$

where χ^S is the interacting spin susceptibility.

For a paramagnetic ground state the interaction is given by

$$I_{\alpha\beta}(\mathbf{r},\mathbf{r}') = \frac{\delta B_{xc}^{\alpha}(\mathbf{r})}{\delta m^{\beta}(\mathbf{r}')} = \delta(\mathbf{r}-\mathbf{r}')\delta_{\alpha\beta}\tilde{I}(\mathbf{r}) \tag{2.24}$$

$$\tilde{I}(\mathbf{r}) = \frac{\partial_{|m|}[n\epsilon_{xc}](\mathbf{r})}{|m(\mathbf{r})|} = \frac{2\alpha_c(n(\mathbf{r})) + \frac{4}{9}\epsilon_x(n(\mathbf{r}))}{n(\mathbf{r})}. \tag{2.25}$$

We evaluate the derivatives of the exchange-correlation energy using the LSDA functional (as given in Ref. [33]). The total magnetic field is given by

$$\delta B_{tot} = (I + I\chi^S I)\delta m_{ext}. \tag{2.26}$$

The quantity in parenthesis can be interpreted as a screened magnetic interaction in analogy with the screened charge interaction used in the GW approximation [31, 34]. The interacting spin susceptibility obeys a Dyson-type equation (in a short-hand matrix notation)

$$\chi^S = \chi_0 + \chi_0 I \chi^S, \tag{2.27}$$

with χ_0 being the non-interacting Kohn-Sham response function given by (in a paramagnetic system)

$$\chi^0_{\alpha\beta} = \delta_{\alpha\beta} 2 \sum_{nm} \frac{\varphi_n(\mathbf{r})\varphi_m(\mathbf{r})\varphi_n(\mathbf{r}')\varphi_m(\mathbf{r}')}{\epsilon_m - \epsilon_n}. \tag{2.28}$$

The factor of two above comes from having two spins.

2.3.2 Numerical implementation

Using a plane wave basis, i.e. we can calculate the non-interacting susceptibility (2.28)) $\chi^0_{\mathbf{GG}'}(\mathbf{q},\omega)$ in reciprocal space. Here $\mathbf{G}, \mathbf{G}'$ are the planewave vectors, $\mathbf{q}$ - reciprocal lattice vector of electron scattering from $\mathbf{k}$ to $\mathbf{k}'$, ω - frequency at which it happens. To obtain the interaction we first calculate the dielectric function (assuming a paramagnetic ground state)

$$\epsilon(\mathbf{r},\mathbf{r}',\omega) = \delta(\mathbf{r}-\mathbf{r}') - \int d\mathbf{r}'' I(\mathbf{r},\mathbf{r}'')\chi^0(\mathbf{r}'',\mathbf{r}',\omega) \tag{2.29}$$

$$= \delta(\mathbf{r}-\mathbf{r}') - \tilde{I}(\mathbf{r})\chi^0(\mathbf{r},\mathbf{r}',\omega), \tag{2.30}$$

where we used (2.24). This expression contains a multiplication in real space that leads to a convolution in Fourier space

$$\epsilon_{\mathbf{GG}'}(\mathbf{q},\omega) = \delta_{\mathbf{GG}'} - \sum_{\mathbf{G}''} I_{\mathbf{G}-\mathbf{G}''}\chi^0_{\mathbf{G}''\mathbf{G}'}(\mathbf{q},\omega). \tag{2.31}$$

Next, the induced magnetic interaction between two electrons is given by (following a convention from Ref. [12, 35])

$$V = \epsilon^{-1} I, \tag{2.32}$$

or with indices

$$V_{\mathbf{GG}'}(\mathbf{q},\omega) = \sum_{\mathbf{G}''} \epsilon^{-1}_{\mathbf{G},\mathbf{G}''}(\mathbf{q},\omega) I_{\mathbf{G}''-\mathbf{G}'}. \tag{2.33}$$

2.3.3 Interaction strength

The final step is to estimate the interaction strength. We follow the formalism explained in Ref. [36]. Since we are working with a paramagnetic ground state, we will omit spin indices further. The Fermi surface average of a spin-fluctuations induced scattering matrix elements can be written as

$$\mu_{spin} = \frac{1}{N(0)} \sum_{n,\mathbf{k}} \sum_{n',\mathbf{k}+\mathbf{q}} V_{n\mathbf{k},n'\mathbf{k}+\mathbf{q}} \delta(\epsilon_{\mathbf{k}} - \epsilon_F)\delta(\epsilon_{\mathbf{k}+\mathbf{q}} - \epsilon_F), \tag{2.34}$$

where $N(0)$ is the density of states at the Fermi level ϵ_F, and $\delta(\epsilon_{\mathbf{k}} - \epsilon_F)$ is the energy conserving Dirac delta-function. The matrix element for scattering of a Cooper pair can be expressed as:

$$V_{n\mathbf{k},n'\mathbf{k}+\mathbf{q}} = \langle n\mathbf{k}, n{-}\mathbf{k}|\ V(\mathbf{q})\ |n'\mathbf{k}+\mathbf{q}, n'{-}\mathbf{k}\rangle, \tag{2.35}$$

with wavevectors $\mathbf{k}$ and $\mathbf{k}' = \mathbf{k} + \mathbf{q}$, n and n' denoting the band indices, and $V(\mathbf{q}) = 3\ V_{\mathbf{GG}'}(\mathbf{q}, \omega = 0)$ as defined in (2.33). The factor of 3 comes from summing over spatial axes. After Fourier transformation this interaction has the following form in momentum space:

$$V_{n\mathbf{k},n'\mathbf{k}'} = \sum_{\mathbf{G},\mathbf{G}'} f^*_{n\mathbf{k},n'\mathbf{k}'}(\mathbf{G}) V_{GG'}(\mathbf{q}) f_{n\mathbf{k},n'\mathbf{k}'}(\mathbf{G}'). \tag{2.36}$$

We omitted the frequency dependence in $V_{GG'}(\mathbf{q}, \omega)$ from (2.33) because we treat the interaction within a static approximation in this work. Finally $f_{n\mathbf{k},n'\mathbf{k}'}(\mathbf{G})$ in (2.36) can be expressed as

$$f_{n\mathbf{k},n'\mathbf{k}'}(\mathbf{G}) = \sum_{\mathbf{G}'} \varphi_{n'\mathbf{k}'}(\mathbf{G} + \mathbf{G}')\varphi^*_{n\mathbf{k}}(\mathbf{G}'). \tag{2.37}$$

2.4 Summary of the computational details

Here we summarize the computational setup for all the chapters that follow. The details presented are describing the implementations of the pseudopotential density functional approach [37] for each case studied.

2.4.1 Lithium

We use the local spin density approximation (LSDA) to the density functional theory (DFT) [38, 39] within the planewave pseudopotential scheme [40–42] as implemented in `Quantum-ESPRESSO` [43]. The norm-conserving Li pseudopotential included 2s and 2p states in the valence and a non-linear core correction. The pseudopotential was generated according to the Troullier-Martins scheme [41]. A 30 Ry kinetic energy cutoff was enough to attain convergence for total energy calculations. We did not include the 1s valence state as it introduced the need for a much higher kinetic energy cutoff without significantly increasing the precision of the calculations [44]. The pseudopotential cutoff radius of 2.5 a.u. was small enough to avoid core overlap up to the pressures studied in this work.

Lattice dynamical properties were obtained through density-functional perturbation theory (DFPT) [45] and the electron-phonon coupling matrix elements and total coupling parameter were calculated using a first-principles interpolation scheme [27] based on maximally-localized Wannier functions [27–29, 46]. An 8×8×8 initial sampling of the Brillouin zone was suitable to achieve an acceptable real-space decay necessary for convergence of both the interpolated electronic structure and lattice dynamics. The final sampling of the BZ was performed on a momentum space grid containing as many as 8 million wavevectors.

2.4.2 FeSe, K-intercalated FeSe

The electronic properties are calculated using the generalized gradient approximation (GGA) to density functional theory (DFT) [20, 38] within a planewave pseudopotential scheme [40, 41]. Phonon dispersions are calculated through density-functional perturbation theory (DFPT) [45]. The electron-phonon coupling matrix elements, total coupling parameter, and transition temperatures are obtained using the standard McMillan-Eliashberg based approach.

Ultrasoft pseudopotentials are employed. A cutoff of 80 Ry is used for the wave function expansion, and 560 Ry cutoff - for charge densities. Brillouin zone sampling is performed on a 64×64×16 momentum k-space grid for electronic integration and 8×8×8 q-space for dynamical matrices calculation.

2.4.3 FeSe-monolayer

We use a 40 Ry cutoff value for the kinetic energy of the planewave basis and 600 Ry cutoff - for the electronic density. Crystal structures are relaxed, so that the forces on the atoms are less then 0.5 mRy/$\AA$. For the non-magnetic and the checkerboard spin-polarized configuration we use a 4-atom tetragonal unit cell. In the stripe spin-polarized case, we choose a unit cell with 8 atoms, and the relaxed structure possesses orthorhombic symmetry as the striped spin arrangement introduces a lattice distortion. The non-magnetic, checkerboard and stripe phases respectively show: 6.97, 7.10, 7.11 in atomic units (a.u) for the equilibrium lattice constants; 2.57, 2.70 and 2.72 in a.u. for the Se-atom heights; and 0, 2.28 and 2.62 bohr magnetons for the equilibrium magnetic moments. The total energies of checkerboard and stripe phases are 13 and 20 mRy, respectively, lower then the non-magnetic state, when related to the 4-atom cell. The background charge is introduced using a uniform like-jellium approximation. No relaxation is done for the charged configurations. The magnetization constraints are introduced within LSDA through the energy penalty functional, as it is implemented in `Quantum-ESPRESSO` package [43], so that a certain value of magnetization on the individual atoms is preferred.

2.4.4 LiBC

We use norm-conserving pseudopotentials with a planewave basis up to 60 Ry. For the Li pseudopotential, we find inclusion of the 1s state to be unnecessary. The grids of 16×16×8 and 8×8×8 k-points are used for self consistent field calculations of Li_2B_3C and $Li_4B_5C_3$, respectively, to achieve similar k-point densities for both systems. For the densities of states calculations, three times denser grids of 48×48×24 and 24×24×24 k-points respectively are sampled. A gaussian smearing of 0.03 Ry is used.

Density-functional perturbation theory [45] is employed to compute phonon frequencies and electron-phonon coupling parameters on a coarse mesh (4×4×4 for Li_2B_3C, 2×2×2 for $Li_4B_5C_3$) of reciprocal vectors $\vec{Q}$ (ν is the phonon branch index). Interpolation techniques [27] based on maximally-localized Wannier functions [27–29] are then used to interpolate electron-phonon coupling parameters on a fine grid (up to 24×24×24). For this interpolation, we use Wannier90 and EPW packages [30, 46], and the XCrysDen code is used to visualize the structures [47].

2.4.5 $Ba_{0.5}K_{0.5}BiO$

Scalar-relativistic norm-conserving pseudopotentials with a planewave basis up to 80 Ry are employed. For the valence states in the pseudopotential for Bi we use 5d, 6s and 6p states; for Ba - 5s, 5p, 6s; for O - 2s, 2p; for K - 3s, 3p, 4s. We find that inclusion of semi-core states is important to correctly reproduce structural distortions in $Ba_{1-x}K_xBiO_3$.

Density-functional perturbation theory [45] is used to compute phonon frequencies and electron-phonon coupling parameters on a coarse mesh (4×4×4 in the 20-atom cell case, 6×6×6 for the 5-atom cell) of reciprocal vectors $\vec{Q}$ (ν is the phonon branch index). Next, interpolation techniques [27] based on maximally-localized Wannier functions [27–29] are used to interpolate electron-phonon coupling parameters on a fine grid (up to 30×30×30). For this interpolation, the Wannier90 and EPW packages are employed [30, 46].

2.4.6 FeSe spin susceptibility

We used LDA ([20]) norm-conserving pseudopotentials with a planewave basis up to 120 Ry obtained from `Quantum-ESPRESSO` pseudopotential library (Fe.pz-hgh.UPF). For the Fe pseudopotential 3d,4s and 4p states are included in the valence shell. The grid of 32×32×4 k-points are used for self consistent field calculations and subsequent calculations as well. A gaussian smearing of 0.05 Ry is employed. Experimental values of lattice constants a and c are utilized [48]. No structure relaxation is done.

Chapter 3

Class-I superconductors

This chapter summarizes the results obtained for the conventional, or class-I superconductors. For these materials the main mechanism responsible for the superconducting pairing is electron-phonon interactions. We use precise first-principle techniques to calculate and analyze the electron-phonon coupling parameters and superconducting transition temperatures.

We present below the underlying motivation for the research conducted, results, discussion and a short summary of findings for every case studied. Full description of each case can also be found in [49–51].

3.1 BCC Li at ambient conditions

The electron-phonon coupling in bcc lithium was studied using a first-principles pseudopotential approach. Wannier interpolation based technique that allows for ultradense sampling of electron-phonon parameters throughout the Brillouin zone was employed. The coupling strength was calculated precisely resolving many of the fine features of its distribution over the zone. The contributions to coupling arising from the Fermi surface topology and electron-phonon matrix elements were separately analyzed. The value of the coupling found for pressures in the 0-5 GPa range is 0.36-0.43 correspondingly. The structure in the wavevector dependent coupling is suggested to be due to the Fermi surface topology. The Eliashberg spectral function $\alpha^2F(\omega)$ shows some increase of spectral weight in the low-frequency region with the application of pressure. We estimate the superconducting transition temperature and find that the obtained values are in accord with experiment for a big, but still reasonable value of Coulomb repulsion $\mu^* = 0.21$.

3.1.1 Motivation

Having only one valence electron, lithium and other alkalis are expected to be simple metals. At room temperature and atmospheric pressure lithium, in the bcc structure, has a Fermi surface that shows little deviations from a free-electron sphere, and many features related to its electronic properties can be very well described within the nearly-free-electron model. Nevertheless lithium still exhibits features that are challenging to explain. One of them is the strength of the electron-phonon coupling at ambient conditions. Many previous estimates predict the electron-phonon and the electron-electron interactions to be significant [37, 49, 52–60]. However superconductivity in zero-pressure samples is not easily-achievable despite the large coupling values predicted.

In addition, the phase diagram of lithium is rather complicated, and lithium is found in several structures. For bcc lithium the superconducting phase transition occurs at temperatures below the millikelvin range at atmospheric pressure [61]. The bcc structure is experimentally seen to be present for all temperatures, although there are evidence of a transition to the $9R$ phase occurs near 80 K [62–65]. With the application of pressure, bcc Li transforms to the fcc phase near 8 GPa and becomes a superconductor with a T_c of 14 K at 20 GPa. Continued increase in pressure causes Li to undergo several structural transitions, and to eventually exhibit a metal-to-insulator transition at 70 GPa [44, 66–71]. Understanding the electron-phonon interactions in Li may be a guide to explaining some of these features.

The experimental value of the electron-phonon coupling strength λ for the bcc structure obtained from heat capacity measurements is about 0.4 [55]. One of the first theoretical estimates for the electron-phonon coupling was calculated using the empirical pseudopotential method, giving values around 0.5±0.1 depending on which pseudopotential was used [37]. Another estimate based upon bandstructure calculations yielded 0.36 [56]. Use of the fully first-principle pseudopotential approach based methods then produced coupling values ranging from 0.38 to 0.45 [52–54]. The latter of these calculations utilized a frozen phonon approach for the treatment of lattice vibrations. A superconducting transition at significantly higher temperatures than experimentally observed has been predicted using the total electron-phonon coupling strengths for multiple structures of Li [57]. It has also been shown that the Fermi surface topology plays a crucial role in the onset of superconductivity in the fcc phase of Li [58, 59]. In these studies the results of the zone integral were shown to be sensitive to the Brillouin zone (BZ) sampling and the need for finer sampling to calculate coupling precisely was emphasized.

In the current work we study the electron-phonon coupling for the monatomic bcc phase of Li in the 0-5 GPa pressure range. Utilizing a method based on first-principles calculations and subsequent Wannier interpolation techniques, we can obtain a very fine sampling of the total coupling strength λ throughout the BZ. We analyze this strength in terms of the effective contributions from Fermi surface nesting, phonon frequencies and electron-phonon matrix elements. The Eliashberg spectral function $\alpha^2F(\omega)$ is analyzed and the superconducting transition temperature is estimated through the McMillan equation [26].

3.1.2 Results

We present the results at zero pressure in bcc Li as well as those at 2.5 and 5 GPa for reference. Relative compressions, the ratio of compressed to ambient volume, corresponding to these pressures are 0.86 and 0.78 respectively. Using the generated pseudopotential, a 2 GPa shift is necessary to reach good agreement with the room temperature experimental equation of state [66]. We give the unshifted LDA values for pressure.

We start by analyzing the shape of the Fermi surface nesting function $\xi_{\vec{Q}}$. It shows little variation with pressure. This is consistent with little change in the structure of the Fermi surface with the application of pressure to bcc Li. From Figure 3.1(a) it can be seen that there is some structure in $\xi_{\vec{Q}}$. The main structure is reflected in the step-like discontinuities arising from the near-spherical shape of the Fermi surface. It can be shown that for a spherical Fermi surface $\xi_{\vec{Q}} \propto \frac{1}{|\vec{Q}|}\theta(2k_F - Q)$. In the bcc structure, this general feature is also found.

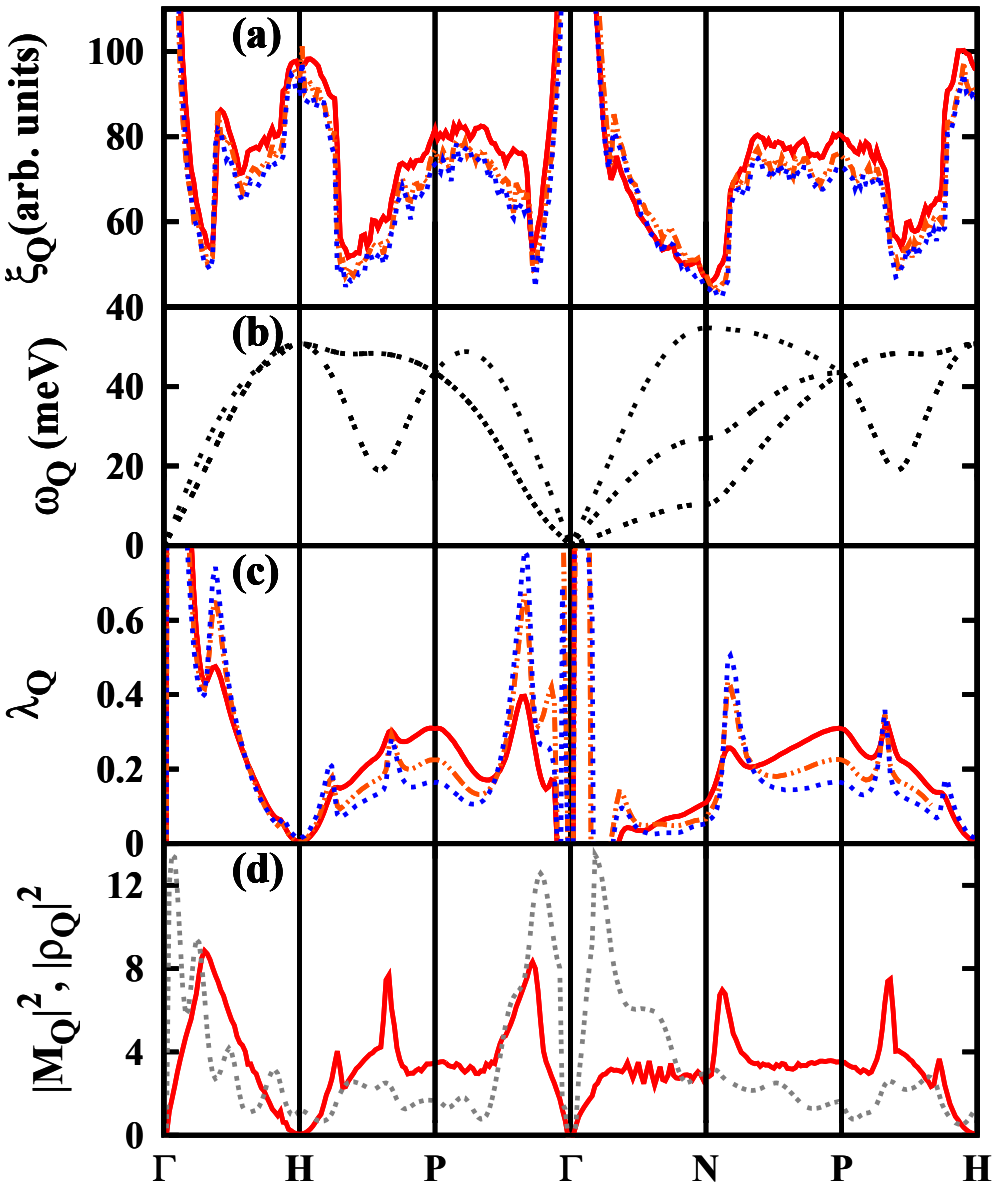

Figure 3.1: Physical properties of bcc Li along a path inside Brillouin Zone: (a) The Fermi surface nesting function ξ_Q, (b) an example of the phonon dispersions ω_Q for 3 modes at 5 GPa, (c) the total electron-phonon coupling λ_Q, (d) the Fermi surface average of the electron-phonon matrix element squared $|M_Q|^2$ (solid line) and the overlap integral of the electronic states $|\rho_Q|^2$ (dashed line) given for 5 GPa. In (c) the coupling value is a sum over all phonon modes. In (a) and (c) solid line corresponds to 0 GPa, dot-dashed - to 2.5 GPa, dashed - to 5 GPa.

The phonon dispersions for 5 GPa are plotted on Fig. 3.1(b). For other pressures they look similar. The "dip" in $\omega_{\vec{Q}}$ between H and P can be associated with the Kohn anomaly situated there. Unlike the fcc phase [49], most of the coupling strength in bcc Li comes from the longitudinal phonons for the cases studied. The wavevector dependent electron-phonon coupling summed over phonon modes is shown on Fig. 3.1(c). We can see a well-defined structure in the plot, where there are a few distinct peaks that show sharp increase with pressure at certain points. Some decrease for the remaining background is present, and this is possibly related to the decrease in nesting function values. The positions of the peaks coincide with the nesting function discontinuities on Fig. 3.1(a). The average squared matrix element for a particular $\vec{Q}$ is given in Fig. 3.1(d) together with the average value of the overlap between the electronic states separated by $\vec{Q}$. More discussion of this plot follows.

In Figure 3.2, the Eliashberg spectral function and phonon density of states are presented. For comparison $\alpha^2F(\omega)$ for the 8 GPa fcc phase is also given [49]. We see that the changes of both $\alpha^2F(\omega)$ and $F(\omega)$ with pressure are similar. Both the higher frequency LA peak and the lower frequency TA peak are shifted due to the phonon stiffening. In the plot of $F(\omega)$, the low frequency peak magnitude decreases slightly with pressure, while the peak magnitude increases in the spectral function. Thus the magnitude of the coupling, $\alpha^2 = \alpha^2F/F$ is amplified as the pressure is applied. Increased spectral weight in the low-frequency region is primarily responsible for the higher values of total coupling λ.

The frequency moments of the Eliashberg spectral function and the resulting estimated values of the superconducting transition temperature are given in Table 3.1. The superconducting transition temperature corresponding to the calculated electron-phonon coupling parameter is obtained using the modified McMillan equation [26]. Because of the ultra-fine sampling implemented, our results are well converged with respect to the BZ sum. The features that would otherwise be obscured by numerical broadening have been resolved. They have a significant effect on the average coupling and other frequency moments. Thus we may expect the T_c estimates to be precise as well within the chosen model.

The logarithmic averaged frequency increases slightly as a result of the phonon stiffening, and the square frequency decreases slightly with pressure, arising from the shift of spectral weight to lower frequencies. The total coupling strength λ increases from 0.36 at zero pressure to 0.43 at 5 GPa giving a considerable increase in T_c. In order to achieve consistency with the experimentally measured superconducting transition of 0.4 mK, the value of $\mu^* = 0.21$ is necessary. Fig. 3.3 displays the colormap of T_c for different values of μ^* and λ within the estimated accuracy limitations of our approach. We see, that the lowest possible predicted

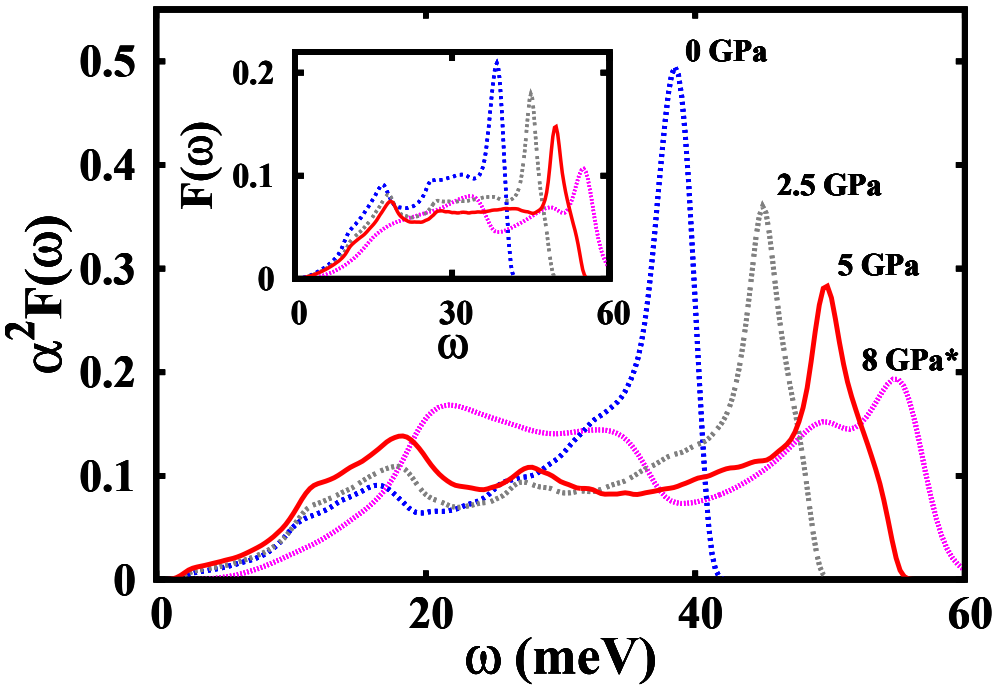

Figure 3.2: Eliashberg function $\alpha^2 F(\omega)$ for different values of pressure. Effective sampling of 50x50x50 k and q-points inside the BZ was utilized. (inset) Phonon densities of states $F(\omega)$ for the same pressures. (*) The 8 GPa $\alpha^2 F(\omega)$ function corresponds to the fcc structure and is given for comparison.

P(GPa)	ω_{log}	$\langle\omega^2\rangle^{1/2}$	λ	$T_c(\mu^* = 0.13)$	$T_c(\mu^* = 0.21)$
0	313	240	0.36	180	0.26
2.5	330	237	0.37	230	0.62
5	330	225	0.43	740	25
8*	308	378	0.39	500	10

Table 3.1: Pressure evolution of frequency moments of spectral function $\alpha^2F(\omega)$. We show the total coupling strength λ, as well as the logarithmic and square average frequencies (in K). The superconducting transition temperature (T_c, in mK) is estimated using the Allen-Dynes formula [26] with a Coulomb parameter μ^* given above. (*) The 8 GPa $\alpha^2F(\omega)$ values corresponds to fcc structure and are given for comparison.

magnitude of the Coulomb pseudopotential is about 0.18, which is similar to what was found for aluminum from first-principles calculations [72].

3.1.3 Discussion

The shape of the Fermi surface seems to have a profound effect on the electron-phonon properties of lithium. In the fcc phase, for example, Fermi surface topology forms the necessary conditions for superconductivity to appear [49, 58]. In the bcc structure we see that the nesting function does not have sharp peaks that denote regions with extremely strong coupling, but nesting does show other interesting features. The Fermi surface in the bcc structure is almost perfectly spherical. This is why the bcc Li nesting function closely resembles the theta-function-based form given in part III. We notice that this form predicts step-like discontinuities to appear when

$$|\vec{Q}| = |2\vec{k}_F \pm \vec{G}|, \tag{3.1}$$

or at the points where scattering onto $2k_F$ and $|2\vec{k}_F \pm \vec{G}|$ occurs. Here $\vec{G}$ is any of the reciprocal lattice vectors. This is indeed what can be seen from Fig. 3.1(a).

Kohn anomalies are also expected to be present wherever the condition (3.1) is satisfied. One Kohn anomaly is seen between H and P on Fig. 3.1(b). The other ones are not present, possibly because of screening. On the other hand the positions of the peaks in electron-phonon coupling of Fig. 3.1(c) coincide with the nesting function discontinuities. So we see that the coupling increases wherever the equality condition (3.1) is satisfied. To explain this increase, it is natural to look at the electron-phonon matrix elements behavior. Fig. 3.1(d) shows that

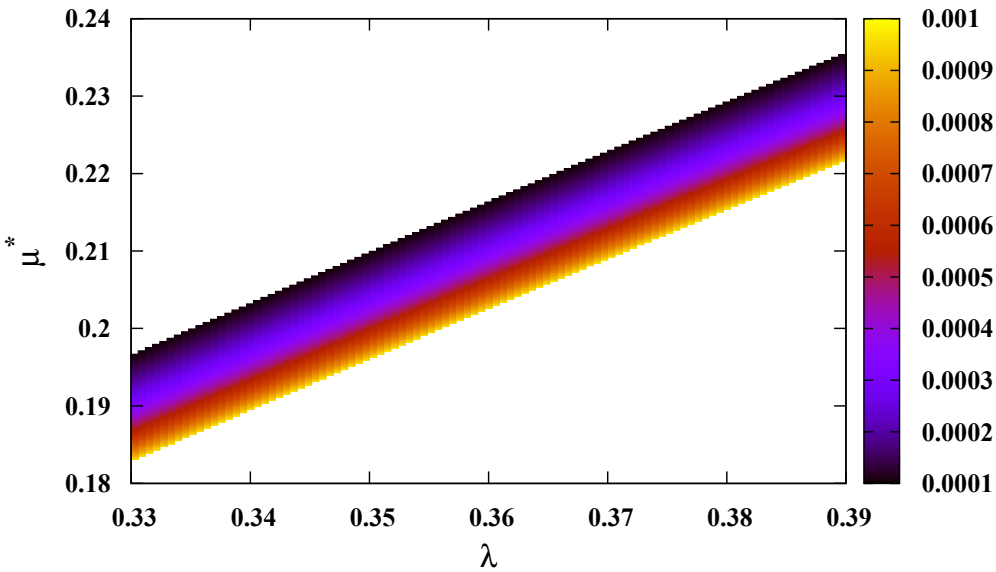

Figure 3.3: The color map of the superconducting transition temperature T_c estimated according to McMillan's equation for a range of electron-phonon coupling λ and Coulomb repulsion parameter μ^*. Only T_c values within 0.1÷1 millikelvin are shown (scale is given in K).

the increased coupling areas coincide with areas with increased matrix elements. Here we conclude that the structure in electron-phonon coupling is induced by the matrix elements distribution over the zone.

First we suggest that, since the shapes of the electronic states $|\vec{k}\rangle$ and $|\vec{k}+2\vec{k}_F\rangle$, for example, are similar, the amplification at the particular k-points could be due to the increased overlap integral between initial and final scattering states. This latter hypothesis can be justified by looking at the average overlap plot in Fig. 3.1(d). The overlap $|\rho_{\vec{Q}}|^2$ plot shows some increase where $\lambda_{\vec{Q}}$ peaks. However, this increase is small. After looking at the expression (2.13), we note that the parameter which can be responsible for the structure in electron-phonon matrix elements, and thus also for the structure in the coupling itself, is the phonon perturbation operator $\delta_\nu V$.

We conclude that there is a well pronounced effect of Kohn anomalies on the electron-phonon matrix elements, which is reflected in highly non-uniform distribution of the phonon perturbation operator over the BZ. This leads to an increase in the electron-phonon matrix elements at particular points in the BZ. This increase becomes more evident with pressure. Sharp structure in electron-phonon coupling explains the need for fine sampling and the previous difficulties associated with precise calculation of the total electron-phonon coupling in bcc Li.

The Electron-phonon interactions are increased when pressure is applied. It is seen from the Eliashberg spectral function evolution as mentioned in Part III. This increase may affect the phase diagram, and, in particular, play an important role in the bcc-to-fcc transition that experimentally occurs at about 8 GPa. Another effect of pressure could be to make the electron-electron interactions less important. The latter conclusion can be based on the fact that unlike the fcc phase, where $\mu^* = 0.13$ results in good agreement with experimental values, in the bcc phase $\mu^* = 0.21$ must be used to find T_c in the millikelvin range, where the experimental transition was observed. Small values of T_c bring another level of uncertainty, since minor changes in λ and μ^* have a large effect on the transition temperature.

Several points can be made to justify the large magnitude of Coulomb repulsion. First, $\mu^* = 0.21$ is not an unphysical value. Within the framework we utilize, this indicates that the electron-electron interactions are expected to be quite strong. We are not aware of any direct first-principle calculation of the Coulomb parameter for Li. Calculations for other metals which exist in the literature provide values which seem to be consistent with the commonly employed $\mu^* = 0.13$ [72, 73]. On the other hand, a value of Coulomb pseudopotential which is similar to what is inferred in this work has been suggested previously for lithium at ambient conditions [74]. A possibility for significantly larger than commonly used value is discussed in the above paper based on the renormalization of the effective electron-electron repulsion with the density of states at the Fermi level. Secondly, we suggest that with the application of pressure, lithium becomes less free-electron-like. Within the Fermi-Thomas model, for instance, the electron-electron interactions should become less strong with pressure. This may explain why the effective value of the Coulomb pseudopotential for fcc is in the commonly accepted range [49]. Finally, if we take into account the limits of the precision of our calculations (see Fig. 3.3), the possibility of μ^* being as low as 0.18 emerges, and this value already is within the previously predicted range for the repulsion [72].

According to available experimental knowledge, the low temperature phase of lithium at zero pressure seems to be a complicated mixture of several structures including bcc and 9R [64]. We can note on the basis of our study and previous calculations for the 9R phase [52] that the usual electron-phonon based model of superconductivity together with the increased electron-electron interactions derived from the free-electron-model should, in principle, explain the experimental observations. It is hoped that more explanation can be provided by experimental studies of the isotope effect on T_c or careful first-principle studies of the Coulomb pseudopotential μ^*.

3.1.4 Summary

We investigated the electron-phonon interactions in bcc lithium from first-principles by considering the pressure evolution of the wavevector dependent electron-phonon coupling parameter and its constituent elements. We found that the electron-phonon interaction is highly affected by the topological features of the Fermi surface. We explain the particular mechanism by which the electron-phonon matrix elements are enhanced at certain points of the BZ. Our calculated superconducting transition temperature for zero-pressure phase is in agreement with experiment for $\mu^* = 0.21$. It shows that the electron-electron interactions in Li are strong and it is the competition between the latter and electron-phonon interactions that leads to a very small transition temperature.

3.2 FCC Li at high pressures

Using a first-principles pseudopotential approach we study the origin of superconductivity in lithium under pressure. The Wannier interpolation based technique that allows for ultradense sampling of electron-phonon parameters throughout the Brillouin zone was employed. The electron-phonon coupling strength as a function of pressure was calculated, precisely resolving many of the fine features of its distribution. The contributions to coupling arising from the Fermi surface topology, phonon dispersions and electron-phonon matrix elements were separately analyzed. It is found that of the constituent components, the electron-phonon matrix elements are the most sensitive to pressure changes, and a particular phonon is responsible for high values of coupling. Additionally, the distribution of matrix elements over the Fermi surface is seen to be non-uniform and possesses a two-peak structure. Analysis of the Eliashberg spectral function $\alpha^2F(\omega)$ shows a considerable increase of spectral weight in the low-frequency region with the application of pressure. We estimate the superconducting transition temperature and find that the obtained values are in good accord with experiment.

3.2.1 Motivation

Lithium has attracted particular attention because it is a simple metal that exhibits a complex phase diagram. At ambient conditions it is a very nearly free-electron bcc metal [75] and its Fermi surface shows little deviation from a sphere. It may be expected that lithium would become more free-electron like with pressure increase. Experiments show, however, that when temperature is decreased or pressure is applied, Li undergoes several structural transitions and becomes superconducting [61, 62, 66–69].

In the bcc structure at atmospheric pressure, it has been found that the superconducting phase transition occurs at temperatures below the millikelvin range [61]. For non-zero pressures, Li begins to show superconductivity at pressures near 20 GPa in the fcc phase and exhibits a maximum transition temperature of 14 K at 30 GPa [67–69], making it among the highest T_c elemental superconductors. Further pressure increases beyond 30 GPa lead to structural transitions which lower T_c [70]. Additionally it was recently shown that at around 70 GPa, Li undergoes a metal-to-insulator transition [71] while resistivity increases with pressure have also been observed for shock-wave experiments [76].

Previous theoretical studies indicate that the electron-phonon coupling strength in lithium is substantial [37, 52, 57–60]. A large electron-phonon coupling strength for the bcc structure was first calculated from the empirical pseudopotential method and then in a first-principles pseudopotential approach [37, 52], while the

total electron-phonon couplings in both bcc and fcc phases has been previously analyzed. Significantly higher superconducting transition temperatures than experimentally observed have been predicted using the calculated coupling strengths for multiple structures of Li [57]. It was found that the Fermi surface topology plays a crucial role in the onset of superconductivity. Unlike the case of bcc Li, Fermi surface nesting appears to be important in the fcc phase. Several features which include phonon softening with pressure, a peak in the nesting function near the Brillouin zone (BZ) edge, and strong coupling to specific phonons have been suggested as the origin of superconductivity in Li under pressure [58, 59]. In previous electron-phonon reports it has been suggested that a very fine BZ sampling is necessary to calculate the total coupling parameters in pressurized Li with high precision [58–60, 77]. Interestingly, studies under extreme pressures indicate that the electronic structure of Li evolves into a paired insulating state which gives an upper limit to the pressure at which superconductivity may be observed [44, 71].

In this work we study the pressure evolution of the total electron-phonon coupling for the monatomic fcc phase of Li in the 8-36 GPa range. Applying a method based on first-principles calculations and subsequent Wannier interpolation techniques, we have resolved the fine features of the coupling strength λ throughout the BZ. We analyze λ in terms of the effective contributions from three different terms: Fermi surface nesting, phonon frequencies and electron-phonon matrix elements. The Eliashberg spectral function $\alpha^2F(\omega)$ is obtained and the superconducting transition temperature is calculated through the modified McMillan equation [26]. We also discuss the possibility of routes to higher T_c.

3.2.2 Results

The results presented here are for fcc Li at five pressures: 8, 14, 20, 30 and 36 GPa. The relative compressions corresponding to these pressures are 0.73, 0.64, 0.57, 0.51, 0.48 respectively. Using the generated pseudopotential, we find good agreement with the room temperature experimental equation of state [66], and slope $\frac{\delta P}{\delta V}$. It is well known that LDA slightly underestimates equilibrium bond lengths and for a given value of atomic volume the experimental pressure is about 2 GPa higher than our LDA value. The pressures listed here are those from LDA calculation.

There exists a widely accepted consensus that Li is an electron-phonon superconductor, so one should expect that the experimental rise in superconducting transition temperature would arise from an increase in electron-phonon coupling. Following the decomposition of $\lambda_{\vec{Q},\nu}$ into the three primary contributions, we start by analyzing how pressure affects the Fermi surface nesting function $\xi_{\vec{Q}}$. From

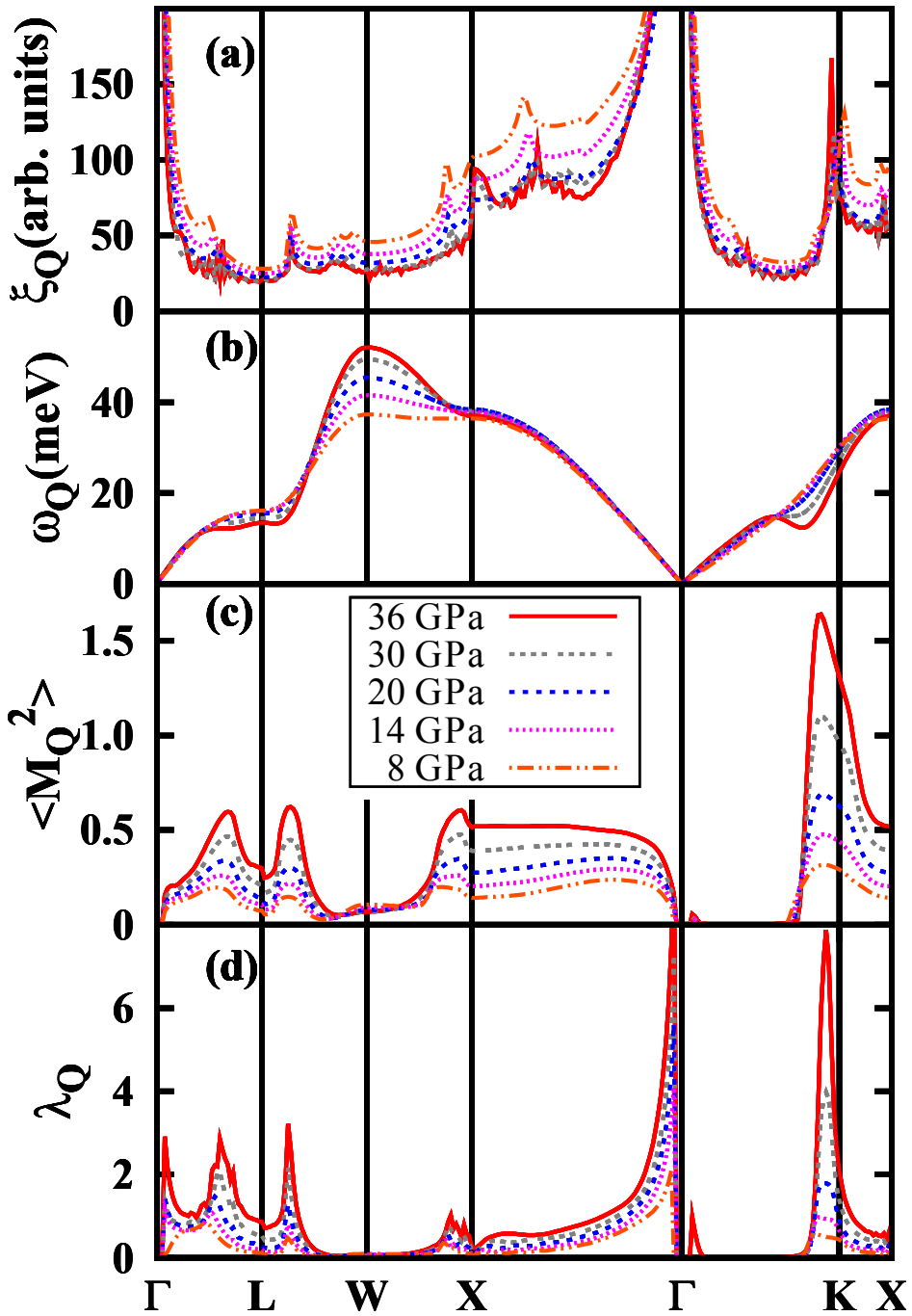

Figure 3.4: (a) The Fermi surface nesting function $\xi_{\vec{Q}}$, (b) phonon dispersions $\omega_{\vec{Q}}$, (c) average matrix element squared $M^2_{\vec{Q}}$ and (d) electron-phonon coupling $\lambda_{\vec{Q}}$ for fcc Li along the path inside the Brillouin zone. (b), (c), (d) are given for lower transverse mode $T1$. In (c) the dimensions of matrix elements are $meV^2 \times 10^3$.

Figure 3.4(a) it can be seen that although pressure does affect $\xi_{\vec{Q}}$, the nesting function is in general suppressed as pressure increases. This is true for nearly all Q-vectors inside the BZ with the exception of a small region around the K-point which shows a definite increase in the Fermi surface nesting function. This increase alone is clearly not enough to account for the experimental rise in T_c seen with the application of pressure. Therefore, we conclude that the nesting function which does not vary strongly with pressure does not contribute significantly to the increase in $\lambda_{\vec{Q},\nu}$.

We have calculated that most of the electron-phonon coupling strength in Li comes from the lower transversal mode $T1$. Therefore, we concentrate our analysis on this particular phonon mode. From Figure 3.4(b) we see that a softening of phonon frequencies is present around the L point of the BZ, and a more significant softening occurs along the Γ-K direction. From Eq. (2.14) the coupling is expected to increase as phonon frequencies are softened. Indeed, this is visible on Figure 3.4(d). An examination of the softening of $\omega_{\vec{Q}}$ near the symmetry point K leads to the conclusion that a simple scaling of lambda by the frequency cannot completely account for the large increase in coupling found in this part of the BZ. On the other hand, the response of the average matrix elements to pressure in Figure 3.4(c) is very similar to that of the wavevector dependent coupling in Figure 3.4(d). Both shows sharp increase with pressure near K.

An analysis of $M^{[\nu]}_{\vec{k},\vec{k}+\vec{Q}}$ can be performed by looking at the distribution of the magnitudes of the matrix elements over the BZ. Since the matrix elements depend on both $\vec{Q}$ and $\vec{k}$, we examine $\vec{Q}_0 = (0.6\ 0.6\ 0.0)$, which is close to the peak of the $\lambda_{\vec{Q}}$ with pressure. We calculate $M = M^{[T1]}_{\vec{k},\vec{k}+\vec{Q}_0}$ on a 200x200x200 k-point mesh in the BZ and filter only k-states with energy close to the Fermi level. The distribution of the matrix elements shown in Figure 3.5 has a two peak structure where a small portion of the matrix elements have values more than an order of magnitude larger than the rest. This structure persists at all pressures but the size of the matrix elements is affected strongly as pressure is increased. For higher pressures the fraction of elevated electron-phonon matrix elements is smaller but the magnitudes of these matrix elements are increased. The regions of Fermi surface where M^2 have the highest values are a small fraction of the BZ. As the pressure increases, these regions become more concentrated.

The Eliashberg spectral function obtained according to Eq. (2.16) is shown on Figure 3.6. For comparison, the phonon density of states is also presented. We see that though the higher frequency LA peak is stiffened with pressure for both $\alpha^2F(\omega)$ and $F(\omega)$ as expected, the behavior of the lower frequency TA peak differs qualitatively between these two graphs. In the $F(\omega)$ graph, the low frequency peak position varies slightly with pressure, while the peak positions coincide in the

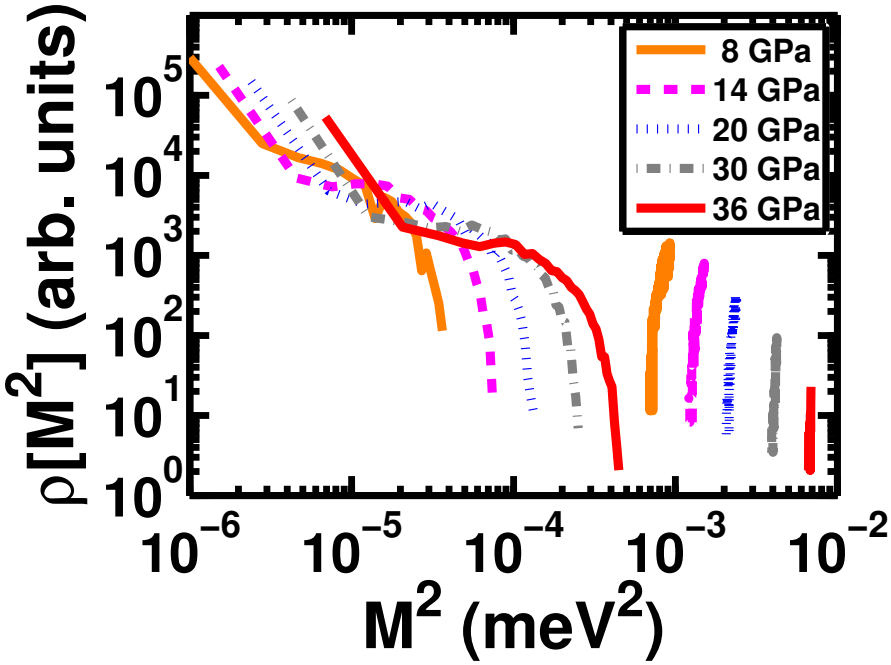

Figure 3.5: Magnitude density distribution of the electron-phonon matrix elements $M_{\vec{k},\vec{k}+\vec{Q}}$ for the lower transversal mode $T1$ of fcc Li with $\vec{Q}$ = (0.6 0.6 0.0). Only matrix elements for the k-states close to Fermi level are included. The magnitude density distribution is a histogram which plots the number of occurrences of a particular matrix element magnitude throughout the Brillouin zone as a function of that magnitude.

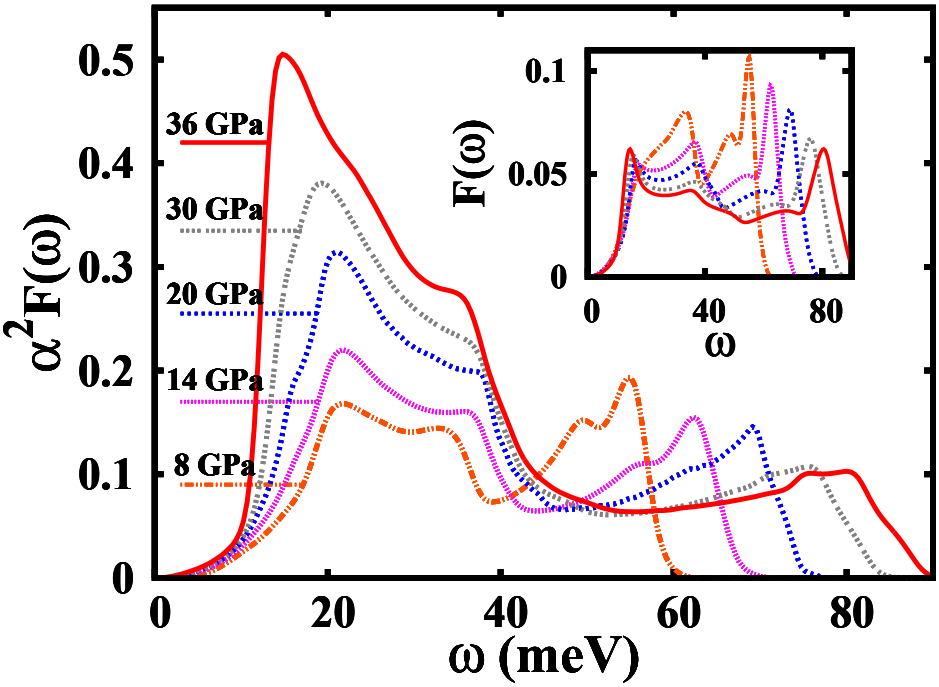

Figure 3.6: Eliashberg function $\alpha^2 F(\omega)$ for different values of pressure. Effective sampling of 50x50x50 k and q-points inside the BZ was utilized. (inset) Phonon densities of states $F(\omega)$ for the same pressures.

spectral function, the magnitude of the coupling, $\alpha^2 = \alpha^2 F/F$ is significantly amplified as pressure is applied. This increased spectral weight in the low-frequency region is primarily responsible for the higher values of average coupling λ. Once again, this observation emphasizes the importance of the coupling matrix elements on the increased transition temperature in Li under pressure.

An enumeration of certain frequency moments of the Eliashberg spectral function and the resulting estimated values of the superconducting transition temperature are given in Table 3.2. The superconducting transition temperature corresponding to the calculated electron-phonon coupling parameter has been obtained using the modified McMillan equation [26]. The total electron-phonon coupling strength λ, logarithmic and average square frequencies [9] $\omega_{\log}$ and $\langle\omega^2\rangle^{1/2}$ are consistent with previous calculations in [58–60, 77]. Because of the ultra-fine sampling of the BZ our results are well converged with respect to the summation over the BZ. Small features that were previously difficult to study have been resolved. We see that both logarithmic and square average frequencies decrease monotonically with pressure, arising from the shift of spectral weight to lower frequencies. On the other hand, the average coupling strength λ increases from 0.39 at 8 GPa to 1.10 at 36 GPa, resulting in a dramatic increase in T_c.

P(GPa)	ω_{log}	$\langle\omega^2\rangle^{1/2}$	λ	$T_c(\mu^* = 0.13)$	$T_c(\mu^* = 0.2)$
8	308	378	0.39	0.5	0.01
14	293	376	0.49	2.0	0.3
20	288	373	0.66	6.8	2.7
30	274	360	0.83	12.2	6.8
36	255	341	1.10	20.0	14.2

Table 3.2: Pressure evolution of different order frequency moments of spectral function $\alpha^2F(\omega)$. We show the total coupling strength λ, as well as the logarithmic and square average frequencies (in K). The superconducting transition temperature (T_c, in K) is estimated using the Allen-Dynes formula [26] with a Coulomb parameter μ^* given above.

The superconducting equation of state for Li is plotted in Figure 3.7 where theoretical results from this work are given together with experimental results [67–69]. Good agreement is observed in the region from 20 to 30 GPa where the different experimental results are consistent with each other. Outside of this pressure region, there are some discrepancies among experimental results.

3.2.3 Discussion

It has been suggested that Fermi surface nesting plays crucial role in the onset of superconductivity in fcc lithium [58]. In this work we observe the nesting to be important and indicative of increases in coupling $\lambda_{\vec{Q}}$. However, the change in the nesting function with pressure is seen to be much less than what is necessary to account for the increase in electron-phonon coupling strength evidenced by the increase in the superconducting transition temperature. This suggests that the pressure affects phonons more strongly than it does affect the Fermi surface topology of Li. In other words, it can be said that the Fermi surface topology in the fcc phase creates necessary conditions for superconductivity to appear, whereas applying pressure adds coupling strength, thereby driving the transition temperature up.

The origin of increasing electron-phonon interactions can be seen by a large deformation potential caused by particular phonons as shown in our calculations. To understand this, it is worthwhile to consider what happens when Li atoms are pushed close together by pressure. It has been suggested that the high pressure pairing in lithium results from a redistribution of the charge density [44]. As pressure is applied, the 2s orbitals eventually begin to overlap and at some point the mutual repulsion causes the electrons to occupy more favorable interstitial regions between Li dimers. This is similar to a Peierls'-type transition

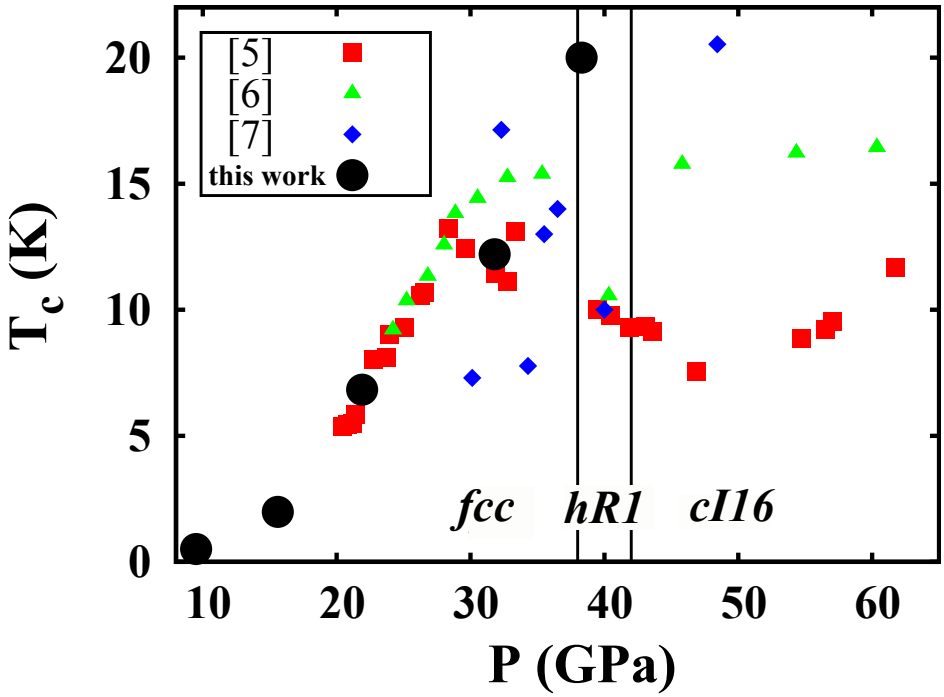

Figure 3.7: Superconducting Temperature vs. Pressure phase diagram for Li. On the graph "[5]","[6]" and "[7]" correspond to experimental data from [67–69] respectively. Calculated results from this work are based on Allen-Dynes equation [26] with $\mu^* = 0.13$. Proposed phase stability boundaries from ref. [70] are indicated by vertical lines.

and could account for the theoretically predicted $s - p$ transition [58, 78] where p-type orbitals lower the total energy resulting in the appearance of paired-type structures ($cI16$). The paired structures are favorable as they tend to maximize the interstitial volume of the unit cell. If we assume that the described process is smooth, it is natural to suggest that the change in elecronic structure with pressure also strongly affects the lattice dynamics. These affected dynamics may be the cause of higher electron-phonon coupling and eventually the structural transition associated with the $T1$ phonon softening. Experimental measurements of the pressure dependence of resistivity show a monotonic continuous trend in the region below 40 GPa [71]. This is consistent with the above assumption of continuous transformation of electronic structure under pressure.

The two peak structure of the electron-phonon matrix elements indicates that there are areas of BZ which have much stronger coupling matrix elements, differing by an order of magnitude or more. We have studied the magnitude density distribution of $\lambda_{\vec{Q}}$ and observe a structure consistent with the two peak graph of Figure 3.5. The latter distribution has one peak in the low $\lambda_{\vec{Q}}$ region and a sec-

ond, softer peak in the higher coupling region arising from these stronger matrix elements. Conversely, the same analysis of $\xi_{\vec{Q}}$ shows no interesting structure; the nesting function $\xi_{\vec{Q}}$ appears to be normally distributed. One possible explanation of the nature of the non-uniform distribution of matrix elements may be that the separate couplings come from the different nature of the electrons near the Fermi level. The shapes of the electronic eigenstates $\langle\vec{k}|$ and $\langle\vec{k}+\vec{Q}|$ and the overlap integral between them were analyzed for $\vec{k}$-s belonging to the stronger-coupling peak and show little variance with pressure. Therefore the increase in matrix element strength appears to result from the complex interaction of the electronic states with the particular $T1$ phonon perturbation.

It is of interest to discuss the value of Coulomb pseudopotential we have used in Table 3.2. Previously it has been suggested that higher values for μ^* are necessary to correctly describe Li [59, 74]. The estimate of $\mu^* \approx 0.22$ was proposed based on the comparison of Migdal-Eliashberg theory calculations of λ with McMillan equation based results for the superconducting transition temperature [59]. Before the superconductivity in Li was experimentally found, it had been proposed that the value of Coulomb pseudopotential for Li at ambient conditions should be greater that 0.1 [74]. Additionally, it follows from the logic of [74] that pressure increases would decrease μ^*. However, we are not aware of any direct first-principle calculation of Coulomb parameter for Li, and specifically Li under pressure. Previous calculations on metals which exist in the literature provide values which are consistent with $\mu^* = 0.13$ we employ [36, 73]. Using this value a good agreement with the experimentally measured T_c is found. We have also included estimated T_c for $\mu^* = 0.20$ for comparison in Table 3.2.

The trend of the superconducting transition temperature increase of 1 K/GPa in the fcc phase in the 20-30 GPa region is promising for a higher temperature superconductor. Unfortunately, as the pressure is increased past 30 GPa, a complete softening of the $T1$ phonon branch along the $\Gamma - K$ direction occurs. At this point the fcc crystal becomes unstable and likely transforms to the $hR1$ phase [70] preventing Li from reaching a higher T_c. We therefore offer a suggestion that by applying uniaxial stress along the same direction as the soft phonon eigenvector it may be possible to suppress the structural phase transition allowing for higher transition temperatures.

3.2.4 Summary

We investigated the origin of superconductivity in fcc lithium from first-principles by considering the pressure evolution of the electron-phonon coupling parameter

and its constituent elements. We found that superconductivity arises from pressure increased electron-phonon interaction and is highly affected by the topological features of the Fermi surface. We confirm that the lower transversal mode is responsible for over half of the coupling and specifically the phonon modes along Γ-K direction play the biggest role. We found that the electron-phonon matrix elements were the most sensitive to pressure of any contribution we examined. The matrix elements whose magnitudes depend strongly on the location in the BZ indicate a possibility of electron-phonon coupling arising from two distinct types of interactions having significantly different strengths. Our calculated superconducting transition temperatures as function of pressure are in good agreement with the available experimental data.

3.3 Li-intercalated borocarbides

We explore the electron-phonon coupling and possible superconductivity in Li-intercalated borocarbide materials using a precise Wannier interpolation-based first-principle technique. We find a T_c of 36.8 K for previously suggested superconductor Li_2B_3C, however we also propose a new material $Li_4B_5C_3$ with an estimated T_c of 16.8 K. Replacing BC layers with BC_3 in Li_2B_3C allows the π electronic states to be dominant at the Fermi level for $Li_4B_5C_3$. We analyze wavevector-resolved electron-phonon coupling parameters and suggest that $Li_4B_5C_3$ may be more suitable for experimental fabrication than Li_2B_3C.

3.3.1 Motivation

Graphite-like layered materials intercalated with alkali- or alkali-earth metals are well known superconductors. Since the discovery of KC_8 [79], superconducting graphite intercalation compounds with various transition temperatures T_c up to 15.1 K were reported [80–88]. Another well known superconducting material with a similar crystal structure is MgB_2. It is known to posses the highest transition temperature (T_c = 39 K) among conventional electron-phonon superconductors [89]. This high value of T_c originates from strong coupling between electrons in σ states and B–B in-plane stretching vibrational modes [90–93].

First principles calculations suggested hole-doped lithium borocarbide (LiBC) as a possible candidate for a high temperature (∼100 K for $Li_{0.5}BC$) superconductor [94]. The same study pointed out a similarity between the superconducting mechanisms in MgB_2 and LiBC. The latter is an insulator [95], but it is predicted that hole-doping by removing lithium atoms induces electrons into the σ bands of the BC layer and makes the resulting material metallic. The σ-band electrons strongly couple with the in-plane phonons which produce a high T_c [94]. The introduction of lithium vacancies through doping causes structural instabilities and considerable changes in the electronic properties [96]. These effects may explain why superconducting LiBC has not been found in experiments [96–99]. Recently, however, the possibility of hole-doping of LiBC by replacing carbon atoms with boron atoms was suggested [100, 101].

In this work we study the electron-phonon coupling in $Li_xB_yC_z$ compounds within the pseudopotential density functional theory approach. First we compute the electron-phonon coupling constants of Li_2B_3C on a dense grid inside the Brillouin zone. An interpolation technique utilizing maximally localized Wannier functions is used [102]. We obtain an average electron-phonon coupling constant λ value of 1.18 and estimate the superconducting transition temperature T_c = 36.8 K using Mcmillan's equation.[26]. In addition, we replace the BC layers with the BC_3

Table 3.3: Structural parameters of Li_2B_3C and $Li_4B_5C_3$. The lattice constants a and c, and the height of lithium atoms are listed. The lithium height is 0.25/0.75 when the covalent bonded layers and the lithium atoms are equidistantly aligned along the direction perpendicular to the layers. The distance between the lithium layer and the nearest-neighbor BC layer is shorter than the distance between the lithium layer and the nearest-neighbor boron layer both for Li_2B_3C and $Li_4B_5C_3$.

	a (Å)	c (Å)	Li positions
Li_2B_3C	2.826	7.234	0.254/0.746
$Li_4B_5C_3$	5.519	7.384	0.271/0.729

layers in Li_2B_3C and suggest a new possible superconducting material $Li_4B_5C_3$ with $\lambda = 0.62$ and $T_c = 16.8$ K. The physical properties of bulk BC_3 have been studied extensively [103–106] since it was first synthesized in 1986 [107]. We suggest, therefore, that the fabrication of $Li_4B_5C_3$ may be easier to achieve than Li_2B_3C.

3.3.2 Results and Discussion

3.3.2.1 Structural properties

Optimized crystal structures of Li_2B_3C and $Li_4B_5C_3$ are shown in Fig. 3.8. The Li_2B_3C is constructed by replacing every other BC layer in pure LiBC by a layer of hexagonal boron atoms, whereas the $Li_4B_5C_3$ is made by further replacing the remaining BC layers by BC_3. The layer-by-layer structure of the latter material consists of a layer of BC_3, a layer of Li-intercalants and a layer of hexagonal boron atoms. There are 6 and 24 atoms in the unit cells of Li_2B_3C and $Li_4B_5C_3$, respectively.

The structural parameters a, c, and lithium positions in the crystal coordinates are listed in Table 3.3. The introduction of the BC_3 layer shortens the in-plane lattice constant a compared with Li_2B_3C by 2.4 % since a C–C bond tends to be shorter than a B–C bond in sp^2-bonded systems. The distance between a lithium layer and the nearest-neighbor boron layer in $Li_4B_5C_3$ (1.69 Å) is shorter than the distance in Li_2B_3C (1.78 Å).

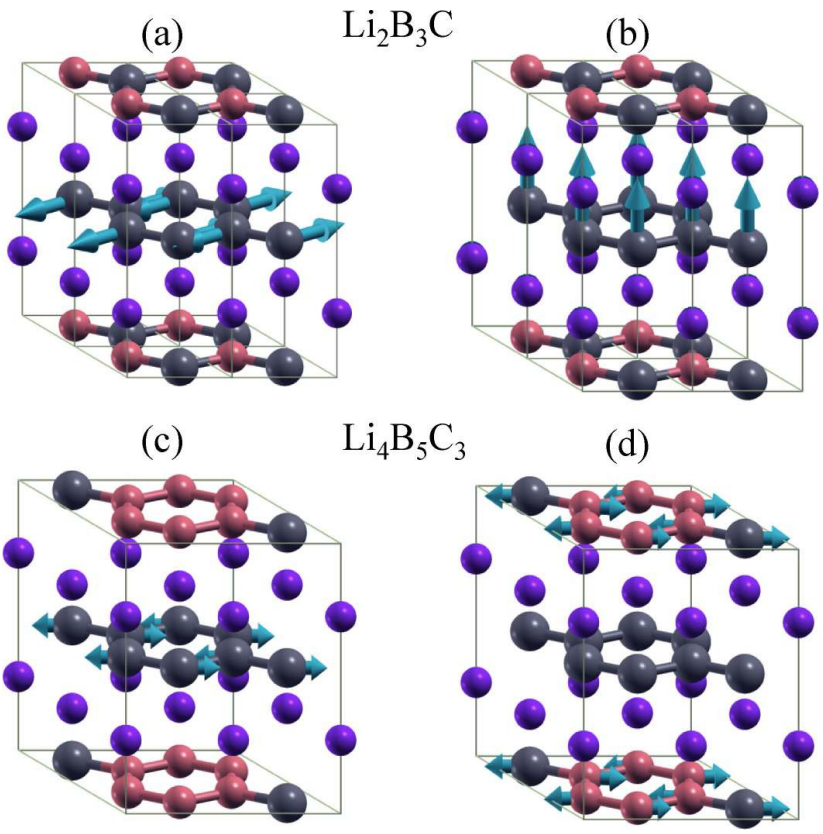

Figure 3.8: Crystal structures of Li_2B_3C (top panels (a),(b)) and $Li_4B_5C_3$ (bottom panels (c),(d)). Lithium, boron, and carbon atoms are represented by purple, gray, and peach color spheres, respectively. The arrows show displacement vectors of the vibrational modes which strongly couple with electrons: (a) the E' mode at the Γ point in the first Brillouin zone, (b) the B_2 mode at the M point, (c) the E_{2g} B–B stretching mode at the Γ point, and (d) the E_{2g} B–C and C–C stretching mode at the Γ point.

3.3.2.2 Electronic structure

The band structures and the electronic densities of states of Li_2B_3C and $Li_4B_5C_3$ are shown in Fig. 3.9. For Li_2B_3C our results are in agreement with those of the previous work [100]. In particular, we confirm that the σ-states of the boron layer provide the largest contribution to the density of states near the Fermi energy.

The band structure of $Li_4B_5C_3$ in Fig. 3.9 has a multitude of states at the Fermi energy and is complicated because of the large size of the calculation cell. The main contribution to the total density of states of $Li_4B_5C_3$ near the Fermi energy is coming from the π-states of the BC_3 layers, in contrast to Li_2B_3C. This difference in the dominant contribution to the total densities of states is consistent with the difference in the electron-phonon coupling as will be discussed later.

3.3.2.3 Phonons

The phonon densities of states are presented in Fig. 3.10. For Li_2B_3C our calculations show that the spectral weight is concentrated in two main regions: a low-energy region at 20-60 meV and a high-energy region at 100-130 meV. The high-energy peaks correspond to the in-plane B–B bond-stretching modes (see Fig. 3.8(a)). The lower energy peak has contributions from out-of plane motions of boron and carbon atoms, as well as the Li displacements (see example in Fig. 3.8(b)).

In $Li_4B_5C_3$, the phonon density of states behaves rather similarly: a low-energy region at 20-60 meV and a higher-energy region at 100-130 meV contain the accumulated spectral weight. The high-energy peaks now correspond to B–B, B–C and C–C in-plane bond-stretching modes (see Fig. 3.8 lower panel).

3.3.2.4 Electron-phonon coupling

Our results for the Eliashberg spectral functions α^2F (Eq. 2.16) are shown in the Fig. 3.10. The spectral function for Li_2B_3C has peaks at $\sim$30, $\sim$50, $\sim$100 and $\sim$120 meV. These findings are consistent with previously obtained theoretical estimates [100]. The two peaks at low frequencies originate from the out-of plane boron-layer and lithium-layer vibrations and have large contribution to the average coupling (because of the ω^{-1} part in Eq. 2.19). The two peaks at high frequencies arise from the B–C and B–B in-plane vibrations and are less important for the average coupling λ.

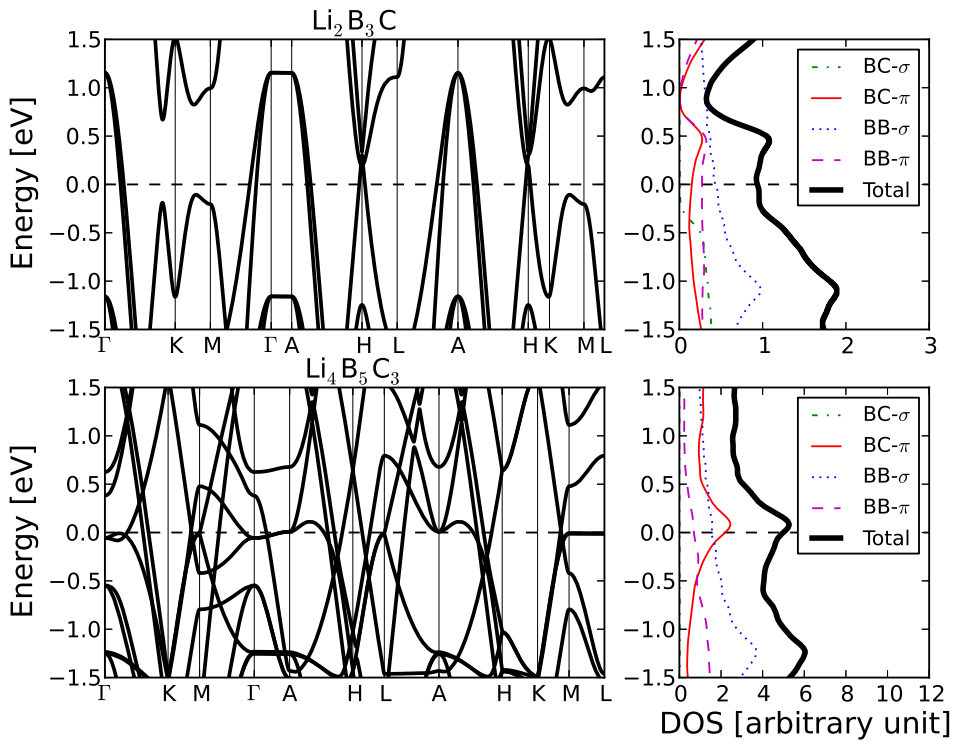

Figure 3.9: Band structures and partial density of states of Li_2B_3C (top panels) and $Li_4B_5C_3$ (bottom panels) near the Fermi energy (the Fermi energy is set to 0 eV). The high symmetry points are marked on the horizontal axis of the band structure plots by different length scales corresponding to the different a and c lattice constants. The black thick solid lines in the right panels show the total densities of states. The green chain, red solid, blue dotted, and magenta dashed lines represent the contributions from the σ-state in the BC layer, the π-state in the BC layer, σ-state in the boron layer, and π-state in the boron layer, respectively. The contributions from lithium atoms are small near the Fermi energy.

We argue that the enhancement of the spectral weight in α^2F for the low-frequency region in Li_2B_3C is likely to complicate the fabrication of the material in experiment. This is because of the tendency of strongly-coupled low-frequency acoustic modes to get soft and drive a structural transition [49].

Fine sampling of the Brillouin zone is essential for a precise calculation of α^2F. Therefore we explain the fact that the previous study in Ref. [100] found less enhancement in the low-frequency region of the spectral function by a relatively coarse sampling compared to the one utilized in this work.

The spectral function for $Li_4B_5C_3$ has peaks in the 30-60 and the 110-130 meV regions. The nature of the vibrations forming these peaks is the same as for Li_2B_3C. The main differences include much lower spectral weight in the 0-60 meV region for $Li_4B_5C_3$ and a slightly increased weight in the 110-130 meV area. These differences account for a smaller average coupling λ in $Li_4B_5C_3$.

3.3.2.5 Nesting function

In the Figure 3.11 the wavevector-resolved electron-phonon coupling $\lambda_{\vec{Q}} = \sum_\nu \lambda_{\vec{Q},\nu}$ and the nesting function along a path inside the phonon Brillouin zone are plotted. The nesting function reflects the probability of an electron at the Fermi level to be scattered by a wavevector $\vec{Q}$ [58],

$$\xi_{\vec{Q}} = \frac{1}{N_k} \sum_{\vec{k}} \delta(\epsilon_{\vec{k}})\delta(\epsilon_{\vec{k}+\vec{Q}}). \tag{3.2}$$

Where N_k is the total number of $\vec{k}$-vectors included in the sum, and $\delta(\epsilon_{\vec{k}})$ is the energy conserving Dirac delta-function.

For Li_2B_3C, as seen from the figure, $\lambda_{\vec{Q}}$ has peaks at M and L, where no increase in nesting is present. This can be explained by the increase in the $\lambda_{\vec{Q},\nu}$ arising from the acoustic phonon frequency softening at these high symmetry points.

In all of our calculations for $Li_4B_5C_3$ the nesting function $\xi_{\vec{Q}}$ is nearly proportional to the electron-phonon coupling $\lambda_{\vec{Q}}$, as can be seen from the figure. Therefore we conclude that the material is far from the phonon-softening which can induce a structural instability, and the electron-phonon matrix elements are relatively constant throughout the Brillouin zone.

3.3.2.6 Superconducting parameters

Table 3.4 shows the parameters used in our estimate of the superconducting transition temperature T_c. We estimate the superconducting transition temperature

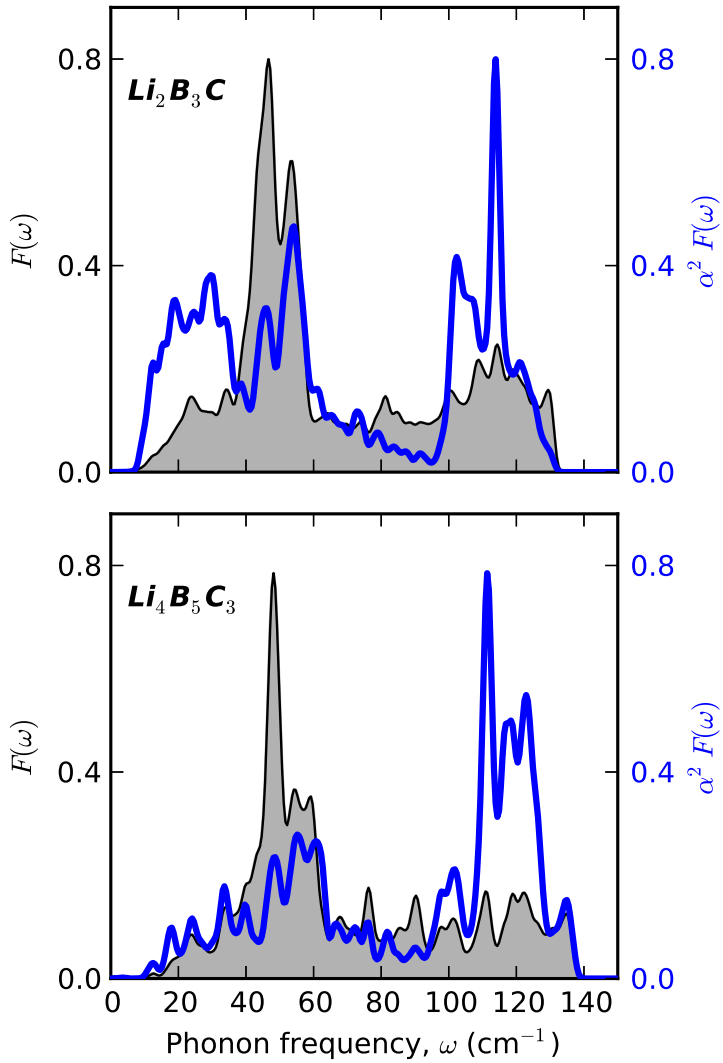

Figure 3.10: Phonon densities of states $F(\omega)$ (black solid line and the gray-shaded area below) and the Eliashberg spectral functions $\alpha^2 F(\omega)$ (blue line) for Li_2B_3C and $Li_4B_5C_3$ calculated in this work. The $F(\omega)$ is given in arbitrary units.

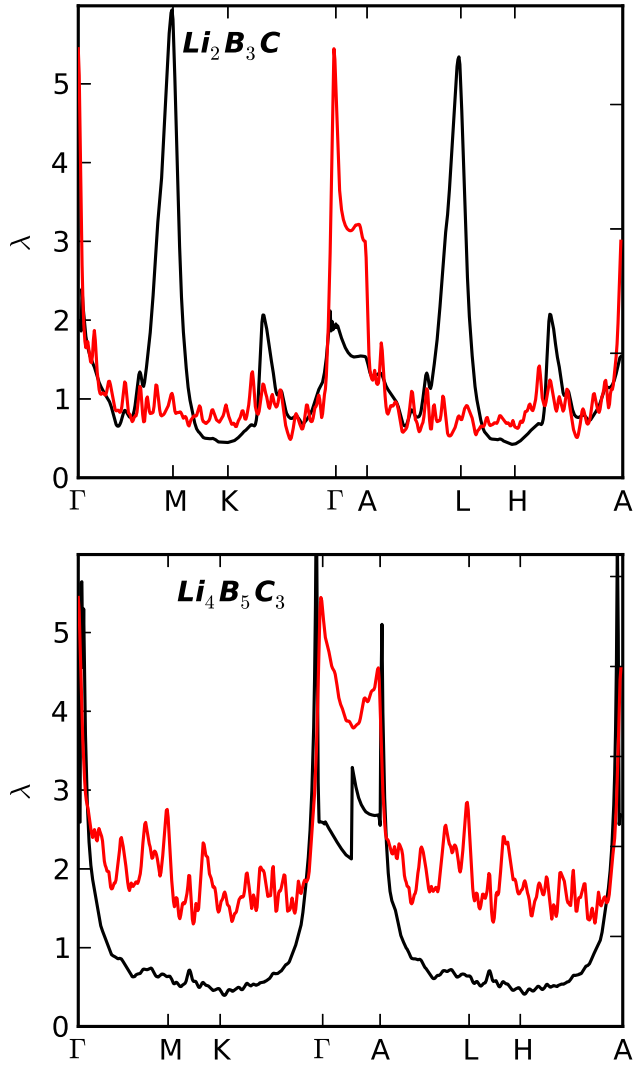

Figure 3.11: Wavevector-resolved electron-phonon coupling $\lambda_{\vec{Q}}$ (solid black) and the Fermi surface nesting (red) function (as explained in Ref. [9, 58], for instance) for a path inside the corresponding Brillouin zone for Li_2B_3C and $Li_4B_5C_3$. The nesting is given in arbitrary units.

Table 3.4: Theoretical estimate of the superconducting transition temperature T_c obtained using the modified McMillan formula [26] for two values of the Coulomb parameter μ^* given. We also show the square and logarithmic frequency moments of the Eliashberg spectral function [9] ($\sqrt{<\omega^2>}$ and $\omega_{\log}$ respectively), are given along with the the average electron-phonon coupling strength λ. The error-bars on λ are ± 0.05

	$\sqrt{<\omega^2>}$ (K)	$\omega_{\log}$ (K)	λ	T_c (K) μ^*=0.1	T_c (K) μ^*=0.0
Li_2B_3C	613	380	1.18	36.8	55.5
$Li_4B_5C_3$	897	638	0.62	16.8	37.6

(T_c, in K) using the modified McMillan formula [26]. In the table we show the estimated T_c using a Coulomb parameter μ^*=0.0 and 0.1.

For Li_2B_3C we obtain λ=1.18, which is slightly smaller than what was found in Ref. [100]. The difference is likely to be due to an enhanced level of the Brillouin zone sampling we use. We find a T_c of 36.8 K for $\mu^* = 0.1$ (55.5 K for the upper limit of $\mu^* = 0$). The logarithmic and square average frequencies are 380 and 613 K respectively.

For $Li_4B_5C_3$ we obtain λ=0.62. This yields a T_c of 16.8 K for $\mu^* = 0.1$ (37.6 K for the upper limit of $\mu^* = 0$). The logarithmic and square average frequencies are 638 and 807 K respectively. $Li_4B_5C_3$ has larger frequency moments because the spectral weight for α^2F is small in the low-frequency regions. For the same reason we argue here again that $Li_4B_5C_3$ is likely to be more stable than Li_2B_3C as the acoustic low-frequency modes do not have large coupling. The small value of the coupling for the low-frequency modes suggests that this material is far from a phonon-softening-induced structural transition.

3.3.3 Summary

We have analyzed the electronic, vibrational and electron-phonon coupling properties of the Li-intercalated borocarbide compounds Li_2B_3C and $Li_4B_5C_3$. Previously suggested large value of electron-phonon coupling is consistent with our more precise approach for Li_2B_3C (λ=1.18, T_c=36.8 K) and we predict that for $Li_4B_5C_3$ λ=0.62, T_c=16.8 K. We find a decrease in spectral weight in the lower-frequency region (20-60 meV) for the Eliashberg spectral function in $Li_4B_5C_3$ compared to Li_2B_3C. Based on that finding we propose that $Li_4B_5C_3$ is less likely to be dynamically unstable and thus may be more suitable for experimental fabrication. Finally, for $Li_4B_5C_3$ we find the Fermi surface nesting function to be

nearly proportional to the electron-phonon coupling throughout the Brillouin zone, which also supports the suggestion concerning the stability of this material.

Chapter 4

Class-II superconductors

This chapter contains a discussion of the results obtained for a the non-conventional, or class-II superconductors. For these materials the mechanism responsible for the superconducting pairing is still unknown at the time of this writing. We use precise first-principle techniques based on the pseudopotential density functional theory and Wannier approximation in the way described in chapter 2 to calculate the electron-phonon coupling and associated superconducting transition temperature, to analyze the sensitivity of the electronic structure to the changes in induced magnetization and to study the spin-fluctuations-induced interaction. We present the motivation, the results and their discussion, and a short summary of findings for each case studied. A complete description of each case can also be found in [108, 109].

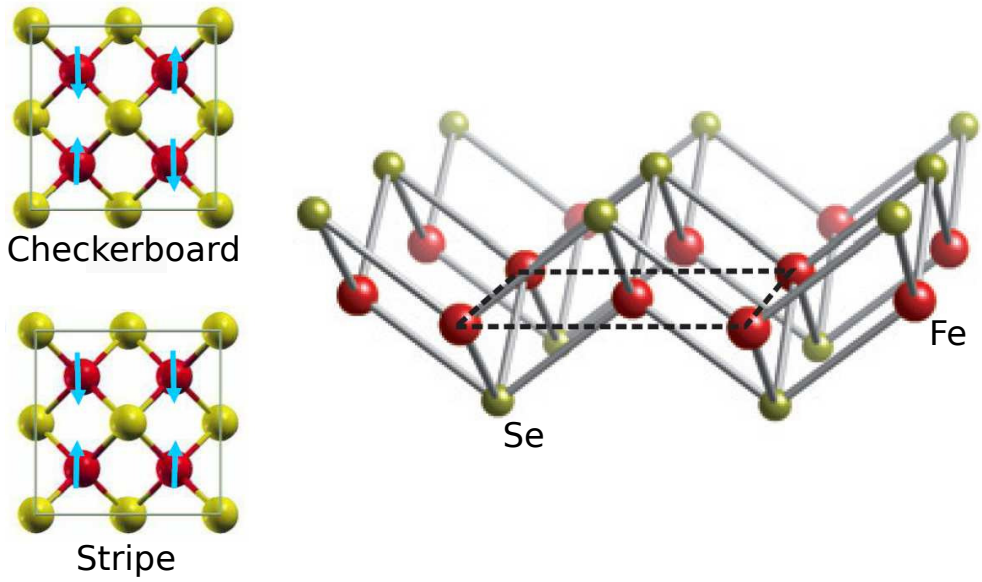

Figure 4.1: Crystal structure of FeSe (right) and antiferromagnetic spin patterns of the Fe-layer (left). Illustration adopted from [16].

4.1 Bulk FeSe and KFe_2Se_2

The effect of the static magnetic moments of iron on electron-phonon interactions in layered FeSe and KFe_2Se_2 is studied. First principle techniques based on the pseudopotential density functional approach and the local spin density approximation are utilized to calculate the bandstructures, phonon dispersions, and electron-phonon coupling properties. Our results indicate that introducing iron magnetic moments leads to significant changes in electronic structure induced by Fe-3d states near the Fermi level, to phonon frequency softening for several vibrational modes, and a dramatic increase in electron-phonon coupling for specific modes. The increase in Brillouin zone averaged coupling is about two-fold. Our estimates of superconducting transition temperatures based on the McMillan equation yield values closer to experimental results for the spin-resolved case. However, these values are not large enough to explain the observed transition temperature.

4.1.1 Motivation

One of the simplest iron-based superconducting compounds, FeSe has many characteristic properties of this group and thus can potentially be considered as a

model system for studying the electron pairing mechanism for iron-based superconductors. At ambient conditions, FeSe has a transition temperature T_c of 8 K for slightly Se-deficient samples, and the presence of superconductivity is extremely sensitive to sample stoichiometry [48, 110]. When pressure is applied the T_c grows to 27 K at 1.5 GPa and to 37 K at 9 GPa [111, 112], perhaps suggesting that lattice vibrations are playing an important role for superconductivity. Antiferromagnetic spin fluctuations are reported to be strong, although no static long-range magnetic order was found for the superconducting phase [113]. Recent reports also suggest the presence of a nodal gap [114] and an unconventional value for the isotope effect parameter [115]. Studies of FeSe monolayer systems on different substrates show significant sensitivity to interface effects and also give some signs of the presence of superconductivity above 77 K [116, 117].

A number of intercalated FeSe compounds were experimentally prepared using alkali, alkali-earth or rare-earth metals as intercalants [118, 119]. The resulting T_c is raised to above 30 K at ambient pressure. Of particular interest is the simultaneous presence of superconductivity and antiferromagnetism in these systems and its relation to the iron vacancy ordering [120, 121]. NMR experiments suggest spin fluctuations to be weak [122]. Raman spectra exhibit phonon anomalies indicative of a rather specific type of electron-phonon coupling [123]. In addition, high pressure measurements are indicative of extreme sensitivity to the nature of defects [124]. All the above give evidence for the importance of taking the effects of lattice vibrations into account when studying the possible mechanism for superconductivity in selenides.

Theoretical findings, alongside ARPES and dHVA experiments help to determine the most probable nature of the Fermi surface geometry [125, 126], even though the availability of good quality crystalline samples limits these studies. Theoretical predictions suggest that for FeSe, the Fermi surface has pockets at points Γ and M of the Brillouin zone (BZ). The intercalated compounds tend not to have the zone-centered pockets, according to both theoretical and experimental findings [127, 128]. The latter fact does not support the widely accepted $s_\pm$ superconducting gap structure model [18, 129]. Electron-phonon coupling calculations without including spin-polarization effects yield values too low to account for the experimentally observable transition temperature within the standard McMillan-Eliashberg approach [127]. When iron magnetic moments are included into the calculation, a significant increase is seen for the 122 and 111 systems [130]. Significant phonon softening was also reported for FeSe [131]. Finally, it is worth mentioning here that the many-body dynamical mean-field theory results have proposed the presence of rather strong electronic correlation [132].

In this work we study the influence of static magnetic moments of iron on electronic structure, vibrational, and electron-phonon properties of layered iron-

chalcogenide systems including bulk FeSe and K-intercalated FeSe. For the spin-resolved study we choose the checkerboard and the striped antiferromagnetic configurations (vibrational properties have been studied for FeSe only in the striped case). The latter is seen experimentally for many iron superconductors in the ordered state, while the former can be relatively simply approached from a calculation perspective. We utilize a first principle pseudopotential density functional theory and local spin density approximation based approach. Our results show significant changes in the electronic structure and clear evidence of phonon softening when spin is considered. Both of these effects lead to a doubling of the electron-phonon coupling for checkerboard spin-resolved configurations. Electron-phonon matrix elements for a particular phonon mode of A_{1g} symmetry show a dramatic increase as well. Superconducting T_c estimates were made based on the Eliashberg spectral function analysis and the McMillan's equation [26]. The T_c for the checkerboard spin-resolved case are much higher then the case when spin is not included, but the values are still one order of magnitude lower then the experimental results.

4.1.2 Results

Results given in this section are for for relaxed configurations, where the lattice constants were optimized to minimize the forces on the atoms. The reason for this approach is to study phonon properties more precisely by using a near-equilibrium configuration. Otherwise negative phonon frequencies emerge as artifacts. For FeSe, in the non-magnetic and checkerboard spin-resolved configurations, we use a 4-atom unit cell. For the striped spin-resolved configuration a unit cell twice as large with 8 atoms is used. For KFe_2Se_2 we use a 10-atom unit cell for all calculations. For FeSe we find the striped spin arrangement to be 24 mRy lower in energy then the non-magnetic one, and 6 mRy lower then the checkerboard spin-pattern. The KFe_2Se_2 unit cell in checkerboard configuration is 42 mRy lower in total energy than the non-magnetic one, and 9 mRy lower than the striped configuration.

First, we analyze the effect of iron magnetic moments on the electronic structure of FeSe. It can be seen from Figs. 4.2 and 4.3 that the non-magnetic bandstructure for bulk FeSe is similar to what was originally obtained in ref. [127]. The spin-resolved bandstructure has two main differences: there are only two bands instead of five that cross the Fermi level, and one of the two has a very small energy bandwidth. These two differences can also be clearly seen in the density of states plots in the figures mentioned. The total DOS has a peak right at the Fermi level for the spin-polarized case, whereas the width of the peak is smaller and its position is not correlated with E_F for the non-polarized configuration. The

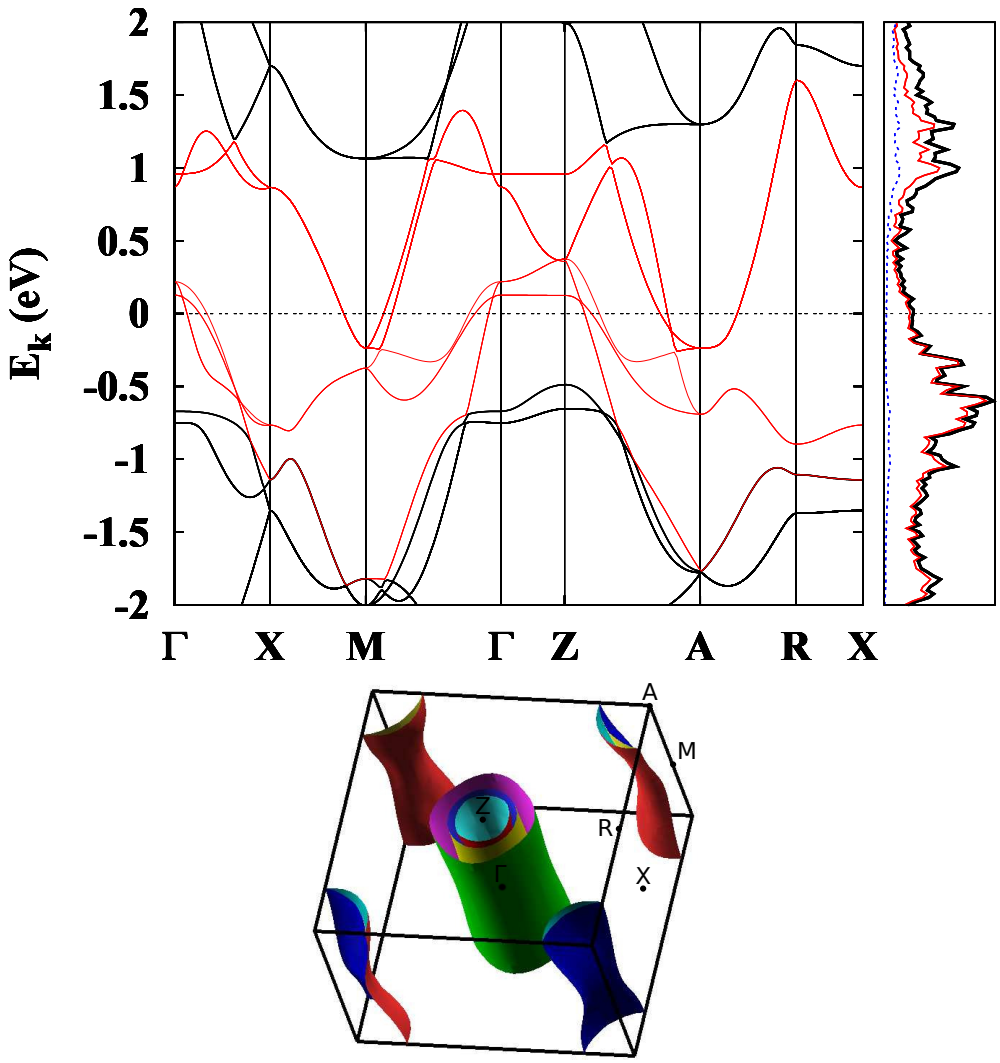

Figure 4.2: TOP(a): Electronic bandstructure of FeSe for the non-spin-polarized case. Brighter colored bands are those crossing the Fermi level. To the right the corresponding projected densities of states (in states/eV, from 0 to 12) are plotted for all atoms (black solid), Fe-3d states (red solid) and Se (blue dashed). BOTTOM(b): the corresponding Fermi Surface. The high symmetry points are given and correspond to the points along the bandstructure plot on the top.

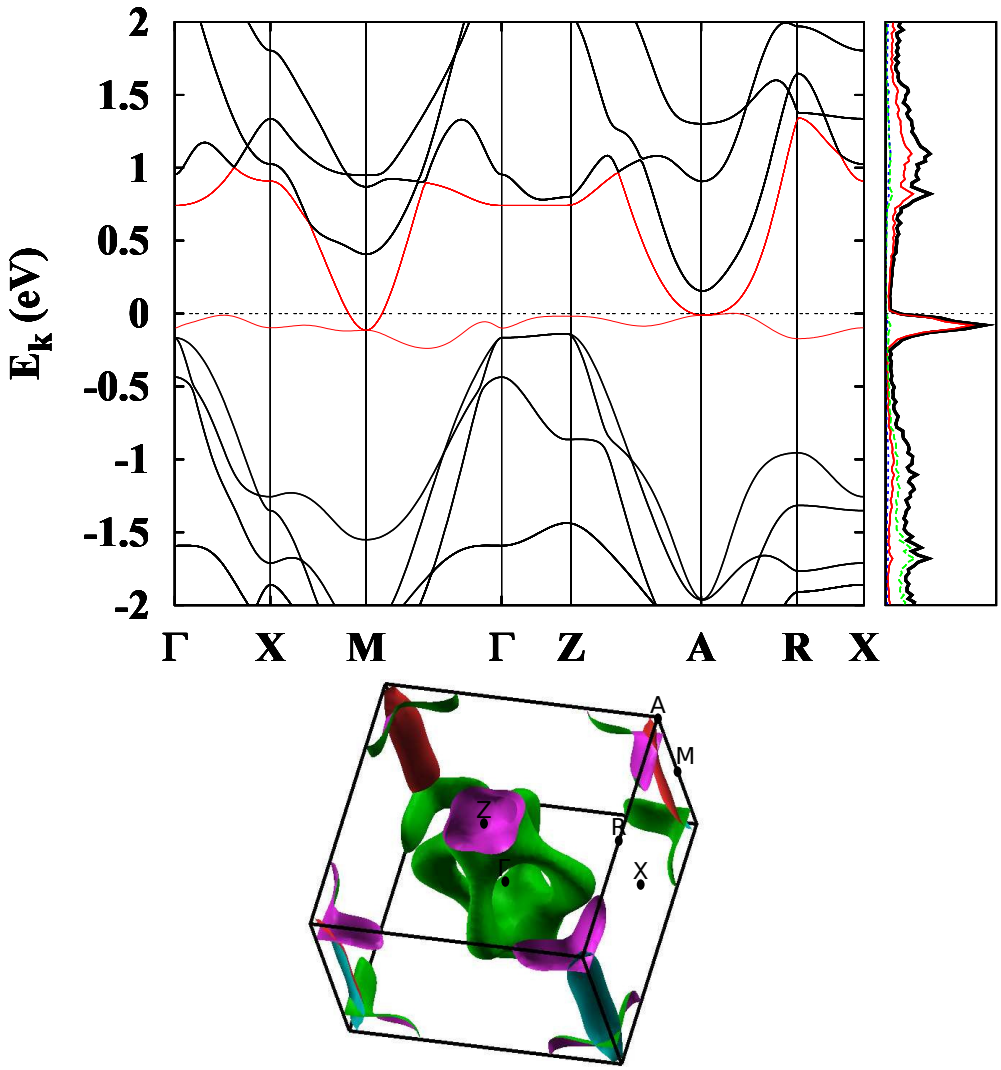

Figure 4.3: TOP(a): Electronic bandstructure of FeSe for the checkerboard spin-polarized case. Brighter colored bands are those crossing the Fermi level. To the right the corresponding projected densities of states (in states/eV, from 0 to 11) are plotted for all atoms (black solid), Fe-3d-up states (red solid), Fe-3d-down states (green dashed) and Se (blue dot-dashed). BOTTOM(b): the corresponding Fermi Surface.

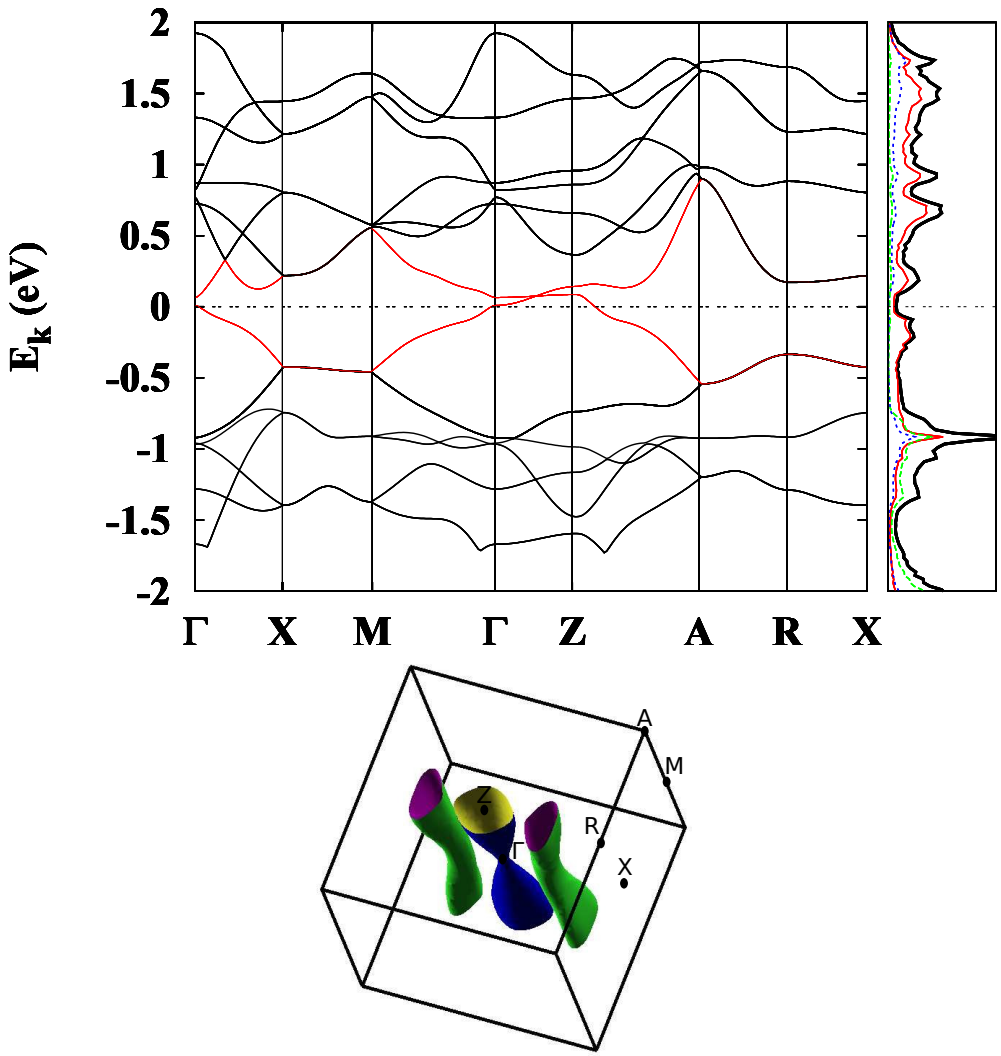

Figure 4.4: TOP(a): Electronic bandstructure of FeSe for the striped spin-polarized case. Brighter colored bands are those crossing the Fermi level. To the right the corresponding projected densities of states (in states/eV, from 0 to 15) are plotted for all atoms (black solid), Fe-3d-up states (red solid), Fe-3d-down states (green dashed) and Se (blue dot-dashed). BOTTOM(b): the corresponding Fermi Surface. NOTE: even though the striped spin-configuration has different BZ (rotated by $\pi/2$ and scaled by $\sqrt{2}$ in k_x and k_y-directions), we use the conventional cell, so the symmetry points on the wavevector path along the x-axis have the same coordinates when expressed in reciprocal lattice vectors terms as for for the non-magnetic and checkerboard BZ. Stripe direction is toward the given X point. Y point corresponding to a perpendicular to the stripe direction is not shown.

partial density of states around the Fermi level is dominated by Fe-3d states in both cases. These changes in electronic structure significantly affect the shape of the Fermi surface. The overall shape with electron pockets centered at M and hole pockets at Γ is modified. Pockets at M are still present, whereas hole pockets are now centered at Z.

The electronic properties of the striped antiferromagnetic spin-resolved configuration are summarized in Fig. 4.4. Calculation of the striped spin arrangement requires twice as many atoms in a unit cell, so the Fermi surface is a fraction of the one examined in the non-magnetic and checkerboard antiferromagnetic configurations. The Fermi surface is formed by two bands. The peak in the total density of states is located somewhat below the Fermi level and thus does not play a large role for the electron-phonon interaction. The general shape of the Fermi surface has one cylindrical pocket at the gamma point and two smaller satellite pockets next to it. The satellite pockets are aligned with the stripe direction. The pocket at Γ for the striped configuration's reduced BZ would produce pockets at both Γ and M for the BZ for non-spin-resolved and checkerboard spin systems.

Secondly, we analyze the effect of iron magnetic moments on the electronic structure of KFe_2Se_2. In Fig. 4.5 and Fig. 4.6 the non-magnetic and checkerboard spin-resolved bandstructures for KFe_2Se_2 are given. Again, the spin-resolved bandstructure has a fewer number of energy bands crossing the Fermi level and their energy bandwidths are narrowed. The same two differences can be seen when comparing the partial density of states plots. As in the case of FeSe, the total DOS has a Fe-3d states induced peak very close to the Fermi level for the spin-polarized case. Generally, we can state that the Fe-3d states are becoming more localized in energy when the spins are included. The way the shape of the Fermi surface evolves can also be seen from the above figures. Overall, the Fermi surface of KFe_2Se_2 for the spin-resolved case does not have pockets at Γ and is much better nested (has regions that amplify scattering possibilities for a particular wavevector, see [49], for example, for more explanation of the nesting function). Further discussion follows.

The electronic properties of the striped antiferromagnetic spin-resolved configuration for KFe_2Se_2 are given in Fig. 4.7. We used a unit cell containing 10 atoms to study striped spin arrangement, however the shape of the BZ is different then for the configurations mentioned in the prevous paragraph. As can be seen in the figure, the striped spin arrangement has a bandstructure similar to a hole-doped semiconductor with a rather small gap of a few hundreds of meV. The Fermi surface has two regions formed by two bands, one of which a shows significant degree of nesting. No pockets are present at the center of the BZ at Γ. On the DOS plot a sharp peak induced by Fe-3d states can be seen at about 0.7 eV below the Fermi level.

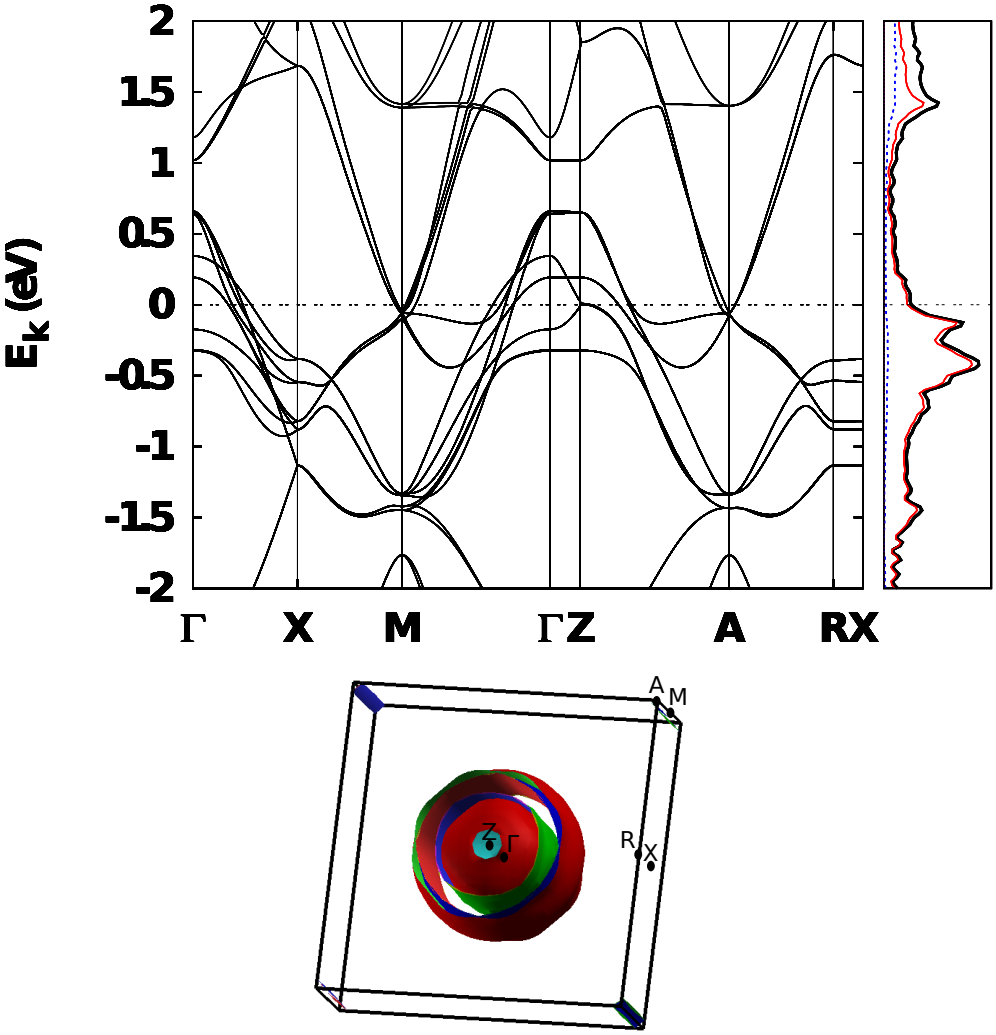

Figure 4.5: TOP(a): Electronic bandstructure of KFe_2Se_2 for the non spin-polarized case. To the right the corresponding projected densities of states (in states/eV, from 0 to 30) are plotted for all atoms (black solid), Fe-3d states (red solid) and Se (blue dashed). BOTTOM(b): the corresponding Fermi Surface.

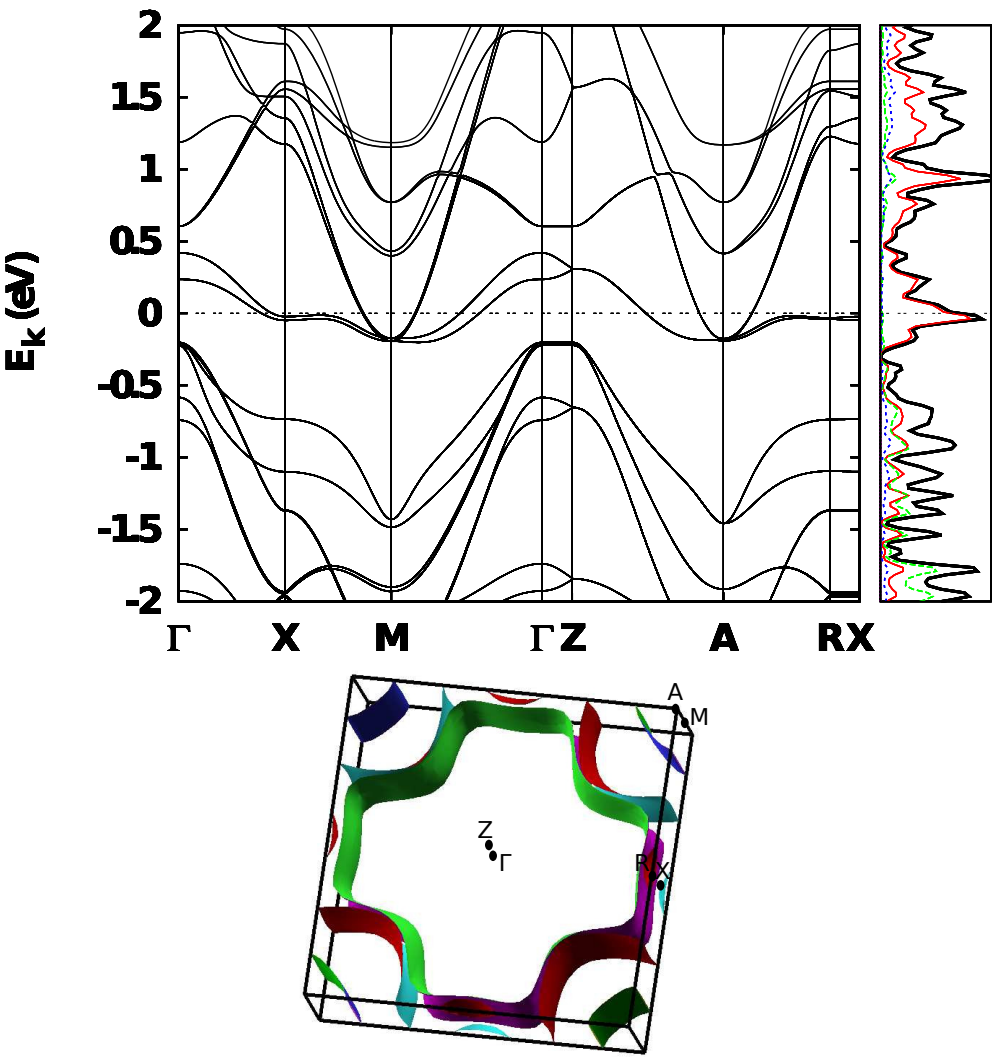

Figure 4.6: TOP(a): Electronic bandstructure of KFe_2Se_2 for the checkerboard spin-polarized case. To the right the corresponding projected densities of states (in states/eV, from 0 to 15) are plotted for all atoms (black solid), Fe-3d-up states (red solid), Fe-3d-down states (green dashed) and Se (blue dot-dashed). BOTTOM(b): the corresponding Fermi Surface. Positions of high symmetry points inside the BZ are same as for Fig. 4.2.

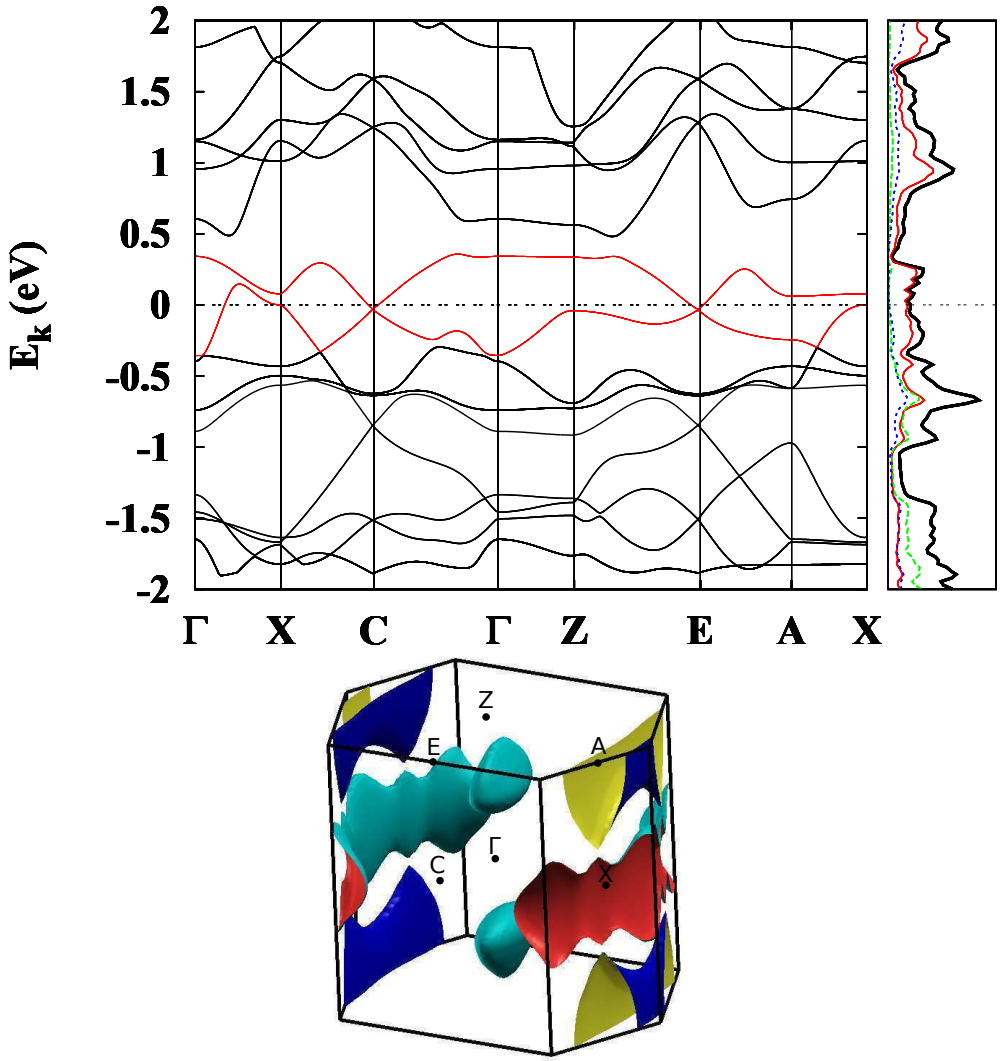

Figure 4.7: TOP(a): Electronic bandstructure of KFe_2Se_2 for the striped spin-polarized case. Brighter colored bands are those crossing the Fermi level. To the right the corresponding projected densities of states (in states/eV, from 0 to 12) are plotted for all atoms (black solid), Fe-3d-up states (red solid), Fe-3d-down states (green dashed), Se (blue dot-dashed) and K (purple dot-dashed). BOTTOM(b): the corresponding Fermi Surface. NOTE: the striped spin-configuration has monoclinic BZ due to stripe-induced lattice distortion. We use the corresponding symmetry points on the wavevector path along the x-axis, that have the same coordinates when expressed in reciprocal lattice vectors terms as for for the non-magnetic and checkerboard BZ. Stripe direction is toward the given X point.

Third, the phonon dispersions are given on Figs. 4.8, 4.9 and 4.10. For FeSe it can be clearly seen that when we compare non-spin and spin-resolved cases; there is a significant degree of softening present for the particular phonon mode having A_{1g} symmetry. This phonon branch has frequencies around 250-260 cm^{-1} for $\vec{q}$ between $\Gamma - Z$ and $\Gamma - X$ when no spin is considered. These frequencies move to below 200 cm^{-1} when iron magnetic moments are included in the calculation. Other phonon modes are affected in a similar way exhibiting overall softening, although significantly smaller in magnitude. The phonon density of states plots illustrate increased weight in the lower-frequency region, the same conclusion is true for the electron-phonon spectral function. The A_{1g} phonons yield the largest electron-phonon coupling values as well.

The phonon dispersions for FeSe in the striped spin configuration show some signs of softening, as can be seen from the density of states plot. However, the degree of this softening is not large. A peak in the Eliashberg function at about 200 cm^{-1} arises from electron-phonon coupling to the B_{3g} mode, which seems to account for about 40% of total coupling.

The phonon dispersion relations for KFe_2Se_2 exhibit similar behavior. A comparison between spin-resolved and non-spin cases shows a general softening, that most evidently can be seen for $\vec{q}$ between $\Gamma - Z$ and $\Gamma - X$. Vibrational states in the 100-150 cm^{-1} region are lowered to below 100 cm^{-1}. The latter can be derived from the comparison between the phonon density of states plots providing evidence for increasing number of phonons in the low-frequency region when spins are included. The spectral weight shift to lower frequencies is also present in the electron-phonon spectral function plots

Electron-phonon coupling values, averaged over the Brillouin zone, estimated values of the superconducting transition temperature, density of states at the Fermi level, average electron-phonon matrix element value and logarithmic averaged frequency are summarized in Table 4.1. The T_c corresponding to the calculated electron-phonon coupling parameter is obtained using the modified McMillan equation [26]. The degree of BZ sampling used suggests that the average coupling value λ is precise to within an error of 10-15%. On the other hand, precise calculation of the Eliashberg spectral function needs better sampling, so the given values of the spectral function frequency moment - ω_{log} - are rough estimates. As we see, λ increases from 0.15 for non-spin-resolved FeSe to 0.39 for checkerboard spin resolved configuration, and correspondingly from 0.19 to 0.34 for KFe_2Se_2. This leads to a T_c of 1.1 K and 0.2 when iron moments are included in the calculation, and for practically zero values in the opposite case. The striped spin-resolved FeSe case has a coupling value of 0.16 and thus zero T_c. We show that using the commonly used value of Coulomb repulsion parameter $\mu^* = 0.1$ even for the checkerboard spin-resolved case we do not achieve consistency with the

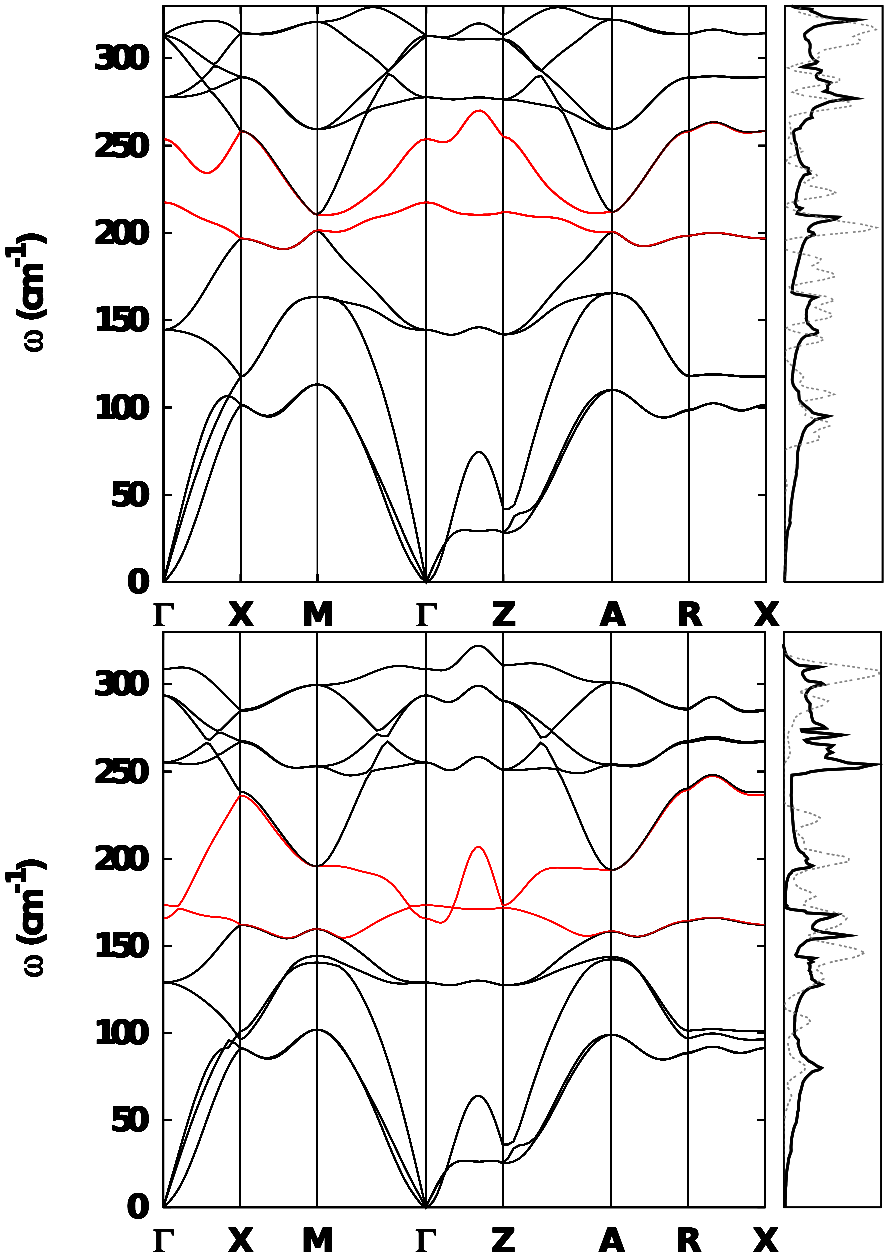

Figure 4.8: Phonon dispersions of FeSe for non the spin-polarized (TOP(a)) and the checkerboard spin-polarized (BOTTOM(b)) configuration. Phonon density of states (solid) and Eliashberg spectral function (dashed) are given to the right (in states/cm^{-1}, from 0 to 0.2 - non-magnetic, in states/cm^{-1}*(2) - spin-resolved, from 0 to 0.4). Bands showing the largest degree of softening are shown in red (brighter) color to guide the eye.

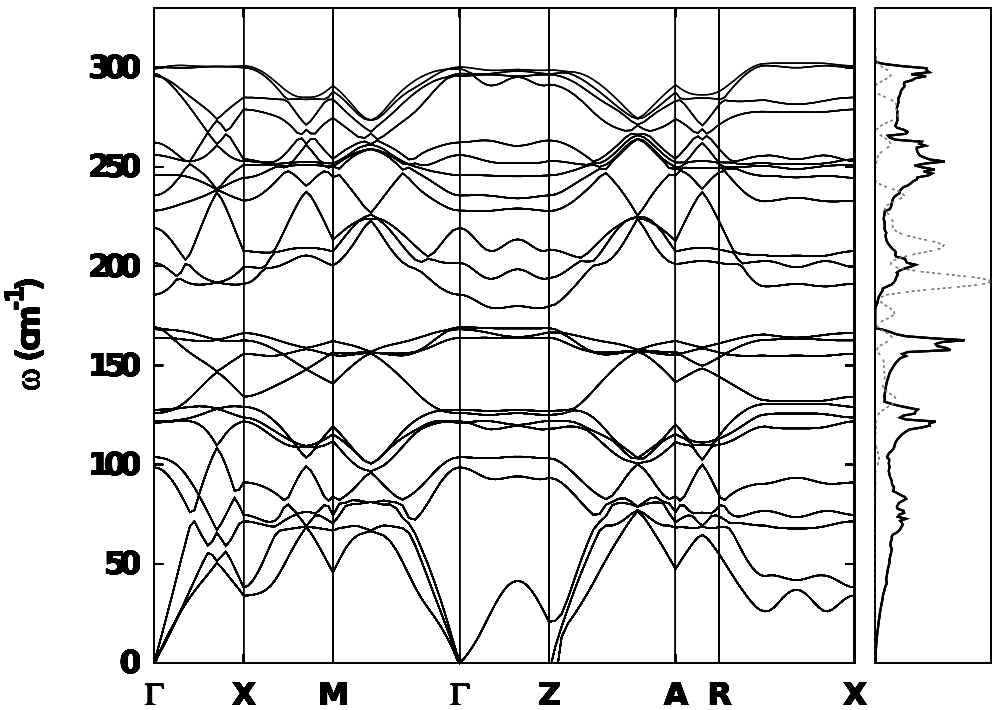

Figure 4.9: Phonon dispersions of FeSe for the striped spin-polarized configuration. Phonon density of states (solid) and Eliashberg spectral function (dashed) are given to the right (in states/cm^{-1}*(1.5) for PDOS, from 0 to 0.3). NOTE: even though the striped spin-configuration has a different BZ, the symmetry points on the wavevector path along the x-axis have the same coordinates when expressed in reciprocal lattice vectors terms as for for the non-magnetic and checkerboard BZ, so the symbols left the same.

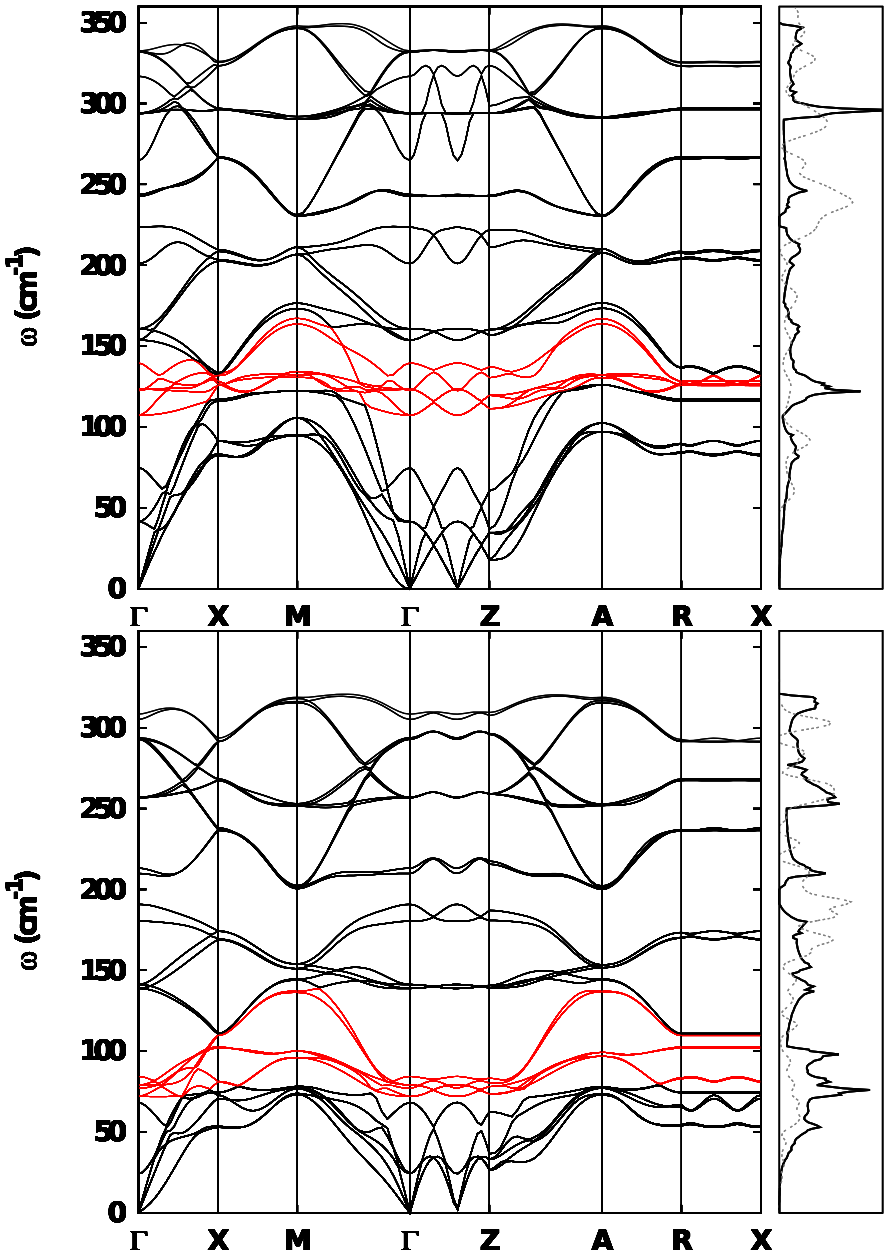

Figure 4.10: Phonon dispersions of KFe_2Se_2 for the non spin-polarized (TOP(a)) and the checkerboard spin-polarized (BOTTOM(b)) configuration. Phonon density of states (solid) and Eliashberg spectral function (dashed) are given to the right (in states/cm^{-1}*(1.5) - non-magnetic, in states/cm^{-1} - spin-resolved, from 0 to 0.5). Bands showing the largest degree of softening are shown in red (brighter) color to guide the eye.

experimentally measured superconducting transition of 8 K for FeSe [48]. The T_c estimates for spin-resolved KFe_2Se_2 are also far away from experimental value of 32 K [118].

4.1.3 Discussion

Currently for both iron-based and copper oxide superconductors there is no consensus regarding the mechanism of electron pairing. In the iron-based compounds, a widely accepted picture is that the itinerant electronic system has a weak but substantial interaction with the significantly localized magnetic moments and charges of the Fe atoms [16, 132–134]. Thus the degree of electronic correlation may be strong enough to be beyond the limits of applicability of the bare local-density (LDA) and generalized-gradient (GGA) approximations. In addition, the fact that no long-range magnetic order is usually seen in these systems experimentally implies that the spin-resolved LDA and GGA may not model the experimental state accurately either [16, 113]. The cases of non-spin resolved and spin-resolved LSDA and GGA calculations can thus be treated as the extremes, and the real experimental situation may be somewhere between the two. Electronic structure properties of iron superconductors are widely believed to be predicted well by LDA without the treatment of spins. This appears to be justified by substantial agreement with experimental results on the Fermi surface shapes at least for 1111 and 122 compounds [16, 133, 135–138]. On the other hand, properties such as equilibrium lattice constants, for example, are better described within the spin-resolved approximation [128]. Therefore in this work we present a detailed comparison of the two approaches considering both electronic and vibrational characteristics. The question about the destruction of magnetic order in the superconducting phase and the presence of the phase separation onto a non-magnetic superconducting phase and magnetic semiconducting phase is still open for KFe_2Se_2 [139]. Also the presence of strong spin fluctuations has been experimentally reported for FeSe [113]. Thus knowing the difference between magnetic and non-magnetic electronic and vibrational properties for both of these compounds is necessary. It would also be interesting to study the effect of non-stoichiometry on electronic and vibrational properties of FeSe compounds, but doing so is rather complicated since the experimental shift in stoichiometry is rather small.

We compare the bandstructures and Fermi surfaces (FS) first. Here and below we refer to the non-spin resolved calculations as LDA and to spin-resolved ones as LSDA for brevity, even though the actual exchange-correlation functionals used are GGA-based. As was mentioned earlier, the 3d states of iron are more localized in energy at the Fermi level for LSDA case. This leads to the differences in

the FS shapes. Since there are no experimental data available for direct comparison for pure FeSe, no conclusion can be made about which method works best. Nevertheless, some features of the LSDA FS can still be expected to be present in experiment. In particular, the fact that FS is better nested could be important. For KFe_2Se_2, experimental findings [126] show no pockets at Γ, which is in agreement with the Fermi surface we find for the spin-resolved case. The fact that our LDA Fermi surface is different from what was obtained in [128] might arise from the necessity to use a relaxed configuration to obtain a dynamically stable structure in this work. In general, we note here that the spin-resolved calculations give better results for equilibrium lattice constants for both compounds (about 1% less then experimental value for FeSe, and 3% less for KFe_2Se_2) and are in agreement with currently available experimental data for the Fermi surfaces. It is also worth mentioning, that if the Fermi level is moved slightly, the Fermi surface shape for FeSe can undergo significant changes because of the high degree of Fe-3d states localization in energy in the spin-resolved case.

To test the importance of the change introduced to the nesting, we calculate the electron-phonon matrix elements averaged over Q_z (z-axis projection of the vector $\vec{Q}$)

$$M = \frac{1}{N_{Q_z}} \sum_{Q_z} M^{[\nu]}_{\vec{k},\vec{k}+\vec{Q}}, \tag{4.1}$$

and then analyze the difference between the spin-resolved squared matrix elements and non-spin-resolved ones

$$\Delta M^2 = M^2_{SP} - M^2_{NS}. \tag{4.2}$$

Colormaps of the differences in checkerboard spin-resolved and non-spin-resolved q_z-averaged matrix elements squared - $\Delta M^2(q_x, q_y)$, are plotted in Fig. 4.11. It can be seen that for FeSe at $|Q(x, y)| = (0.5\ 0.5)$, and for KFe_2Se_2 at $|Q(x, y)| = (0.0\ 0.5)$, the ΔM^2 are significantly amplified for spin-resolved configuration. A closer look at the corresponding Fermi surface shapes confirms that nesting opportunities do increase for those two wavevectors when the spin treatment is included. Thus, we can conclude that nesting does play a significant role in the overall increase of the electron-phonon coupling.

Phonon softening serves as another important factor affecting the electron-phonon coupling. We again emphasize the fact that there are specific phonon modes of A_{1g} symmetry that are affected the most. This means that, when the spin treatment is turned on, the spatial structure of electronic states is affected in such a way that it favors the A_{1g} phonons softening. Visual analysis of the shapes of electronic states at the Fermi level tend to confirm that observation. It is also worthwhile

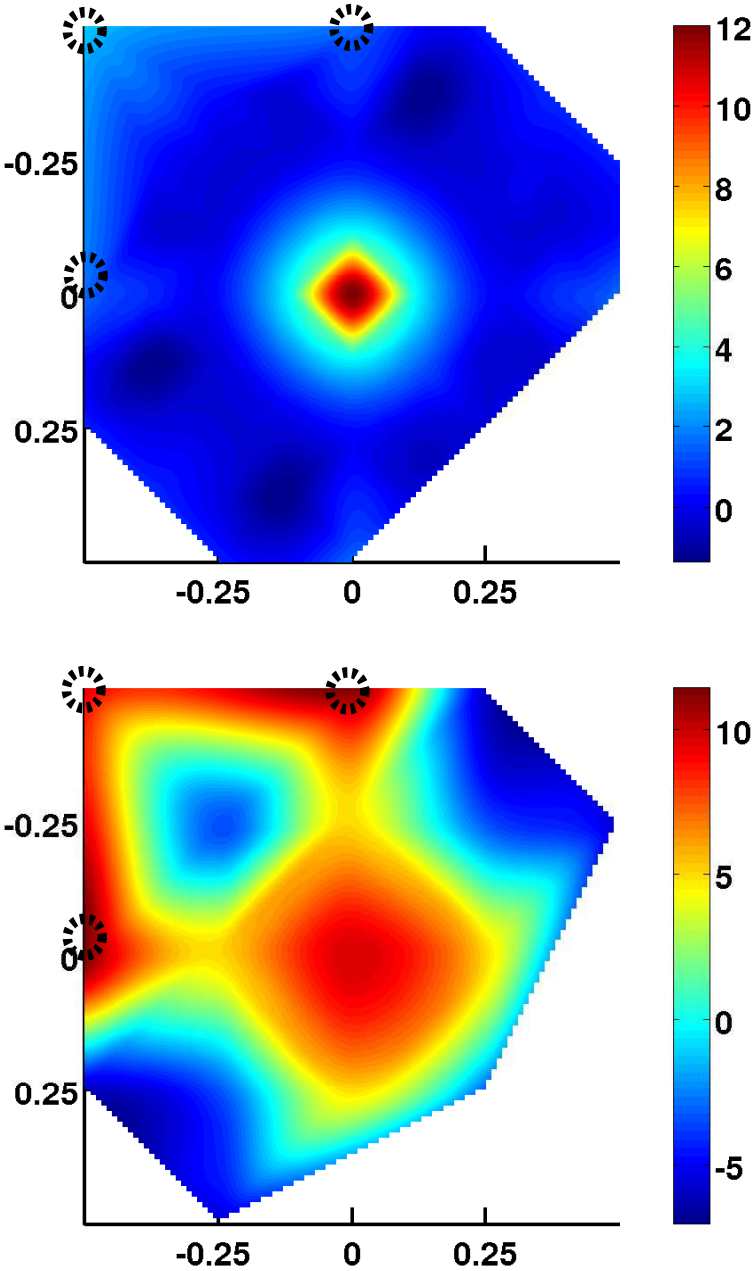

Figure 4.11: Color map of the differences in matrix elements δM^2 between the checkerboard spin resolved and the non-spin-resolved cases (according to (4.2)) given for FeSe (TOP(a)) and KFe_2Se_2 (BOTTOM(b)). The units on x an y-axis are $2\pi/a$, z-axis - arbitrary units. Points (0.0 0.5) and (0.5 0.5) are shown using dashed circles.

Material	$\|\mu\|$	$N(E_F)$	$\omega_l og$	λ	$< M^2 >$	$T_c(\mu^* = 0.1)$
FeSe	-	10.5	250	0.15	0.4	0.0
FeSe(check-brd)	2.2	13.5	280	0.39	0.7	1.1
FeSe(striped)	2.6	6.5	280	0.16	0.4	0.0
KFe_2Se_2	-	16.5	240	0.18	0.9	0.0
KFe_2Se_2(ch)	2.6	18.2	180	0.34	1.1	0.2
KFe_2Se_2(str)	2.8	9.5	-	-	-	-

Table 4.1: Summary of the electronic and electron-phonon interaction related parameters obtained in this work. We show the total coupling strength λ, as well as the Fe magnetic moment $|\mu|$ (in Bohr magnetons), the density of states at the Fermi level $N(E_F)$ (in states/Ry divided by the number of iron atoms in unit cell), the logarithmic average frequency (in K) and the average electron-phonon matrix element squared $< M^2 >$ (arbitrary units). The superconducting transition temperature (T_c, in K) is estimated using the Allen-Dynes formula [26] with a Coulomb parameter μ^* given above.

to notice that for the spin-resolved case, 90% of the total coupling at Γ comes from the A_{1g} mode, whereas the latter is only responsible for 20% for the non-spin-resolved case. This dramatic increase suggests that the phonon perturbation operator also undergoes significant changes in its shape that strongly favor the above mentioned symmetry.

The chalcogen/pnictogen height is an important parameter reflecting the superconducting properties of iron-based compounds, as has been previously noted [133]. The relative behaviors of FeSe and KFe_2Se_2 in our calculations can be analyzed utilizing this picture. For checkerboard LSDA, which gives better agreement with experiment for the structural parameters, the relaxed chalcogen height is 1.41 and 1.38 angstroms for FeSe and KFe_2Se_2 respectively. Since the latter compound has smaller average coupling values and experiments show a rapid increase of T_c with pressure [111, 112], we argue that the optimal chalcogen height could be somewhere within the two values stated above, at least for the electron-phonon interaction based contribution to the pairing mechanism.

To sum up how the results of this work can contribute to the overall understanding of the mechanism of superconductivity in iron-based superconductors, we state the following. There exists a widely accepted belief that the nature of superconducting pairing is not entirely electron-phonon. Our findings confirm this picture. Nevertheless, we show that for the extreme case when static magnetic moments of iron can coexist with superconductivity, the Migdal-Eliashberg theory would predict much higher coupling and transition temperatures closer to the experimental values then were previously found for non-magnetic systems.

4.1.4 Summary

We investigated the electron-phonon interactions in layered FeSe and KFe_2Se_2 from first-principles by considering the effects of inclusion of static magnetic moments of Fe atoms on electronic, vibrational and wavevector-dependent electron-phonon coupling parameter. We find that the 3d-states of iron are localized more in energy space for the spin-resolved case. The latter leads to important changes in the bandstructures and Fermi surfaces. Phonon frequencies and electron-phonon coupling constants are seen to be significantly affected by the changes in electronic structure as well. The shape of the Fermi surface is shown to play an important role. We explain the mechanism by which the electronic structure change induces an enhancement in the electron-phonon coupling and show that it is mainly due to the nesting-related amplification of the electron-phonon matrix elements at specific regions of the BZ.

Our calculation of electron-phonon coupling for spin-resolved configurations in this work provide another way to estimate superconducting transition temperatures. The total electron-phonon coupling values exhibit approximately a to two-fold increase (from 0.15 to 0.39 for FeSe, and from 0.19 to 0.34 for KFe_2Se_2) when a checkerboard spin pattern is introduced. We find spin-resolved coupling values based estimates of T_c to be in better agreement with experiment than estimates for non-spin-resolved configurations, however these are still not large enough to solely explain the superconductivity on the basis of electron-phonon interactions.

4.2 Magnetic excitations in Monolayer FeSe

The electronic structural properties in the presence of constrained magnetization and a charged background are studied for a monolayer of FeSe in non-magnetic, checkerboard-, and striped-antiferromagnetic (AFM) spin configurations. First principles techniques based on the pseudopotential density functional approach and the local spin density approximation are utilized. Our findings show that the experimentally observed shape of the Fermi surface is best described by the checkerboard AFM spin pattern. To explore the underlying pairing mechanism, we study the evolution of the non-magnetic to the AFM-ordered structures under constrained magnetization. We estimate the strength of electronic coupling to magnetic excitations involving an increase in local moment and, separately, a partial moment transfer from one Fe atom to another. We also show that the charge doping in the FeSe can lead to an increase in the density of states at the Fermi level.

4.2.1 Motivation

Recent experimental advances in molecular beam epitaxy and scanning tunneling microscopy have made it possible to study superconducting monolayer systems, such as FeSe, which is the simplest iron-based superconductor. Studies of FeSe monolayer systems on different substrates show significant sensitivity to interface effects and give signs of the presence of superconductivity above 77 K [117, 140]. The latter fact is especially interesting because bulk samples only show superconducting transition temperatures T_c of about 8 K, or 37 K with the application of pressure [48, 111]. When double-layer graphene is used as a substrate, the superconducting gap seems to increase with the FeSe film thickness, and a monolayer-thick film was found to be non-superconducting [117]. At the same time, when FeSe films are studied on $SrTiO_3$, scanning tunneling microscopy reveals the presence of a 20 meV gap for single unit cell thick films, whereas thicker films show no presence of superconductivity [140].

Another difference between the bulk and monolayer FeSe is the Fermi surface topology. ARPES measurements show distinctive shape where only pockets at the Brillouin zone (BZ) boundaries are present, and no pockets are seen at the center point Γ [141]. The same study shows the presence of large and nearly isotropic superconducting gaps without nodes. Another very recent report by the same research group [142] describes the presence of two phases with different Fermi surface topology, where a superconducting phase can be obtained from a non-superconducting one through annealing. Both reports give evidence for

substantial interface-induced changes in electronic structure. Suppression of superconductivity by twin boundaries interconnected with the Se-atom height with respect to the Fe layer was also found [143].

Several theoretical efforts were made to study thin films of FeSe [144, 145]. First-principles study of atomic and electronic structures of one- and two-monolayer thick films on $SrTiO_3$ found semiconductor-like behavior and collinear antiferromagnetic order to be present [144]. No strong hybridization of the electronic states between the substrate and the film was found. Effects of the interaction between the electronic system and soft phonons of $SrTiO_3$ on FeSe/$SrTiO_3$ interface was studied using functional renormalization group calculations [145]. The possibility for the soft phonons at the interface to significantly affect the pairing mechanism and increase T_c with respect to the bulk sample was proposed.

In the current work we study the electronic structure of an isolated FeSe monolayer in the non-spin-resolved (NM) phase, and for the checkerboard (CH) and the striped (STR) antiferromagnetic (AFM) spin configurations. We utilize a first principle pseudopotential density functional theory and local spin density approximation (LSDA) based approach. Our results show that the shape of the Fermi surface for the doped CH AFM spin configuration is consistent with the experimentally observed one. We study the evolution of the electronic structure from the NM to the AFM cases under magnetization constraints on Fe-atoms. Constrained magnetization-based estimates show that the transfer of magnetic moment between Fe atoms induces a larger bandstructure shift than the case when magnetic moments are increased. The strength of the magnon-induced energy shifts is up to one order of magnitude larger then a typical value for an energy shift caused by phonons. We also study the effect of the introduction of a charge background, and find that it can significantly change the density of electronic states at the Fermi level.

4.2.2 Results

First, we consider the differences in electronic structure between the bulk and monolayer cases. As can be seen from Fig. 4.12(a), the NM Fermi surface for FeSe is very similar to that of the bulk crystal [127]. There are three hole pockets at the zone center Γ and two electron pockets centered at the corners. Fig. 4.12(c) shows the Fermi surface for the STR AFM case, that is similar to the bulk case (for bulk FeSe electronic structure see [146], for example). There are two pockets that form the Fermi surface: the hole-pocket is centered at Γ, and the electron-pocket forms satellites located nearby Γ towards the Y direction. The BZ for the STR case is a fraction of those for NM and CH, so we note that the pocket at Γ for the STR configuration's reduced BZ would produce pockets at both Γ and M for

the other two configuration's. The CH case does exhibit a different Fermi surface in the monolayer configuration. Fig. 4.12(b) shows only one electronic pocket at M and small hole-like pockets around Γ towards X. The bandstructure analysis shows that this difference comes mainly from the change in the shape of a "flat" band formed close to the Fermi level E_F, below it. In contrast to the bulk case, this band shows a significant reduction in energy width. Analysis of the spatially resolved integrated local density of states in the region of 200 meV below the Fermi level clearly shows the concentration of charge on iron atoms due to the formation of the above-mentioned "flat" band.

Secondly, since the experimentally observed value of the Fe magnetic moment for the iron-based superconductors is usually smaller then the first-principle calculations-based theoretical predictions [16, 133], we introduce constraints on the value of the atomic magnetization to effectively lower the resulting local moment. We then study how the electronic structure evolves from the non-magnetic to spin-ordered case. Fig. 4.13 shows the resulting evolution for the CH AFM case. It can be seen that when we introduce magnetization, the energy states split around M, and as the magnetization increases, a "flat" band starts forming as a composition of the bands both initially present in non-magnetic states around the Fermi level and the lower-lying ones. Similar behavior is seen at the Γ point: a state initially at about -0.5 eV below the Fermi level rises to form the flat band, and the hole-like bands lower their positions in energy until they fall below E_F. As a result, a sharp peak in the density of states is formed right below the Fermi level. Overall, the bandstructure undergoes significant changes including both band rearrangements and shifts. We point out here that a similar-looking electronic structure transformation is observed in experiment [142] via annealing.

Since one of the possible effects of the interface could be a charge exchange, it is interesting to analyze how the electronic structure is affected by doping. To do this, we introduce a uniform jellium charge background. Fig. 4.14 shows the results for the CH AFM case (with 2.28 μ_B and no constraints), where two particularly interesting things can be noted: first, the width of the "flat" band formed below E_F is very sensitive to positive doping, and hole-like states appear at the Fermi level at various point of the BZ; secondly, an electron-like state falls below the Fermi level at Γ point for negative doping, forming a second electron-like pocket of the Fermi surface. The latter configuration has a Fermi surface that is similar to what was obtained for a bulk intercalated FeSe-compound in [147]. The density of states plots given in Fig. 4.14 exhibit a shape, that favors an increase at E_F for both positive and negative doping. In the former case the increase is induced by moving the Fermi level into the flat-band-originated peak, in the latter case the increase is due to the appearance of the above-mentioned electron-like band at Γ. For the NM and the STR phases our calculations show

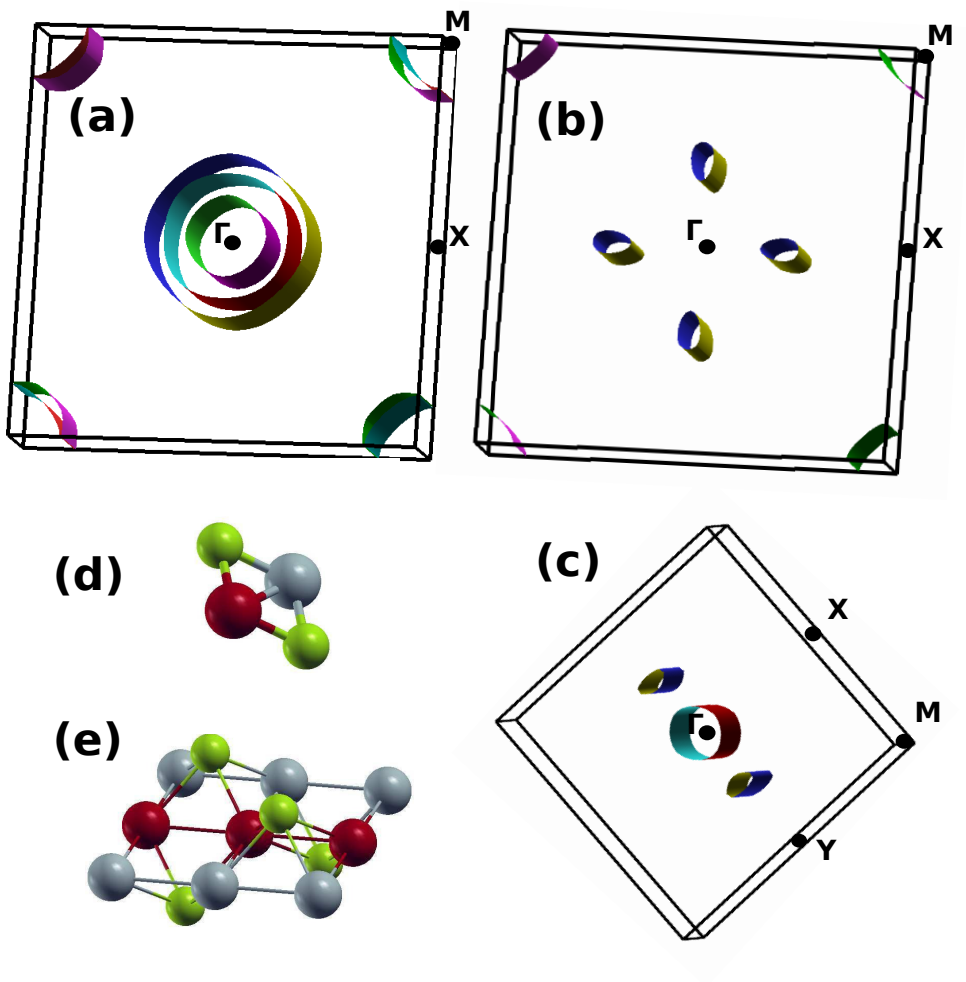

Figure 4.12: (a)-(c) Fermi surfaces of an FeSe monolayer for the non-spin-polarized, checkerboard AFM and striped AFM cases respectively. The non-zero length in z-direction is due to the finite size of the unit cell. NOTE: the striped spin-configuration has a different BZ (rotated by $\pi/2$ and scaled by $\sqrt{2}$ in k_x and k_y-directions). The stripe direction is toward the given X point. (d) - the unit cell with two Fe and two Se atoms, used in our calculations for non-magnetic and checkerboard cases. (e) - the unit cell for the striped iron spin arrangements; the neighboring atoms are also shown. The Fe atoms are red and grey for spin up and down, and Se atoms are shown in green (above and below the Fe-plane).

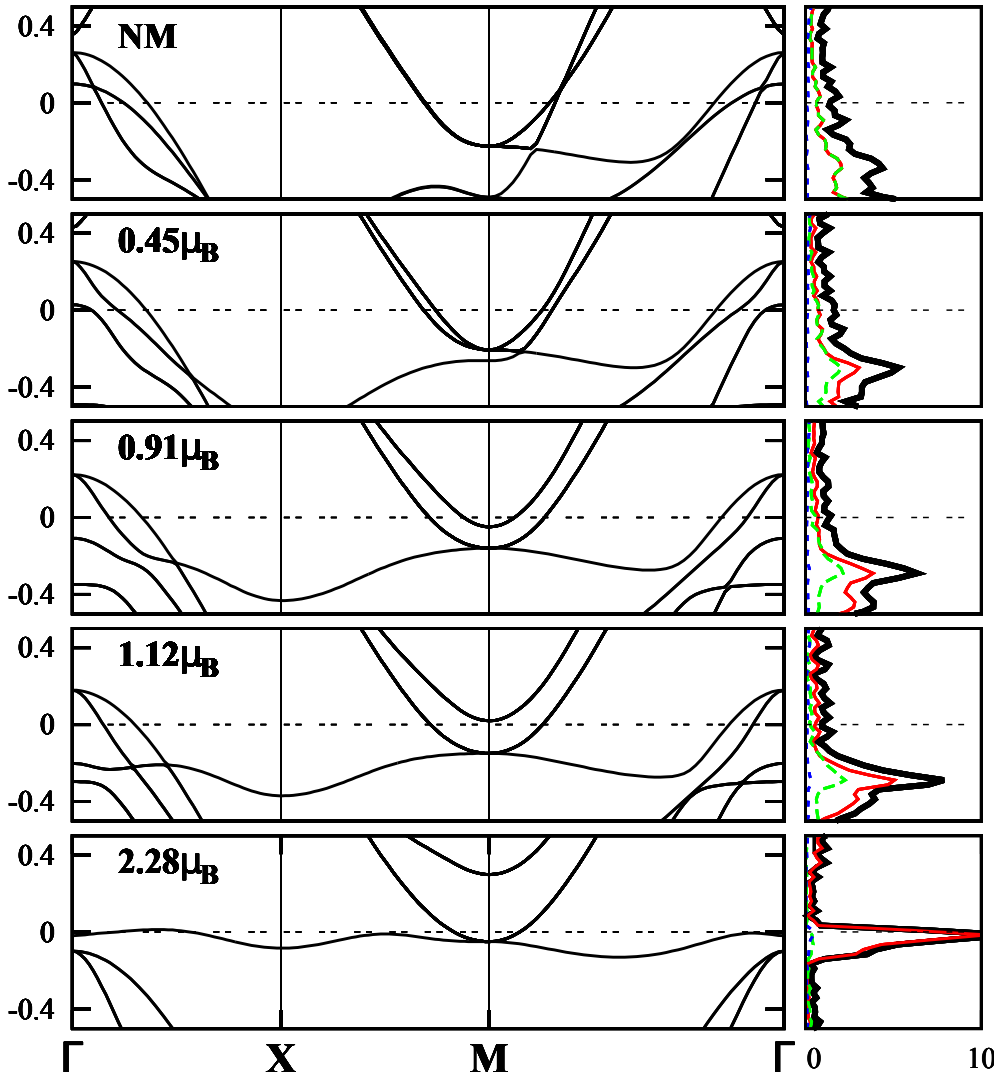

Figure 4.13: The evolution of the electronic bandstructure of an FeSe monolayer under constrained magnetization for the checkerboard antiferromagnetic spin-polarized case. From top to bottom the resulting value of the magnetic moment on iron atoms is changing from zero (NM - non-magnetic) to 2.28 μ_B. The units on y-axis are electron-volts, and the Fermi level is at zero. To the right the corresponding projected densities of states (in states/eV) are plotted for all atoms (black solid), Fe-3d-up states (red solid), Fe-3d-down states (green dashed) and Se (blue dot-dashed).

a rigid band shift of E_F for the positive charge doping. The hole-like bands at Γ exhibit higher sensitivity in their relative position with respect to the Fermi level, shifting upward in energy. For the negative charge doping we see new electron-like states appear at the Fermi level around Γ for -0.25e in the non-magnetic case, and for -0.75e doping in the striped case. The density of states at the Fermi level shows a relative increase for both doping directions in both NM and STR phases.

4.2.3 Discussion

There appears to be a general belief that the non-spin-resolved structure studies using the local-density approximation provide Fermi surface shapes that are in agreement with experiment at least for 1111 and 122 compounds [16, 133]. Nevertheless, some properties, such as equilibrium lattice constants, for example, are better described within LSDA [128, 148]. On the basis of our findings we suggest here that a specific AFM spin orientation might be induced in the FeSe layer by the substrate. There have been previous studies that reported that $SrTiO_3$ substrate can induce AFM order at the interface in thin films [149, 150]. The existence of only one M-point centered Fermi surface pocket was addressed with respect to the superconducting pairing in [151] and might also mean that the currently widely accepted $s_\pm$ model [18, 129] needs to be adjusted. The presence of the small pockets in our calculation for zero doping should not mislead the reader, since the behavior of the electronic structure with doping (as seen in Fig. 4.13) shows that a small excess of negative charge shifts the Fermi level above the hole-like band and the pockets will disappear from the Fermi surface. In Ref. [142] it is explicitly mentioned that annealing does introduce charge doping. On the basis of our model we argue that the doping is negative.

We compare our results to the results of Ref. [144], where similar first-principle studies were made for a monolayer and bilayer FeSe films on $SrTiO_3$ substrate. First, since the presence of antiferromagnetic order and no strong hybridization between substrate and film electronic states were found in [144], we focus our studies on the FeSe monolayer without explicitly treating a substrate. Secondly, in this work we plot the Fermi surfaces for the FeSe monolayer in different spin configurations and compare them with the experimental findings of [141], which has not been done before. Finally, we use the jellium approximation to study substrate-induced doping in the current paper, which is a rather simple, but nevertheless physically reasonable and well-established approximation. To sum it up, we believe that the results of the current work and Ref. [144] should be treated as complimentary to each other. We also have modeled the effects of strain on

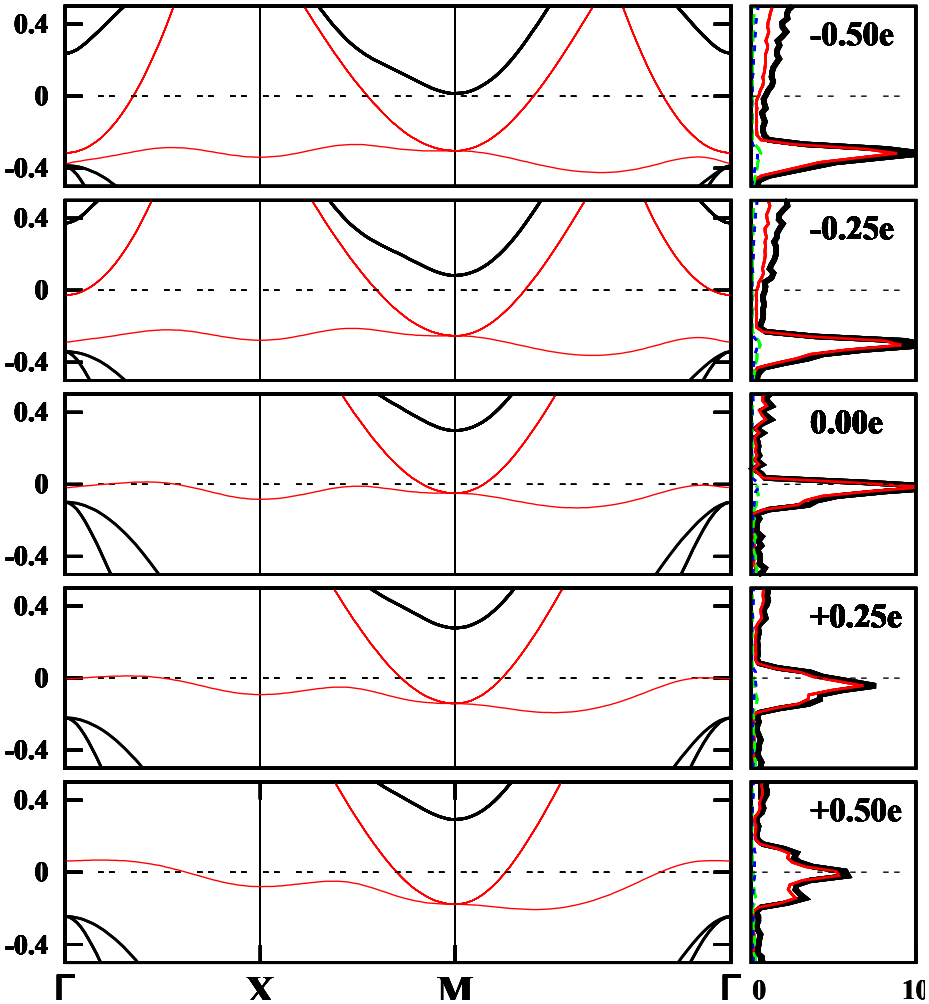

Figure 4.14: The electronic bandstructures of the FeSe monolayer with different levels of charge doping in the checkerboard antiferromagnetic spin-polarized case (with 2.28 μ_B and no constraints). From top to bottom the value of excessive background charge is changing from -0.5e to +0.5e, as shown. The units on the y-axis are electron-volts, and the Fermi level is at zero. To the right the corresponding projected densities of states (in states/eV) are plotted for all atoms (black solid), Fe-3d-up states (red solid), Fe-3d-down states (green dashed) and Se (blue dot-dashed). Red-colored (brighter-colored) bands are the ones crossing the Fermi level.

the electronic structure of the monolayer by varying the lattice constant within 5% from the equilibrium values and did not find any significant differences.

To explore the possible pairing mechanisms, we have studied the bandstructure evolution with magnetization constraints, and analyze the bandshifts introduced by particular magnetic excitations. This approach is analogous to a frozen phonon approach to evaluate electron-phonon coupling. For example, from Fig. 4.13 we extract the information for the relative position of the bottom of the electron-like band at M with respect to E_F as a function of the Fe magnetic moment. In the unfolded non-magnetic BZ of iron lattice only (similar to used in [151]) the introduction of the CH spin orientation corresponds to the magnon q-vector of (π,π). Similarly for the evolution of the NM to the STR configuration we analyze the relative position of the hole-like band maxima at Γ. This excitation corresponds to a (π, 0) magnon in the unfolded BZ. Both (π,π) and (π, 0) magnons involve an increase of local Fe moments in a corresponding spin arrangements with respect to the non-magnetic configuration. We also apply a small-magnitude magnetization shift from (μ_0, $-\mu_0$) to ($\mu_0 + \delta\mu$, $-\mu_0 + \delta\mu$), corresponding to an effective transfer of local moment between the Fe atoms. Our analysis shows that the energy shifts for all three cases do not strongly depend on the value of the iron-magnetic moment. The relative strengths of the shifts are estimated as follows:

$$(\frac{\partial E_M}{\partial \mu})_{(\pi,\pi)} : (\frac{\partial E_\Gamma}{\partial \mu})_{(\pi,0)} : (\frac{\partial E}{\partial \mu})_{(trans)} = 1 : 1.5 : 6 \tag{4.3}$$

In addition, we analyze the $(\partial\mu/\partial a)$ derivative, where a is the in-plane lattice constant, to calculate $(\partial E/\partial a)_{mag} = (\partial E/\partial\mu)(\partial\mu/\partial a)$. To accomplish this we obtain the relaxed structures for each magnetization value considered. The estimates give $(\partial E/\partial V)_{(\pi,\pi)} \approx 1$ eV/$\AA$, which is of the same order as a characteristic value for a frozen phonon, if we consider $(\partial E)_{ph} \approx 15$ meV, $a \approx 3.75\AA$, which are typical for FeSe, and a $(\partial a/a)_{ph} \approx 0.005$. So we can conclude that the local moment transfer-involving magnetic excitation are coupled to electronic states stronger than the excitations that involve magnetization increase only. The relative coupling value for the latter is of the same order as for the phonons.

As seen in the current work, the increase in the superconducting gap value and T_c for the monolayer FeSe and intercalated FeSe compounds, for example, may originate from the charge-transfer-induced increase in the density of states at the Fermi level for the FeSe-layer, and the charge transfer itself can originate from the interaction with the $SrTiO_3$ substrate, or from chemical doping in the case of alkali doped FeSe materials. Such an increase would mean that there are more electronic states that can take part in the scattering process forming Cooper pairs, thus increasing the gap between the superconducting and normal states. For the checkerboard AFM configuration of FeSe monolayer (and for

the other two configurations as well) a positive charge doping produces a large increase in the density of states, but also introduces hole pockets to the Fermi surface, which are not seen experimentally. Negative doping induces less change in the density of states (this is true for the striped AFM state as well), but seems to be more consistent with the shape of the Fermi surface seen by ARPES measurements. Controlling the charge carriers density in thin films by gating has long been an actively researched field for graphene. The results here suggest that similar approaches can be beneficial for studying superconductivity in FeSe and possibly in other iron-based superconductors. Our results also suggest that the superconducting gap in an FeSe monolayer can be enhanced with gating.

4.2.4 Summary

In conclusion, we have studied the electronic properties of an FeSe monolayer in different spin configurations. Our results show that the checkerboard antiferromagnetic spin pattern yields a Fermi surface that resembles the experimental results for FeSe on $STiO_3$. This suggests that a similar antiferromagnetic spin pattern is induced in the monolayer under experimental conditions. A study of the evolution of the non-magnetic electronic structure into the checkerboard and the striped antiferromagnetic configurations under constrained magnetization reveals that the magnetic excitations involving local moment transfer are coupled to electronic states stronger then the ones involving an equal change in magnetization. By simulating the substrate-induced interface effects we show that the presence of a uniform positive background charge in the FeSe-layer can lead to an increase in the density of states at the Fermi level. Our findings propose that gated devices similar to the ones used now for graphene may be able to reveal new interesting results in FeSe and other two-dimensional superconductors.

4.3 Spin-fluctuations-induced electron-electron interaction in FeSe

We analyze the spin-fluctuations-induced interaction in FeSe using a first-principles approach based on pseudopotential density functional theory and local density approximation. We find the gross isotropic average of the interaction throughout the Fermi surface to increase when selenium atom height is decreased. We also find the anisotropic interaction to have structure consistent with the $s\pm$ symmetry.

4.3.1 Motivation

There exist many attempts to understand unconventional high-temperature superconductivity on the basis of spin fluctuations [152–155]. Cuprates [152–154] and recently iron pnictide and chalcogenide materials [17, 156, 157] can be listed among the study cases. The effect of spin fluctuations on electronic states is often calculated utilizing model Hamiltonian approach. Pioneering works were based on the homogeneous electron gas and tight-binding approximation [158–160]. Recent studies, aimed to investigate superconductivity in the cuprates and pnictides, used experimental neutron scattering and nuclear magnetic resonance data to parametrize the spin susceptibility [152, 154, 161]. Alternatively, other works combined first-principles techniques with fitting the interaction parameters to reproduce experimental findings [156, 157].

The results of model Hamiltonian-based approaches further justified the need for a fully first-principles approach. Several attempts to implement one were made. Spin susceptibility and the electron self energy were evaluated on the basis of the density-functional theory (DFT) for palladium and vanadium [162, 163]. The T-matrix approach was employed to calculate satellites in the photoemission spectrum and quasiparticle lifetimes in nickel and other metals [164–166]. Recently, the interacting spin susceptibility was calculated for iron selenide for various Se height values [167]. Another study discussed Fermi surface nesting and the static susceptibility of FeSe under pressure and found indirect evidence for strong coupling [168].

In this work, we analyze the interaction between the electronic states arising from spin fluctuations solely on the basis of the pseudopotential density functional theory. We apply our approach to study bulk FeSe. An isotropic average of the interaction for the states on the Fermi surface is found to be sensitive to the selenium atom height inside the unit cell. About a two-fold increase in the isotropic average is seen when the selenium height is decreased to 40% of it's

experimental value. We associate the increase with the changes in the electronic structure at the Fermi level. In addition, we confirm that the spatial shape of the anisotropic interaction is consistent with the $s\pm$ symmetry.

4.3.2 Results and Discussion

4.3.2.1 Electronic structure

The electronic bandstructures and the corresponding densities of states of FeSe for three different values of selenium heights z_{Se} are shown in Fig. 4.15. The bandstructure undergoes significant changes when z_{Se} is changed. For the experimental value of 0.25 there are four bands crossing the Fermi level: two hole-like bands at Γ and two electron-like bands at M. This is consistent with previous calculations [127, 146]. For z_{Se}=0.20 the hole-like Fermi surface shrinks in size and one of the hole bands falls below the Fermi level, and the effective masses of the electron bands decreases. For z_{Se}=0.15 the bandstructure looks rather different with both electron- and hole-like states at the center of the Brillouin zone.

The total density of states increases with the application of pressure (decrease in z_{Se} from 0.25 to 0.20) as the top of the hole-like band crosses the Fermi level E_F. A further decrease of z_{Se} changes the value of the density of states at E_F to be slightly lower (see Table 4.2).

4.3.2.2 Spin susceptibility

The non-interacting spin susceptibility plots are presented in Fig. 4.16. For z_{Se}=0.25 there are peaks at M (0.5 0.5 0.0) and at X (0.5 0.0 0.0), which is consistent with the previous findings [167, 168]. When z_{Se} is decreased, spectral weight at the zone center around Γ starts to increase as the hole-like band crosses the Fermi level for z_{Se}=0.2. This leads to an overall increase in χ_0 everywhere in the zone. A further decrease in z_{Se} leads to a rearrangement of spectral weight so that χ_0 peaks at Γ and the [110] direction is amplified. This change reflects the fact that a state with electron-like dispersion is at E_F for z_{Se}=0.15.

4.3.2.3 Isotropic average of the scattering matrix element

An isotropic average of the matrix element for scattering from Eq. 2.35 over the Fermi surface $V(q) = 1/N_{\mathbf{k}} \sum_{\mathbf{q}} V(\mathbf{k}, \mathbf{k}+\mathbf{q})$ is shown in the right panel of Fig. 4.16. For z_{Se}=0.25, $V(q)$ peaks for $|\mathbf{q}| \approx 0.25$. The spectral weight around

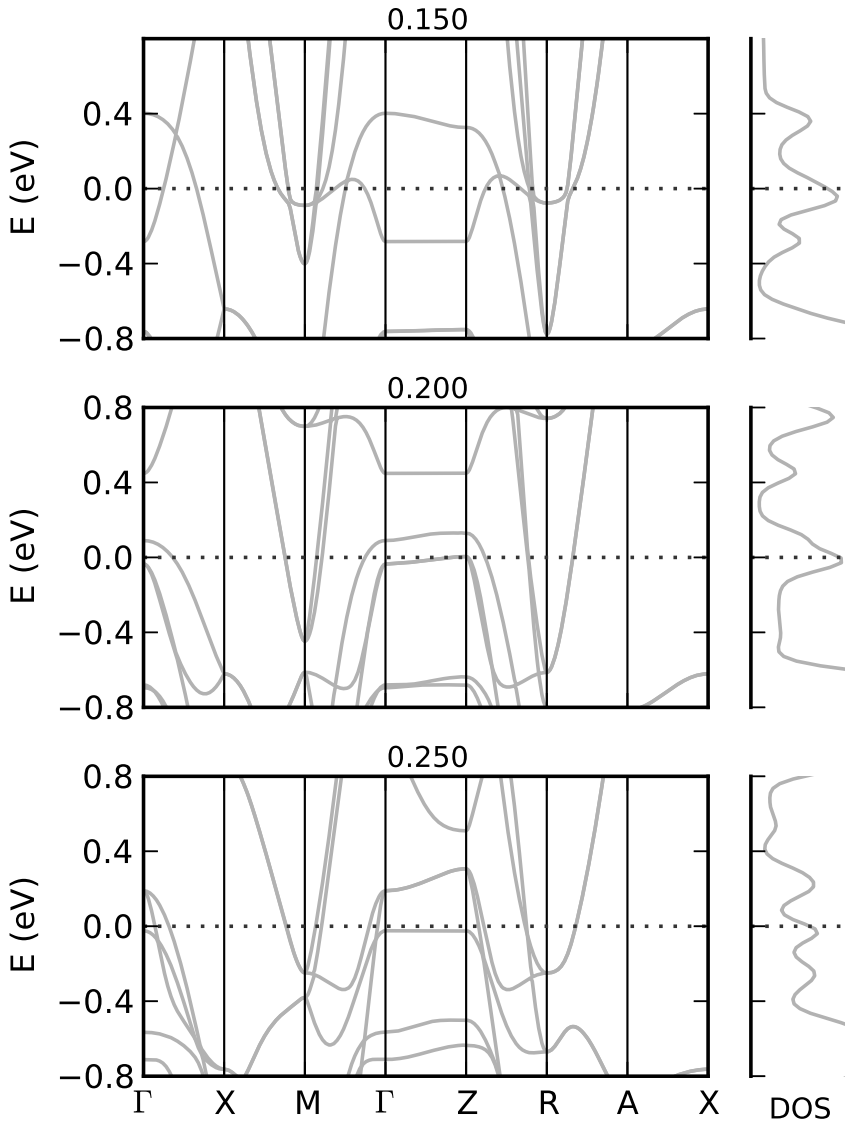

Figure 4.15: Electronic bandstructures of FeSe for different values of Se atom height z_{Se}: 0.25, 0.20 and 0.15 as measured in units of the lattice parameter c. On the right panel the corresponding total densities of states are plotted.

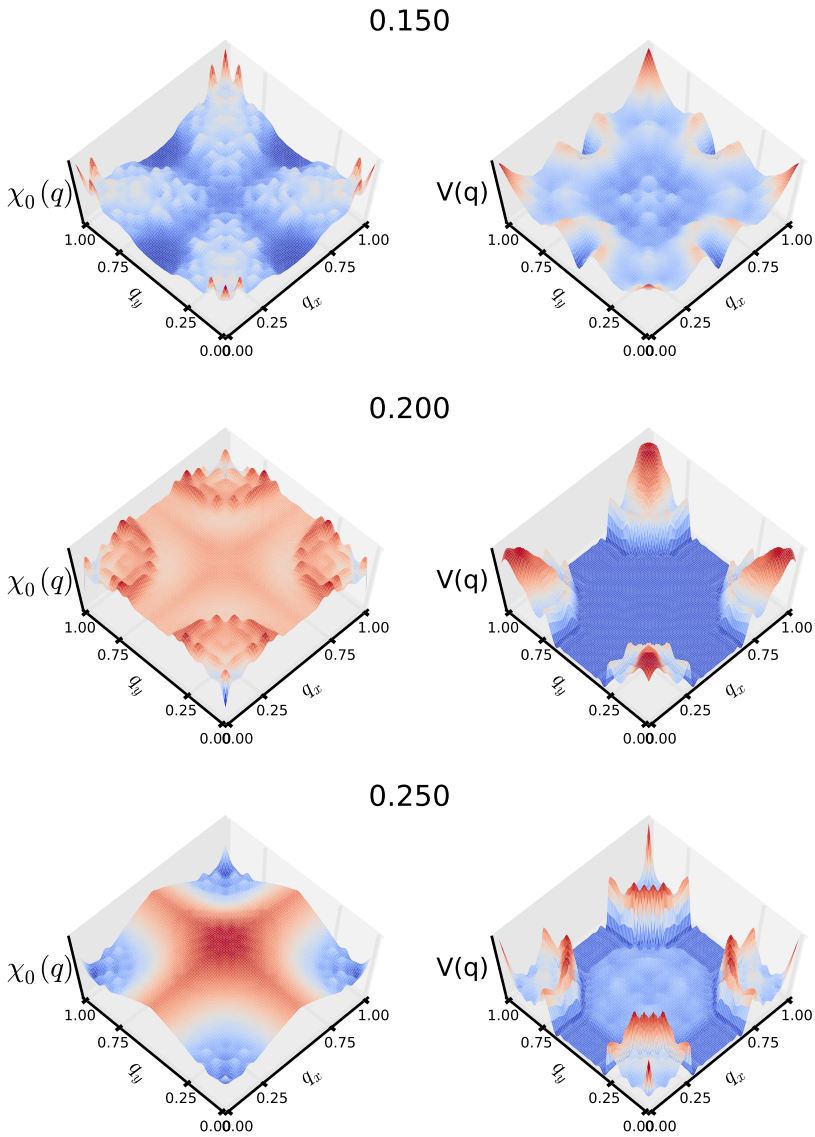

Figure 4.16: The non-interacting spin susceptibility χ_0 (on the left) and the isotropic average of the spin-fluctuations induced interaction $V(q) = 1/N_{\mathbf{k}} \sum_{\mathbf{q}} V(\mathbf{k}, \mathbf{k}+\mathbf{q})$ for q_z=0. Results for three different values of selenium heights z_{Se}=0.25, 0.20 and 0.15 are given. The surfaces are colored such that red areas correspond to larger values and blue - to smaller values. Brillouin zone center Γ is at (0,0). q_x and q_y are given in units of $2\pi/a$. The units on z-axis are arbitrary. High symmetry points M and X are at (0.5 0.5) and (0.5 0.0) respectively (and the points related by symmetry).

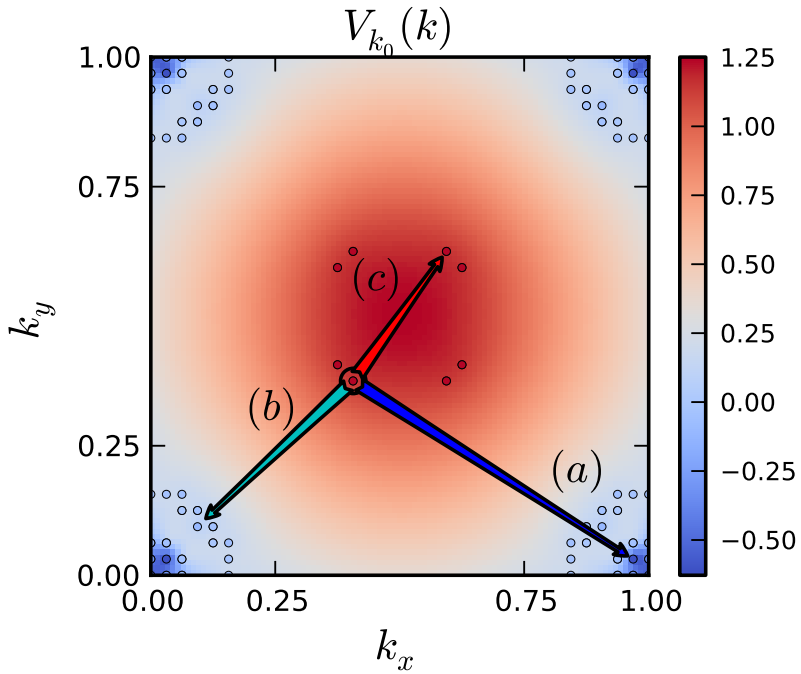

Figure 4.17: Colormap of the anisotropic interaction $V(\mathbf{k_0}, \mathbf{k}')$ for $\mathbf{k_0}$=(0.4 0.4 0.0) and z_{Se}=0.25. k_z is equal to 0. Arrows (a), (b) and (c) denote the corresponding scattering events from $\mathbf{k_0}$ to a hole-like bands close to Γ (0.0 0.0) - (a) and (b), and to electron-like band around M (0.5 0.5) - (c). The color represents the magnitude of $V(\mathbf{k_0}, \mathbf{k}')$ in arbitrary units.

Table 4.2: Summary of the parameters calculated in this work. Shown below are: the density of states at the Fermi level $N(0)$ (in atomic units, per unit cell, per spin), the spin-fluctuations-induced pairing interaction averaged over the Brillouin zone V, and their product $N(0)V$.

z_{Se} (in units of **c**)	$N(0)$ (a.u.)	V (arb. units)	$N(0)V$ (arb. units)
0.150	0.175	1.02	0.18
0.200	0.194	0.79	0.15
0.250	0.138	0.50	0.07

$\mathbf{q} = 0$ is relatively small. Under pressure (z_{Se}=0.20) spectral weight for zero $\mathbf{q}$ increases and a peak at Γ is formed. It is natural to associate this increase, again, with the holelike band crossing the Fermi level. The shape of $V(q)$ becomes more anisotropic for the smallest selenuim height (0.15); peaks are formed at around (0.4 0.0 0.0) and (0.5 0.1 0.0) and at the points related by crystal symmetry. Some increase at the zone center is also seen.

4.3.2.4 Interaction strength

Based on the above results we analyze how the isotropic average of the electronic interaction via spin-fluctuations changes with z_{Se}. For this we track changes in $N(0)V$ - the product of the density of states at the Fermi level and the isotropic average of $V(q)$. Results can be seen in Table 4.2. The density of states at E_F has maximum for z_{Se}=0.20, and V monotonically grows as the selenium height is decreased. The product of the two experience a 2.5 times increase when z_{Se} is varied from 0.25 to 0.15.

4.3.2.5 Anisotropic interaction

Finally we present the anisotropic interaction $V(\mathbf{k_0}, \mathbf{k}')$ for $\mathbf{k_0}$=(0.4 0.4 0.0) and z_{Se}=0.25 in Fig. 4.17. It is clearly seen that the matrix elements for scattering changes sign depending of whether the scattering occurs within the electron-like band or from electron-like to hole-like band. This is consistent with the $s\pm$ model for pairing [17]. The absolute value of scattering matrix element $V(\mathbf{k_0}, \mathbf{k}')$ is about two times larger for electron-electron scattering than for electron-hole channel.

4.3.3 Summary

In conclusion, we have calculated the fully anisotropic spin-fluctuations-induced interaction for FeSe from first principles for different values of the atomic height of Se within the calculation cell. We found that an isotropic average value of the interaction is sensitive to selenium height. There is an increase of about two-fold when selenium height is decreased from 0.25 to 0.15. We associate this increase with the changes in the electronic structure at the Fermi level. We confirm that the shape of the anisotropic interaction in reciprocal space is consistent with the $s\pm$ symmetry.

Chapter 5

Complex oxides

Superconductivity in complex oxides is discussed next in this chapter. The superconducting pairing in these materials is largely believed to be induced by electron-phonon interactions. Nevertheless, at the time of this writing no theoretical description based on the electron-phonon mechanism is consistent with all the experimental results. To further test this, we use precise first-principle techniques as described in chapter 2 to calculate the electron-phonon coupling in K-doped $BaBiO_3$. We examine many of the possible structural distortions in this compound and calculate the superconducting transition temperature. More details are given is Ref. [169].

5.1 K-intercalated $BaBiO_3$

Despite considerable research efforts, a clear understanding of superconductivity in $Ba_{0.5}K_{0.5}BiO_3$ has been elusive. Recent studies showed that although electron-correlation effects in this compound can significantly increase the electron-phonon coupling, they do not reproduce the measured Eliashberg spectral function (α^2F). We show that the oxygen octahedra tilts in $Ba_{0.5}K_{0.5}BiO_3$ increase α^2F in the range of frequencies near 30 meV, even on the level of the generalized gradient approximation. This increase in α^2F changes its spectral shape and provides a better agreement with experiment. This effect results in a 50-60% increase of the average electron-phonon coupling strength λ. We use the Wannier interpolation technique to determine the electron-phonon coupling with high precision.

5.1.1 Motivation

More than two decades ago it was found [170, 171] that the superconducting transition temperature T_c of $Ba_{1-x}K_xBiO_3$ was close to 30 K (for x=0.4), one of the highest among materials without copper or iron. Unlike copper and iron-based superconductors, $Ba_{1-x}K_xBiO_3$ is non-magnetic [171, 172], and its electrons are likely paired by a more conventional electron-phonon coupling mechanism. A large value of electron-phonon coupling parameter λ (about 1.0–1.2) was confirmed by the tunneling measurements [173, 174], as well as by specific heat experiments [175]. It has been suggested that this large electron-phonon coupling originates from the proximity of a charge-density-wave phase [176–181] in the parent compound ($BaBiO_3$) and the accompanied Bi–O breathing structural distortion [182].

There are several theoretical attempt to study of the origin of superconductivity in $Ba_{1-x}K_xBiO_3$. An early study of the Bi–O breathing mode on the basis of the frozen-phonon approximation estimated λ to be about 0.3 based on this mode [183], much smaller than the experimental value (1.0–1.2). A more detailed calculation, using the virtual crystal approximation (VCA) and including all phonon branches sampled over the Brillouin zone, gave nearly the same value of $\lambda = 0.3$ [184]. Even the inclusion of anharmonic effects did not account for the discrepancy between theory and experiment. The additional anharmonic contribution [184] to λ is estimated to be 0.04. Earlier study [185] estimated anharmonic λ to be equal to 0.2.

To account for the differences between experiment and theory, recent studies [186, 187] emphasized shortcomings of the local-density approximation (LDA) to describe electron correlation. A study based on the GW approximation and hybrid functionals in Ref. [187] found the shift of the electronic bands due to a

Bi–O breathing mode to be $\sim \sqrt{3}$ times larger than for LDA. The authors then performed ad hoc rescaling of the Brillouin zone average LDA electron-phonon coupling parameter, obtained in VCA case, ($\lambda \approx 0.3$) by a factor of $\sim$3 which yielded $\lambda = 1$.

Approaching from a different perspective, we found in the current work that a careful treatment of structural distortions increases the spectral weight in the low- and mid- frequency zone of the Eliashberg spectral function α^2F. This increase leads to a better correspondence between theory and experiment and does not require an ad hoc rescaling. A sketch of how the hybrid functional approach from Ref. [187] and the structural distortions considered in this work adjust the VCA result for α^2F is given in Figure 5.1. In this study we have not attempted to use the hybrid functionals approach as it would make an extensive study of phonon and electron-phonon coupling properties not feasible computationally within our model which includes the structural distortions and doping explicitly.

We show here that the presence of oxygen octahedra tilts [188] in $Ba_{0.5}K_{0.5}BiO_3$ increases λ from 0.3 to 0.45, even on the level of a conventional generalized gradient approximation. We also explicitly include dopant atoms (K) in our calculation, without relying on the virtual crystal approximation. In addition, we use the Wannier interpolation techniques [27] to integrate the electron-phonon coupling on a very fine mesh in the Brillouin zone (mesh size is up to 30×30×30).

5.1.2 Results

5.1.2.1 Atomic structure

In this work we use the fully relaxed structure of $Ba_{0.5}K_{0.5}BiO_3$ in the enlarged primitive unit cell containing 20 atoms ($\sqrt{2}\times\sqrt{2}\times2$ reconstruction of the primitive cubic 5 atom cell). In addition, we explicitly take into account dopant atoms (K) and do not rely on the virtual crystal approximation. We consider all three possible arrangements of the dopant atoms (K) in the 20 atom primitive unit cell of $Ba_{0.5}K_{0.5}BiO_3$. These configurations, labeled I, II, III, consist of alternating planes of K and Ba atoms along [111], [110] and [001] directions respectively (see Fig. 5.2). The three doping arrangements are within 50 meV (per formula unit) from each other in energy with total energies decreasing from I to III.

For an easier comparison with previous theoretical work, we also treat $Ba_{0.5}K_{0.5}BiO_3$ using the virtual crystal approximation (VCA), in a simple-cubic 5-atom unit cell. In addition, we fully relax the structure of the parent compound ($BaBiO_3$) in the same enlarged unit cell ($\sqrt{2} \times \sqrt{2} \times 2$) as for the doped compound.

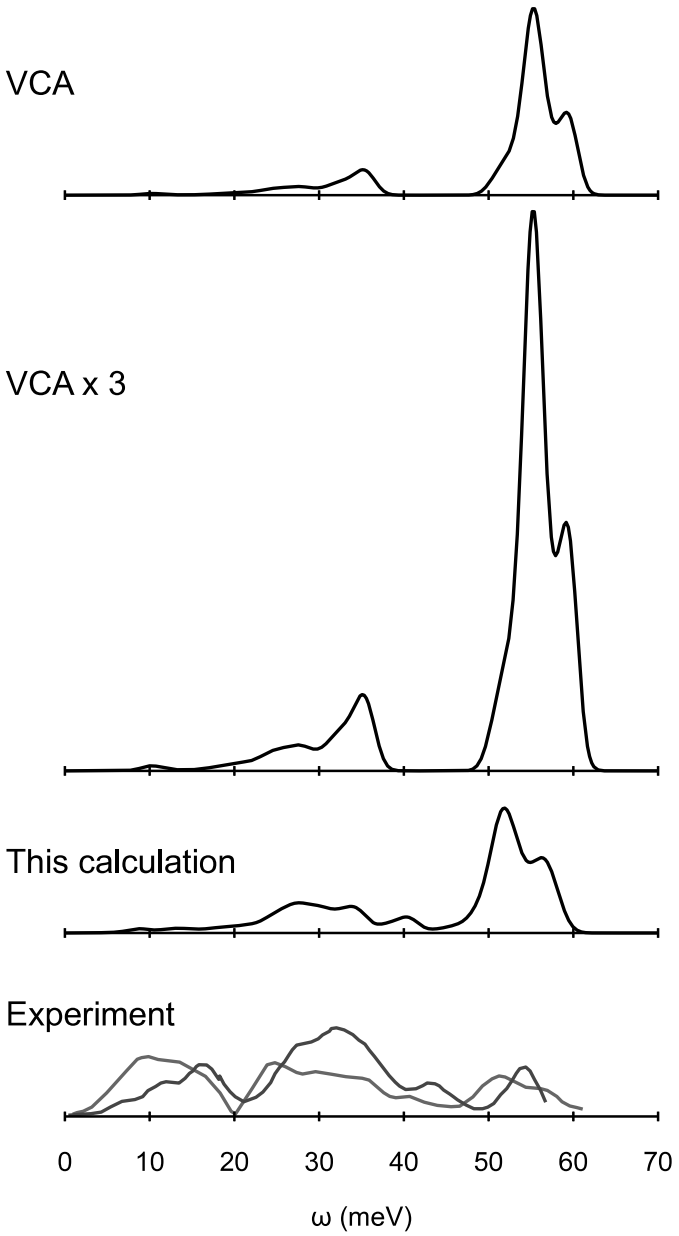

Figure 5.1: A comparison of the available results for the Eliashberg spectral function $\alpha^2F(\omega)$. Results for the virtual crystal approximation (VCA) and the supercell approach of this work are given together with the experimental data. The scale is the same for all panels on the plot. Hybrid functionals [187] give an overall three-fold increase of the VCA spectral function ($\alpha^2F(\omega)$). Our work shows that the octahedral rotations, even on the GGA level, transfer spectral weight towards lower frequencies (from ∼55 meV to ∼30 meV). The experimental results are taken from Ref. [173].

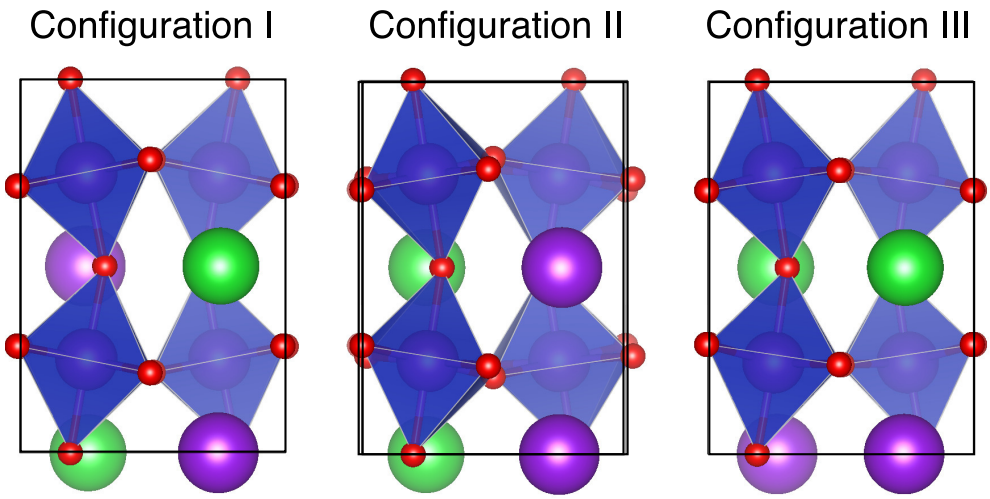

Figure 5.2: Three possible arrangements of the dopant atoms (K) in the 20 atom primitive unit cell of $Ba_{0.5}K_{0.5}BiO_3$. Atomic colors are: O - red, K - purple, Ba - green. Bi atoms are inside blue octahedra. All projections are along 110-direction (same as dominant octahedral tilt).

Table 5.1: Structural parameters of $BaBiO_3$ and $Ba_{0.5}K_{0.5}BiO_3$. For $Ba_{0.5}K_{0.5}BiO_3$ we show results for three different configurations of dopant (K) atoms (configurations I, II, and III), as well as for the virtual crystal approximation (VCA). Experimental data are shown in parentheses [172, 188]. This table shows the equilibrium unit cell volume V (in Å^3 per formula unit of $Ba_{0.5}K_{0.5}BiO_3$), the maximum and minimum Bi-O bond lengths (in Bohr) and octahedral tilt angles along [110] and [001] directions (in deg).

		Bi–O bond length		Octahedral tilt	
	V (Å^3)	Min. (Bohr)	Max. (Bohr)	[110] (deg)	[001] (deg)
$BaBiO_3$					
	87.02	4.19	4.39	13.4	6.5
	(82.21)	(4.01)	(4.19)	(12)	(6)
$Ba_{0.5}K_{0.5}BiO_3$					
Config. I	82.74	4.16	4.18	10.7	1.4
Config. II	83.02	4.16	4.18	8.8	2.6
Config. III	83.09	4.11	4.23	9.0	1.1
VCA	84.65	4.15	4.15	-	-
	(77.41)	(4.03)	(4.03)	(4.5)[1]	

The summary of the structural parameters for all systems studied in this work is given in Table 5.1. In the case of the undoped parent compound ($BaBiO_3$) we find that the fully relaxed structure has two kinds of structural distortions. First, there is a breathing distortion which reduces the Bi–O bond length for half of Bi atoms (4.19 Bohr), and increases it for the other half (4.39 Bohr). Second, there is a tilt of oxygen octahedra around both [110] and [001] directions (13.4° and 6.5°). Our calculation is in a good agreement with the experimental data for both Bi–O breathing and octahedral tilts. The unit cell volume is overestimated by 6% as compared to the experiment, as is commonly found in the GGA approximation.

The fully relaxed doped structure ($Ba_{0.5}K_{0.5}BiO_3$) has an almost negligible amount of Bi–O breathing distortion, unlike the parent compound. However, the doped compound still has a significant amount of octahedral tilts, especially around the [110] axis (between 8.8 and 10.8°). The amount of the tilt along the [001] axis is small: about 1-2°. The bond lengths and tilts obtained for the undoped compound are in a good agreement with the results of previous calculations [176, 177, 186, 189] and experimental data. Our calculations show that the unit cell volume of the doped structure is 5% lower than the volume of the parent compound. This is, again, in good agreement with experimental observation (6% lower).

5.1.2.2 Electronic structure

The electronic bandstructures and the densities of states (DOS) for all studied configurations are given in Fig. 5.3. The parent compound ($BaBiO_3$) is experimentally found to be have a semiconducting gap of 0.2 eV [190]. However in our GGA calculations, as well as in the previous theoretical studies [177, 183, 186] the parent compound is slightly semi-metallic (conduction band minimum is 0.3 eV below the Fermi level). The absence of the semiconducting gap in GGA calculations is not unusual for oxide systems. The width of the valence band is 0.9 eV and it has mostly oxygen 2p character (see right panels in Fig. 5.3). More extensive treatments of electronic correlation effects are able to reproduce semiconducting behavior of the parent compound [186].

The K-doped compound ($Ba_{0.5}K_{0.5}BiO_3$) is metallic in our calculation. The overall shape of the valence band is similar to that in the parent compound. However, the Fermi level (relative to the valence band maximum) is downshifted by 0.5-0.7 eV, and the width of the band is increased from 0.9 to 1.6 eV. Additionally, there is a series of band splittings on the order of 0.1-0.2 eV at the A and X points of the Brillouin zone. These splittings are present only for configurations II and III of the dopant atoms, while they nearly disappear in the configuration I during

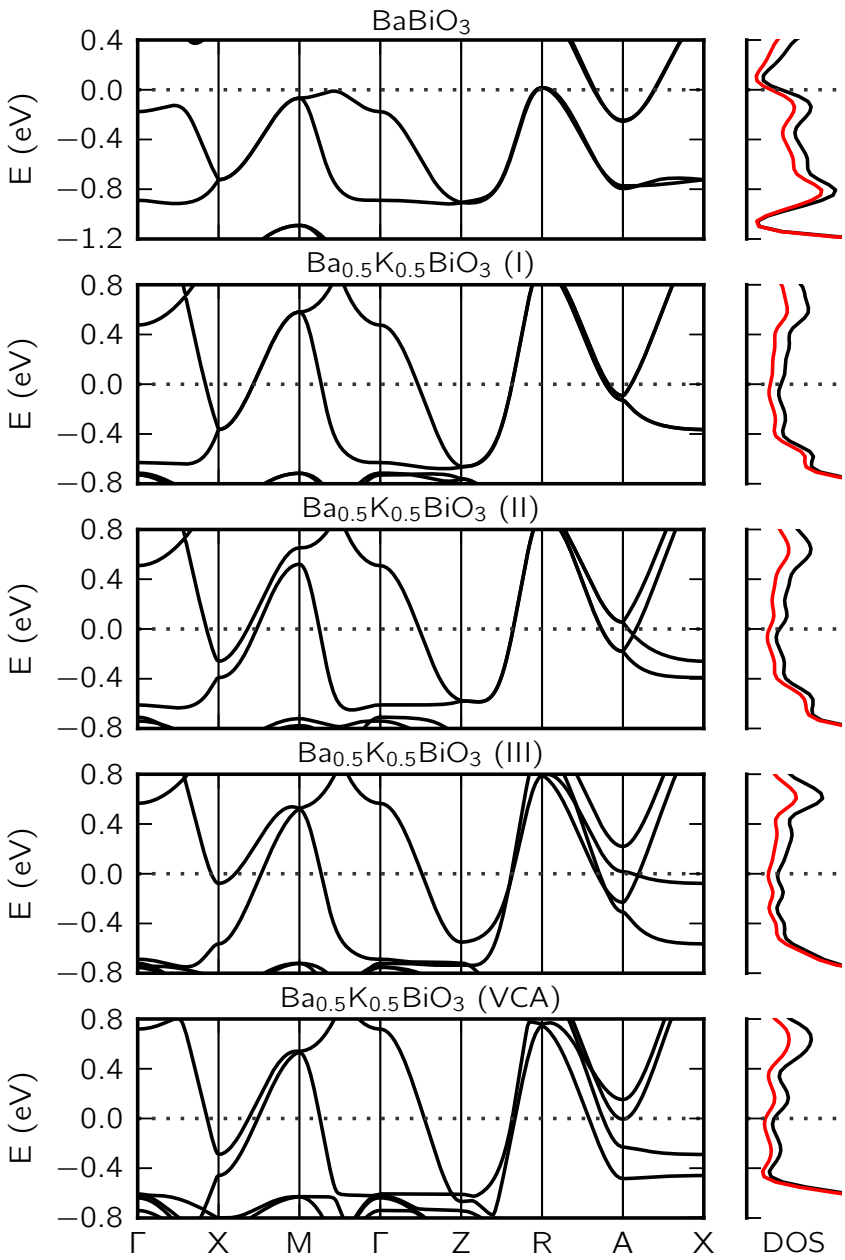

Figure 5.3: The electron band structure for a parent compound ($BaBiO_3$) and a doped compound ($Ba_{0.5}K_{0.5}BiO_3$) with different configurations of dopant atoms (I, II, and III, see Sec. 5.1.2.1). For comparison we also show the band structure using the virtual crystal approximation (VCA) in the folded Brillouin zone. Total densities of states (black) and the oxygen 2p partial density of states (red) are given in the small panel on the right.

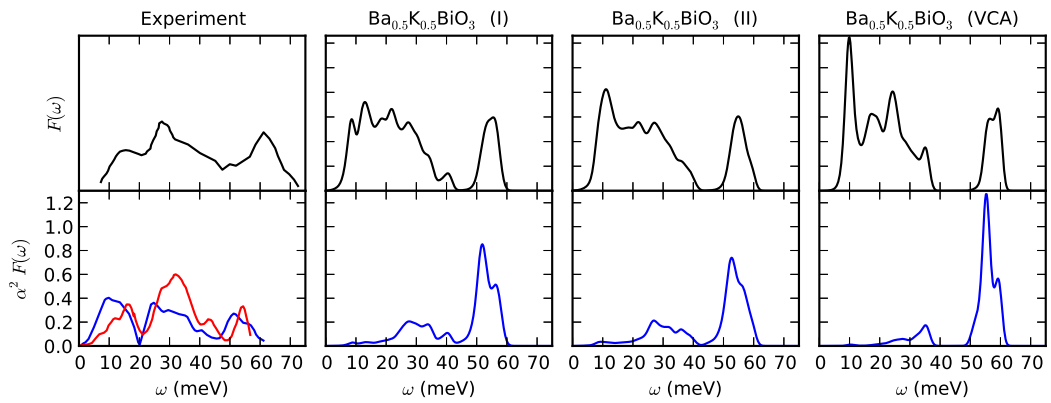

Figure 5.4: The phonon densities of states $F(\omega)$ (black, upper panel) and the Eliashberg spectral functions $\alpha^2F(\omega)$ (blue and red, lower panel). The experimental phonon density of states is from Ref. [173] and corresponds to $Ba_{1-x}K_xBiO_3$ with x=0.4. Two measured Eliashberg spectral functions (red and blue) are from the same Ref. [173] and they correspond to x=0.375. We also show calculated $F(\omega)$ and $\alpha^2F(\omega)$ from this work (x=0.5) for the configuration of dopant atoms I and II (see Sec. 5.1.2.1), as well as the calculation using virtual crystal approximation. The $F(\omega)$ is given in arbitrary units so that area under the curve is the same in each panel.

the structural relaxation. The band character of the valence band in the doped compound is oxygen-2p, same as in the case of the parent compound. The total density of states at the Fermi level varies within 5-10 % between configurations I, II, and III.

For comparison with earlier studies, we also calculate the bandstructure using the VCA. Overall, we find that the band structure of $Ba_{0.5}K_{0.5}BiO_3$ in the VCA has a similar (within 10%) bandwidth and density of states at the Fermi level as in our full 20-atom calculation. We find good agreement with previous similar studies regarding the bandstructures and partial densities of states [171, 177, 183, 186].

5.1.2.3 Phonons

The experimental and theoretical phonon densities of states for the doped compound are shown in the top four panels of Fig. 5.4. Our theoretical calculation shows that the intensity of the phonon density of states is concentrated in a broad low-energy region (10-40 meV) and in a narrower higher-energy region (55-60 meV). Small differences with respect to experiment may arise from the

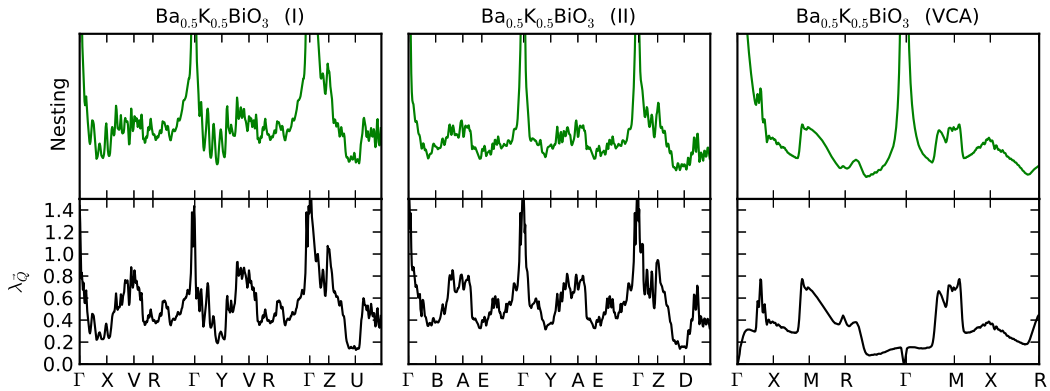

Figure 5.5: The Fermi surface nesting function [9, 58] (green, above) and the electron-phonon coupling $\lambda_{\vec{Q}}$ (black, below) along a path in the phonon Brillouin zone. We show results for $Ba_{0.5}K_{0.5}BiO_3$ both in the configurations I and II (see Sec. 5.1.2.1) and for the virtual crystal approximation (VCA). The nesting function is given in arbitrary units. In the plot we impose $\lambda_{\vec{Q},\nu}$ to be equal zero for small $\vec{Q}$ and ω_ν.

equilibrium volume overestimation of our GGA calculation. In our calculations, the low-energy region consists of the movement of the heavier atoms (Ba, K, Bi) with an admixture of oxygen displacement. The high-energy region is dominated by the oxygen modes.

For a comparison with earlier studies, we also calculated the phonon density of states using the virtual crystal approximation (VCA). We find a strong peak in the phonon density of states near 10 meV that is not present in our fully relaxed 20-atom unit cell calculation, or in experiment. In addition, the VCA overestimates the gap in the phonon density of states (near 45 meV). The gap separates the phonon modes involving the O-octahedra breathing at 55 meV from the rest.

We also studied the phonons of the undoped parent compound (not shown in Fig. 5.4) and find that it does not have a gap in the phonon density of states in agreement with experimental finding [178, 179].

5.1.2.4 Electron-phonon coupling

The experimental and theoretical Eliashberg spectral functions α^2F (Eq. 2.16) are shown in the bottom panels of Fig. 5.4. The experimental spectral function has a peak at ∼10–20, ∼30, and ∼55 meV. The 30 and 55 meV peaks are present in our

fully-relaxed 20-atom cell calculation, but with different magnitudes. In addition, α^2F is nearly zero at frequencies below 20 meV, unlike in the experiment.

The virtual crystal approximation (VCA) calculation of α^2F disagrees even more with the experiment. The middle peak (at 30 meV) is lower than in our fully-relaxed calculation while the high-energy peak (at 55 meV) is higher. The lowering of the spectral function near 30 meV is also responsible for a lower average electron-phonon coupling λ (Eq. 2.14) in VCA.

Figure 5.5 shows the electron-phonon coupling $\lambda_{\vec{Q}} = \sum_\nu \lambda_{\vec{Q},\nu}$ and the nesting function along a path inside the phonon Brillouin zone. The nesting function serves as a measure of how many potential electron scattering states are present at a particular wavevector $\vec{Q}$ [58],

$$\xi_{\vec{Q}} = \frac{1}{N_k} \sum_{\vec{k}} \delta(\epsilon_{\vec{k}})\delta(\epsilon_{\vec{k}+\vec{Q}}), \tag{5.1}$$

Where N_k is the total number of $\vec{k}$-vectors included in the sum and $\delta(\epsilon_{\vec{k}})$ is the Dirac delta-function.

In all of our calculations, the nesting function is nearly proportional to the electron-phonon coupling $\lambda_{\vec{Q}}$. Therefore, the strength of the electron-phonon interaction varies slowly throughout the phonon Brillouin zone.

5.1.2.5 Superconducting parameters

Table 5.2 gives the parameters used in our estimate of the superconducting transition temperature T_c. Shown are the square ($\sqrt{<\omega^2>}$) and the logarithmic average ($\omega_{\log}$) frequency moments of the Eliashberg spectral function, and the average electron-phonon coupling strength λ. We estimate the superconducting transition temperature using the McMillan formula [26] (Eq. 1.3). In the table we show the estimated T_c using a Coulomb parameter μ^*=0.0 and 0.1.

Using a fully relaxed 20-atom-cell we obtain λ=0.45 in configuration I and λ=0.48 in configuration II. These values produce T_c estimates of 4.2 and 3.2 K for $\mu^* = 0.1$ (14 and 12 K for $\mu^* = 0$). For the 20-atom case the logarithmic average frequency is 384 K in configuration I and 393 K in configuration II.

In the virtual crystal approximation we obtain $\lambda = 0.30$. This leads to a T_c of only 0.5 K for $\mu^* = 0.1$ (and 6.5 K for $\mu^* = 0.0$). The value of the logarithmic average frequency in the VCA is 575 K.

Table 5.2: Theoretical estimate of the superconducting transition temperature T_c obtained using the McMillan formula [26] (Eq. 1.3) with a Coulomb parameter μ^* given. We also show the square and logarithmic average frequencies [9] ($\sqrt{<\omega^2>}$ and $\omega_{\log}$), average electron-phonon coupling strength λ. The results for the doped configuration III (not shown here) were obtained only on a coarse grid 4×4×4 and are within 3-5% of the results for a configuration I and II.

	$\sqrt{<\omega^2>}$ (K)	$\omega_{\log}$ (K)	λ	T_c (K) μ^*=0.1	T_c (K) μ^*=0.0
$Ba_{0.5}K_{0.5}BiO_3$					
Config. I	480	393	0.48	4.2	14.0
Config. II	479	384	0.45	3.2	12.0
VCA	575	522	0.30	0.5	6.5

5.1.3 Discussion

The most striking disagreement between the theoretical and experimental Eliashberg spectral function α^2F is coming from the low frequency region between 10 and 40 meV (see Fig 5.4). The phonon spectrum in this region consists of movement of heavier atoms (Ba, Bi, K) with some admixture of the oxygen movement. The higher region of frequencies (above 40 meV) consists mostly of oxygen-breathing modes, and computed α^2F in that region is larger than in the experiment.

The only first-principle theoretical study with a λ and T_c close to the experimental values, is the hybrid-functional calculation from Ref. [187]. However, this agreement with experiment is achieved by an ad hoc rescaling of the electron-phonon coupling of the high-frequency (55 meV) oxygen-breathing phonon. Therefore this increase is in an opposite direction to what is required to have α^2F in better agreement with experiment. What is needed is that low-freqency (10-40 meV) α^2F increases, and high-frequency α^2F decreases.

Our work shows that the proper treatment of the atomic structure, especially the oxygen octahedra tilts can increase the electron-phonon coupling parameter λ by 50-60%. In addition, this increase comes mostly from an enhancement of the spectral weight for α^2F in the low frequency regime near 30 meV. Therefore, we propose that a more elaborate electron-correlation study (such as hybrid-functional from Ref. 17 or GW method) together with the proper treatment of the atomic structure may give α^2F in a better agreement with experiment. The combined effect of including electron-correlation and a complete treatment of the atomic structure need not be simply additive. We also speculate that disorder,

present in the spatial arrangement of K atoms, might further increase $\alpha^2 F$ in the 10-40 meV range.

5.1.4 Summary

We studied the electronic, vibrational, and electron-phonon properties of the $Ba_{0.5}K_{0.5}BiO_3$ superconductor. Unlike the previous studies, we perform calculations in the fully-relaxed 20-atom unit cell. We find that the presence of oxygen octahedra tilts increases the average electron-phonon coupling λ by 50-60% (from 0.3 to 0.48) as compared to the more conventionally used virtual crystal approximation (VCA) without tilts. This increase in λ originates from enhanced electron-phonon coupling at intermediate phonon frequencies (near 30 meV), but it is still not large enough to explain the experimentally obtained superconducting transition temperature. We suggest that the agreement may be improved further by an electron-correlation study going beyond the GGA (as in Ref. [187]) in combination with the inclusion of the oxygen octahedra tilts.

Chapter 6

Concluding remarks

Previous chapters of this manuscript came as a result of author's exciting journey through theoretical and computational studies of condensed matter. This journey allowed me to accumulate certain knowledge and hands-on experience that cannot be classified within only one, but rather includes partly all of of the following fields: physics, materials science, chemistry and computer science. The diversity of the materials studied in this work also shows how powerful and universal the first-principles techniques are. It this last chapter I (T.B.) would like to take an opportunity to share a personal view on the challenges that researchers are facing.

6.1 Current limitations and strong points

Current limitations of the first principles studies of superconductivity can be classified into two main categories: predictive power of the existing theoretical frameworks and the computational complexity of obtaining high precision results.

Both these aspects are heavily entangled. More predictive power often requires higher computational complexity. As an example, one can think about the GW method [32, 34] or the dynamical meanfield theory (DMFT) [191]. Both allow for a better treatment of electronic correlations (see eq. 2.2) than conventional DFT. At the same time, both GW and DMFT add another layer of computational complexity (since they use the DFT Kohn-Sham electronic states as input). As a rule of thumb: conventional DFT calculations for the same system are about one order of magnitude less expensive that both GW calculations of quasiparticle band structure or linear response calculations of the phonon spectra. It becomes apparent then why combining GW and phonon dispersions calculations, for example, is a challenging task [192].

6.1.1 Conventional/Class-I superconductors

In silico implementations of the Eliashberg theory give an example of a strong point of the first principles approaches. Superconductivity in MgB_2 [193, 194] was explained soon after it's discovery through computational application of Eliashberg formalism. These advances allow researchers to suggest new superconducting materials solely on the basis of the computational findings [100].

The complexity of the computational implementation, on the other hand, serves as a limitation for Eliashberg-based approaches. At this point in time, it prevents direct studies of complex systems with large crystal unit cells, as of now.

6.1.2 Unconventional/Class-II superconductors

Class-II materials are generally hard to study computationally because of their complex chemical composition that in many cases involves dopants and crystal disorder. In addition, electronic correlations beyond conventional DFT in class-II superconductors tend to be very important for a precise description of the electronic structure. Therefore an extensive treatment of electronic correlations is often required. When there is no clear understanding of the mechanisms of superconducting pairing, very little can be done about predicting new class-II

superconductors computationally. Nevertheless, first-principles approaches are proven very successful in providing explanation to many experimental findings [129].

6.2 Future prospects

Here is a summary of the author's vision of the field in the next few years.

6.2.1 Computational condensed matter physics

As many more areas of human activity become increasingly computerized, it is evident that more computational power is needed for solving problems in physics. Therefore rapid development of new and efficient application of the computational algorithms can be seen as a crucial factor in opening new frontiers of science. Advances in theoretical approaches and new experimental results will continue to generate demand for new computing capabilities. The constantly improving computer technologies in turn make it possible to obtain new scientific results by applying "old" analytical theory using faster computers, or to a newly discovered set of materials, or to materials that were previously too complicated to study.

Several initiatives on accumulating and documenting results of computations in condensed matter physics and materials science exist in the scientific community at the time of this writing (see Ref. [195] for example). The data they accumulate should make it possible for the future generations of researchers to coordinate efforts in studying complex materials.

6.2.2 Superconductivity

Advances in the research on superconductivity were largely driven by the discoveries of new materials with high transition temperature in the past: copper oxides in 1986 and iron compounds in 2008 [11, 15]. It is very likely that this trend will continue in the future, at least until a clear understanding of the underlying theory will make unconventional high-T_c superconductivity more open for theoretical predictions.

Extensive treatment of the electronic correlations and structural complexity will be reachable computationally when adequate computing support becomes available. The author expects the accuracy and predictive power of first-principles studies of superconductivity to improve significantly at that point, and then many new exciting results will emerge.

References

[1] H. K. Onnes. **The resistance of pure mercury at helium temperatures**. *Commun. Phys. Lab. Univ. Leiden*, **12**:120+, 1911. 1

[2] F. Bloch. **Uber die Quantenmechanik der Elektronen in Kristallgittern**. *Z. Phys.*, **52**:555, 1928. 1

[3] D. R. Hartree. **The Wave Mechanics of an Atom with a Non-Coulomb Central Field. Part I. Theory and Methods**. *Mathematical Proceedings of the Cambridge Philosophical Society*, **24**(01):89–110, 1928. 1

[4] P. Hohenberg and W. Kohn. **Inhomogeneous Electron Gas**. *Phys. Rev.*, **136**(3B):B864–B871, Nov 1964. 1, 10

[5] John Bardeen and David Pines. **Electron-Phonon Interaction in Metals**. *Phys. Rev.*, **99**(4):1140–1150, Aug 1955. 3

[6] J. Bardeen, L. N. Cooper, and J. R. Schrieffer. **Theory of Superconductivity**. *Phys. Rev.*, **108**(5):1175–1204, Dec 1957. 3

[7] G. M. Eliashberg. **Interaction between electrons and lattice vibrations in a superconductor**. *Sov. Phys. JETP*, **11**:696, 1960. 4

[8] L. P. Gorkov. **On the energy spectrum of superconductors**. *Sov. Phys. JETP*, **7**:505, 1958. 4

[9] P.B. Allen and Mitrovic B. *Solid state physics Vol. 32.* Academic, New York, 1982. 4, 12, 13, 39, 51, 52, 98, 100

[10] W. L. McMillan. **Transition Temperature of Strong-Coupled Superconductors**. *Phys. Rev.*, **167**:331–344, Mar 1968. 4, 14

[11] J. G. Bednorz and K. A. Müller. **Possible high T_c superconductivity in the Ba-La-Cu-O system**. *Zeitschrift fur Physik B Condensed Matter*, **64**:189–193, 1986. 6, 105

[12] D. J. Scalapino. **Superconductivity and Spin Fluctuations**. *arXiv:9908287v2*, 1999. 7, 19

[13] D. J. Scalapino, E. Loh, and J. E. Hirsch. **d-wave pairing near a spin-density-wave instability**. *Phys. Rev. B*, **34**:8190–8192, Dec 1986. 7

[14] David Pines. **Finding New Superconductors: The Spin-Fluctuation Gateway to High Tc and Possible Room Temperature Superconductivity**. *The Journal of Physical Chemistry B*, **117**(42):13145–13153, 2013. 7

[15] Yoichi Kamihara, Takumi Watanabe, Masahiro Hirano, and Hideo Hosono. **Iron-Based Layered Superconductor $La[O_{1-x}F_x]FeAs$ (x = 0.050.12) with Tc = 26 K**. *Journal of the American Chemical Society*, **130**(11):3296–3297, 2008. 7, 105

[16] Johnpierre Paglione and Richard L. Greene. **High-temperature superconductivity in iron-based materials**. *Nat Phys*, **advance online publication**:–, August 2010. 7, 8, 55, 69, 76, 79

[17] I. I. Mazin, D. J. Singh, M. D. Johannes, and M. H. Du. *Phys. Rev. Lett.*, **101**:057003, 2008. 7, 83, 88

[18] I. I. Mazin. **Symmetry analysis of possible superconducting states in $K_xFe_ySe_2$ superconductors**. *Phys. Rev. B*, **84**:024529, Jul 2011. 7, 56, 79

[19] W. Kohn and L. J. Sham. **Self-Consistent Equations Including Exchange and Correlation Effects**. *Phys. Rev.*, **140**(4A):A1133–A1138, Nov 1965. 10

[20] J. P. Perdew and Alex Zunger. **Self-interaction correction to density-functional approximations for many-electron systems**. *Phys. Rev. B*, **23**(10):5048–5079, May 1981. 10, 21, 23

[21] J. P. Perdew. **Accurate density functional for the energy: Real-space cutoff of the gradient expansion for the exchange hole**. *Phys. Rev. Lett.*, **55**:1665–1668, October 1985. 10

[22] X. Gonze. **Adiabatic density-functional perturbation theory**. *Phys. Rev. A*, **52**:1096–1114, August 1995. 10

[23] G. Grimvall. *The electron-phonon interaction in metals.* North-Holland, New York, 1981. 12, 13

[24] N.E. Phillips. *Low-temperature Heat Capacity of Metals.* CRC critical reviews in solid state sciences. 1971. 12

[25] P.B. Allen. *Dynamical Properties of Solids.* North-Holland, Amsterdam, 1980. 13

[26] P.B. Allen and R.C. Dynes. **Transition temperature of strong-coupled superconductors reanalyzed**. *Phys. Rev. B*, **12**(3):905–922, Aug 1975. 14, 26, 28, 30, 35, 39, 40, 41, 44, 52, 57, 65, 72, 99, 100

[27] Feliciano Giustino, Marvin L. Cohen, and Steven G. Louie. **Electron-phonon interaction using Wannier functions**. *Phys. Rev. B*, **76**(16):165108, Oct 2007. 15, 21, 22, 23, 92

[28] Nicola Marzari and David Vanderbilt. **Maximally localized generalized Wannier functions for composite energy bands**. *Phys. Rev. B*, **56**(20):12847–12865, Nov 1997. 15

[29] Ivo Souza, Nicola Marzari, and David Vanderbilt. **Maximally localized Wannier functions for entangled energy bands**. *Phys. Rev. B*, **65**(3):035109, Dec 2001. 21, 22, 23

[30] Arash A. Mostofi, Jonathan R. Yates, Young-Su Lee, Ivo Souza, David Vanderbilt, and Nicola Marzari. **wannier90: A tool for obtaining maximally-localised Wannier functions**. *Computer Physics Communications*, **178**(9):685–699, 2008. 15, 22, 23

[31] J. Deslippe, G. Samsonidze, D. A. Strubbe, M. Jain, M. L. Cohen, and S. G. Louie. *Comput. Phys. Commun.*, **183**:1269, 2012. 18, 19

[32] Mark S. Hybertsen and Steven G. Louie. **First-Principles Theory of Quasiparticles: Calculation of Band Gaps in Semiconductors and Insulators**. *Phys. Rev. Lett.*, **55**(13):1418–1421, Sep 1985. 18, 103

[33] J. P. Perdew and Y. Wang. **Accurate and simple analytic representation of the electron-gas correlation energy**. *Phys. Rev. B*, **45**:13244–13249, June 1992. 19

[34] Lars Hedin. **New Method for Calculating the One-Particle Green's Function with Application to the Electron-Gas Problem**. *Phys. Rev.*, **139**(3A):A796–A823, Aug 1965. 19, 103

[35] C. A. Kukkonen and A. W. Overhauser. *Phys. Rev. B*, **20**:550, 1979. 19

[36] Keun-Ho Lee, K. J. Chang, and Marvin L. Cohen. **First-principles calculations of the Coulomb pseudopotential mu^*: Application to Al**. *Phys. Rev. B*, **52**:1425–1428, Jul 1995. 20, 42

[37] Philip B. Allen and Marvin L. Cohen. **Pseudopotential Calculation of the Mass Enhancement and Superconducting Transition**

Temperature of Simple Metals. *Phys. Rev.*, **187**(2):525–538, Nov 1969. 21, 25, 26, 34

[38] D.M. Ceperley and B.J. Alder. **Ground State of the Electron Gas by a Stochastic Method**. *Phys. Rev. Lett.*, **45**(7):566–569, Aug 1980. 21

[39] John P. Perdew, Kieron Burke, and Matthias Ernzerhof. **Generalized Gradient Approximation Made Simple**. *Phys. Rev. Lett.*, **77**:3865–3868, Oct 1996. 21

[40] J Ihm, A Zunger, and M.L. Cohen. **Momentum-space formalism for the total energy of solids**. *Journal of Physics C: Solid State Physics*, **12**(21):4409, 1979. 21

[41] N. Troullier and J.L. Martins. **Efficient pseudopotentials for plane-wave calculations**. *Phys. Rev. B*, **43**(3):1993–2006, Jan 1991. 21

[42] Marvin L Cohen. **Pseudopotentials and Total Energy Calculations**. *Physica Scripta*, **1982**(T1):5, 1982. 21

[43] Paolo Giannozzi, Stefano Baroni, Nicola Bonini, Matteo Calandra, Roberto Car, Carlo Cavazzoni, Davide Ceresoli, Guido L Chiarotti, Matteo Cococcioni, Ismaila Dabo, Andrea Dal Corso, Stefano de Gironcoli, Stefano Fabris, Guido Fratesi, Ralph Gebauer, Uwe Gerstmann, Christos Gougoussis, Anton Kokalj, Michele Lazzeri, Layla Martin-Samos, Nicola Marzari, Francesco Mauri, Riccardo Mazzarello, Stefano Paolini, Alfredo Pasquarello, Lorenzo Paulatto, Carlo Sbraccia, Sandro Scandolo, Gabriele Sclauzero, Ari P Seitsonen, Alexander Smogunov, Paolo Umari, and Renata M Wentzcovitch. **QUANTUM ESPRESSO: a modular and open-source software project for quantum simulations of materials**. *Journal of Physics: Condensed Matter*, **21**(39):395502, 2009. 21, 22

[44] J. B. Neaton and N. W. Ashcroft. **Pairing in dense lithium**. *Nature*, **400**(6740):141–144, jul 1999. 21, 25, 35, 40

[45] Stefano Baroni, Stefano de Gironcoli, Andrea Dal Corso, and Paolo Giannozzi. **Phonons and related crystal properties from density-functional perturbation theory**. *Rev. Mod. Phys.*, **73**(2):515–562, Jul 2001. 21, 22, 23

[46] Jesse Noffsinger, Feliciano Giustino, Brad D. Malone, Cheol-Hwan Park, Steven G. Louie, and Marvin L. Cohen. **EPW: A**

program for calculating the electron-phonon coupling using maximally localized Wannier functions. *Computer Physics Communications*, **181**(12):2140 – 2148, 2010. 21, 22, 23

[47] A. Kokalj. **Computer graphics and graphical user interfaces as tools in simulations of matter at the atomic scale**. *Comput. Mater. Sci.*, **28**:155–168, 2003. 22

[48] Fong-Chi Hsu, Jiu-Yong Luo, Kuo-Wei Yeh, Ta-Kun Chen, Tzu-Wen Huang, Phillip M. Wu, Yong-Chi Lee, Yi-Lin Huang, Yan-Yi Chu, Der-Chung Yan, and Maw-Kuen Wu. **Superconductivity in the PbO-type structure α-FeSe**. *Proc. of the Nat. Acad. of Sci.*, **105**(38):14262–14264, 2008. 23, 56, 69, 74

[49] Timur Bazhirov, Jesse Noffsinger, and Marvin L. Cohen. **Superconductivity and electron-phonon coupling in lithium at high pressures**. *Phys. Rev. B*, **82**(18):184509, Nov 2010. 24, 25, 28, 30, 32, 49, 61

[50] Timur Bazhirov, Jesse Noffsinger, and Marvin L. Cohen. **Electron-phonon coupling in bcc lithium**. *Phys. Rev. B*, **84**:125122, Sep 2011.

[51] Timur Bazhirov, Yuki Sakai, Susumu Saito, and Marvin L. Cohen. **Electron-phonon coupling and superconductivity in Li-intercalated layered borocarbide compounds**. *under review at Phys. Rev. B.* 24

[52] Amy Y. Liu, Andrew A. Quong, J. K. Freericks, E. J. Nicol, and Emily C. Jones. **Structural phase stability and electron-phonon coupling in lithium**. *Phys. Rev. B*, **59**(6):4028–4035, Feb 1999. 25, 26, 32, 34

[53] Amy Y. Liu and Marvin L. Cohen. **Electron-phonon coupling in bcc and 9R lithium**. *Phys. Rev. B*, **44**(17):9678–9684, Nov 1991.

[54] T. Jarlborg. **Electronic and magnetic structures in BCC and HCP Li under pressure**. *Physica Scripta*, **37**:795–799, May 1988. 26

[55] Norman E. Phillips. **Low-temperature Heat Capacity of Metals**. *Crit. Rev. Sol. St.*, **2**:467, 1971. 26

[56] D. A. Papaconstantopoulos, L. L. Boyer, B. M. Klein, A. R. Williams, V. L. Morruzzi, and J. F. Janak. **Calculations of the superconducting properties of 32 metals with $Z \leq 49$**. *Phys. Rev. B*, **15**(9):4221–4226, May 1977. 26

[57] N. E. Christensen and D. L. Novikov. **Predicted Superconductive Properties of Lithium under Pressure**. *Phys. Rev. Lett.*, **86**(9):1861–1864, Feb 2001. 26, 34, 35

[58] Deepa Kasinathan, J. Kuneš, A. Lazicki, H. Rosner, C. S. Yoo, R. T. Scalettar, and W. E. Pickett. **Superconductivity and Lattice Instability in Compressed Lithium from Fermi Surface Hot Spots**. *Phys. Rev. Lett.*, **96**(4):047004, Feb 2006. 26, 30, 35, 39, 40, 41, 49, 51, 98, 99

[59] G. Profeta, C. Franchini, N. N. Lathiotakis, A. Floris, A. Sanna, M. A. L. Marques, M. Lüders, S. Massidda, E. K. U. Gross, and A. Continenza. **Superconductivity in Lithium, Potassium, and Aluminum under Extreme Pressure: A First-Principles Study**. *Phys. Rev. Lett.*, **96**(4):047003, Feb 2006. 26, 35, 42

[60] Yansun Yao, J. S. Tse, K. Tanaka, F. Marsiglio, and Y. Ma. **Superconductivity in lithium under high pressure investigated with density functional and Eliashberg theory**. *Phys. Rev. B*, **79**(5):054524, Feb 2009. 25, 34, 35, 39

[61] Juha Tuoriniemi, Kirsi Juntunen-Nurmilaukas, Johanna Uusvuori, Elias Pentti, Anssi Salmela, and Alexander Sebedash. **Superconductivity in lithium below 0.4 millikelvin at ambient pressure**. *Nature*, **447**:187–189, 2007. 25, 34

[62] M. Hanfland, K. Syassen, N. E. Christensen, and D. L. Novikov. **New high-pressure phases of lithium**. *Nature*, **408**:174–178, 2000. 25, 34

[63] W. Schwarz and O. Blaschko. **Polytype structures of lithium at low temperatures**. *Phys. Rev. Lett.*, **65**(25):3144–3147, Dec 1990.

[64] A. W. Overhauser. **Crystal Structure of Lithium at 4.2 K**. *Phys. Rev. Lett.*, **53**(1):64–65, Jul 1984. 32

[65] G. Ernst, C. Artner, O. Blaschko, and G. Krexner. **Low-temperature martensitic phase transition of bcc lithium**. *Phys. Rev. B*, **33**(9):6465–6469, May 1986. 25

[66] M. Hanfland, I. Loa, K. Syassen, U. Schwarz, and K. Takemura. **Equation of state of lithium to 21 GPa**. *Solid State Communications*, **112**(3):123 – 127, 1999. 25, 26, 34, 35

[67] Katsuya Shimizu, Hiroto Ishikawa, Daigoroh Takao, Takehiko Yagi, and Kiichi Amaya. **New high-pressure phases of lithium**. *Nature*, **419**:597–599, 2002. 34, 40, 41

[68] Viktor V. Struzhkin, Mikhail I. Eremets, Wei Gan, Ho-kwang Mao, and Russell J. Hemley. **Superconductivity in Dense Lithium**. *Science*, **298**(5596):1213–1215, 2002.

[69] Shanti Deemyad and James S. Schilling. **Superconducting Phase Diagram of Li Metal in Nearly Hydrostatic Pressures up to 67 GPa**. *Phys. Rev. Lett.*, **91**(16):167001, Oct 2003. 34, 40, 41

[70] T Matsuoka, S Onoda, M Kaneshige, Y Nakamoto, K Shimizu, T Kagayama, and Y Ohishi. **Superconductivity and crystal structure of lithium under high pressure**. *Journal of Physics: Conference Series*, **121**(5):052003, 2008. 34, 41, 42

[71] Takahiro Matsuoka and Katsuya Shimizu. **Direct observation of a pressure-induced metal-to-semiconductor transition in lithium**. *Nature*, **458**(7235):186–189, Mar 2009. 25, 34, 35, 41

[72] R. Szczesniak. **On the Coulomb pseudopotential for Al and Pb superconductors**. *physica status solidi (b)*, **244**(7):2538–2542, 2007. 30, 32

[73] Keun-Ho Lee and K. J. Chang. **Linear-response calculation of the Coulomb pseudopotential $\mu*$ for Nb**. *Phys. Rev. B*, **54**(3):1419–1422, Jul 1996. 32, 42

[74] C. F. Richardson and N. W. Ashcroft. **Effective electron-electron interactions and the theory of superconductivity**. *Phys. Rev. B*, **55**(22):15130–15145, Jun 1997. 32, 42

[75] E. Wigner and F. Seitz. **On the Constitution of Metallic Sodium**. *Phys. Rev.*, **43**(10):804–810, May 1933. 34

[76] V. E. Fortov, V. V. Yakushev, K. L. Kagan, I. V. Lomonosov, V. I. Postnov, and T. I. Yakusheva. **Anomalous electric conductance of lithium under quiasi-isoentropic compression to 60 GPa (0.6 MBar). Transition to molecular state?** *JETP letters*, **70**:628, 1999. 34

[77] Deepa Kasinathan, K. Koepernik, J. Kuneš, H. Rosner, and W. E. Pickett. **Origin of strong coupling in lithium under pressure**. *Physica C*, **460-462**:133, 2007. 35, 39

[78] Lei Shi and D. A. Papaconstantopoulos. **Theoretical predictions of superconductivity in alkali metals under high pressure**. *Phys. Rev. B*, **73**(18):184516, May 2006. 41

[79] N. B. Hannay, T. H. Geballe, B. T. Matthias, K. Andres, P. Schmidt, and D. MacNair. **Superconductivity in Graphitic Compounds**. *Phys. Rev. Lett.*, **14**:225–226, February 1965. 44

[80] I. Belash. **Superconductivity of graphite intercalation compound with lithium C2Li**. *Solid State Commun.*, **69**:921–923, March 1989. 44

[81] M. Calandra and F. Mauri. **Theoretical Explanation of Superconductivity in C_6Ca**. *Phys. Rev. Lett.*, **95**(23):237002, December 2005.

[82] G. Csányi, P. B. Littlewood, A. H. Nevidomskyy, C. J. Pickard, and B. D. Simons. **The role of the interlayer state in the electronic structure of superconducting graphite intercalated compounds**. *Nature Phys.*, **1**:42–45, October 2005.

[83] N. Emery, C. Hérold, M. D'Astuto, V. Garcia, C. Bellin, J. F. Marêché, P. Lagrange, and G. Loupias. **Superconductivity of Bulk CaC_6**. *Phys. Rev. Lett.*, **95**(8):087003, August 2005.

[84] I. I. Mazin. **Intercalant-Driven Superconductivity in YbC_6 and CaC_6**. *Phys. Rev. Lett.*, **95**(22):227001, November 2005.

[85] T. E. Weller, M. Ellerby, S. S. Saxena, R. P. Smith, and N. T. Skipper. **Superconductivity in the intercalated graphite compounds C_6Yb and C_6Ca**. *Nature Phys.*, **1**:39–41, October 2005.

[86] A. Gauzzi, S. Takashima, N. Takeshita, C. Terakura, H. Takagi, N. Emery, C. Hérold, P. Lagrange, and G. Loupias. **Enhancement of Superconductivity and Evidence of Structural Instability in Intercalated Graphite CaC_6 under High Pressure**. *Phys. Rev. Lett.*, **98**(6):067002, February 2007.

[87] A. Sanna, G. Profeta, A. Floris, A. Marini, E. K. U. Gross, and S. Massidda. **Anisotropic gap of superconducting CaC_6 : A first-principles density functional calculation**. *Phys. Rev. B*, **75**(2):020511, January 2007.

[88] Gianni Profeta, Matteo Calandra, and Francesco Mauri. **Phonon-mediated superconductivity in graphene by lithium deposition**. *Nat Phys*, **8**(2):131–134, Feb 2012. 44

[89] Jun Nagamatsu, Norimasa Nakagawa, Takahiro Muranaka, Yuji Zenitani, and Jun Akimitsu. **Superconductivity at 39[thinsp]K in magnesium diboride**. *Nature*, **410**(6824):63–64, mar 2001. 44

[90] J. M. An and W. E. Pickett. **Superconductivity of MgB_2: Covalent Bonds Driven Metallic**. *Phys. Rev. Lett.*, **86**:4366–4369, May 2001. 44

[91] K.-P. Bohnen, R. Heid, and B. Renker. **Phonon Dispersion and Electron-Phonon Coupling in MgB_2 and AlB_2**. *Phys. Rev. Lett.*, **86**:5771–5774, June 2001.

[92] J. Kortus, I. I. Mazin, K. D. Belashchenko, V. P. Antropov, and L. L. Boyer. **Superconductivity of Metallic Boron in MgB_2**. *Phys. Rev. Lett.*, **86**:4656–4659, May 2001.

[93] H. J. Choi, D. Roundy, H. Sun, M. L. Cohen, and S. G. Louie. **First-principles calculation of the superconducting transition in MgB_2 within the anisotropic Eliashberg formalism**. *Phys. Rev. B*, **66**(2):020513, July 2002. 44

[94] H. Rosner, A. Kitaigorodsky, and W. E. Pickett. **Prediction of High T_c Superconductivity in Hole-Doped LiBC**. *Phys. Rev. Lett.*, **88**(12):127001, March 2002. 44

[95] G. Mair, M. Schwarz, and H. G. Schnering. **LiBC - ein vollstandig interkalierter Heterographit**. *Z. Anorg. Allg. Chem.*, **621**:1153–1159, 1995. 44

[96] A. M. Fogg, J. Meldrum, G. R. Darling, J. B. Claridge, and M. J. Rosseinsky. **Chemical Control of Electronic Structure and Superconductivity in Layered Borides and Borocarbides: Understanding the Absence of Superconductivity in LixBC**. *J. Am. Chem. Soc.*, **128**:10043–10053, 2006. 44

[97] A. Bharathi, Balaselvi. S. J., M. Premila, T. N. Sairam, G. L. N. Reddy, C. S. Sundar, and Y. Hariharan. **Synthesis and search for superconductivity in LiBC**. *Solid State Commun.*, **124**:423–428, December 2002.

[98] A. M. Fogg, P. R. Chalker, J. B. Claridge, G. R. Darling, and M. J. Rosseinsky. **LiBC electronic, vibrational, structural, and low-temperature chemical behavior of a layered material isoelectronic with MgB_2**. *Phys. Rev. B*, **67**(24):245106, June 2003.

[99] D. Souptel, Z. Hossain, G. Behr, W. Löser, and C. Geibel. **Synthesis and physical properties of LiBC intermetallics**. *Solid State Commun.*, **125**:17–21, January 2003. 44

[100] M. Gao, Z.-Y. Lu, and T. Xiang. **Prediction of phonon-mediated high temperature superconductivity in stoichiometric Li$_2$B$_3$C**. *ArXiv e-prints*, July 2013. 44, 47, 49, 52, 103

[101] R. Miao, J. Yang, M. Jiang, Q. Zhang, D. Cai, C. Fan, Z. Bai, C. Liu, F. Wu, and S. Ma. **First-principles study of superconductivity in the hole self-doped LiB1.1C0.9**. *J. Appl. Phys.*, **113**(13):133910, April 2013. 44

[102] J. Noffsinger, F. Giustino, B. D. Malone, C.-H. Park, S. G. Louie, and M. L. Cohen. **EPW: A program for calculating the electron-phonon coupling using maximally localized Wannier functions**. *Comput. Phys. Commun.*, **181**:2140–2148, December 2010. 44

[103] D. Tomanek, R. M. Wentzcovitch, S. G. Louie, and M. L. Cohen. **Calculation of electronic and structural properties of BC_3**. *Phys. Rev. B*, **37**:3134–3136, February 1988. 45

[104] R. M. Wentzcovitch, M. L. Cohen, and S. G. Louie. **Comparative study of the density of states of graphite and BC_3**. *Phys. Lett. A*, **131**:457–460, September 1988.

[105] H. Sun, F. J. Ribeiro, J.-L. Li, D. Roundy, M. L. Cohen, and S. G. Louie. **Ab initio pseudopotential studies of equilibrium lattice structures and phonon modes of bulk BC_3**. *Phys. Rev. B*, **69**(2):024110, January 2004.

[106] F. J. Ribeiro and M. L. Cohen. **Possible superconductivity in hole-doped BC_3**. *Phys. Rev. B*, **69**(21):212507, June 2004. 45

[107] J. Kouvetakis, R. B. Kaner, M. L. Sattler, and N. Bartlett. **A Novel Graphite-Like Material of Composition BC_3, and Nitrogen-Carbon Graphites**. *J. Chem. Soc. Chem .Commun.*, **1986**:1758–1759, 1986. 45

[108] Timur Bazhirov and Marvin L. Cohen. **Spin-resolved electron-phonon coupling in FeSe and KFe_2Se_2**. *under review at Phys. Rev. B*, (18). 54

[109] Timur Bazhirov and Marvin L Cohen. **Effects of charge doping and constrained magnetization on the electronic structure of an FeSe monolayer**. *Journal of Physics: Condensed Matter*, **25**(10):105506, 2013. 54

[110] T. M. McQueen, Q. Huang, V. Ksenofontov, C. Felser, Q. Xu, H. Zandbergen, Y. S. Hor, J. Allred, A. J. Williams, D. Qu, J. Checkelsky, N. P. Ong, and R. J. Cava. **Extreme sensitivity**

of superconductivity to stoichiometry in $Fe_{1+\delta}Se$. *Phys. Rev. B*, **79**:014522, Jan 2009. 56

[111] S. Medvedev, T. M. McQueen, I. A. Troyan, T. Palasyuk, M. I. Eremets, R. J. Cava, S. Naghavi, F. Casper, V. Ksenofontov, G. Wortmann, and C. Felser. **Electronic and magnetic phase diagram of [beta]-Fe1.01Se with superconductivity at 36.7[thinsp]K under pressure**. *Nat Mater*, **8**(8):630–633, aug 2009. 56, 72, 74

[112] Yoshikazu Mizuguchi, Fumiaki Tomioka, Shunsuke Tsuda, Takahide Yamaguchi, and Yoshihiko Takano. **Superconductivity at 27 K in tetragonal FeSe under high pressure**. *Applied Physics Letters*, **93**(15):152505, 2008. 56, 72

[113] T. Imai, K. Ahilan, F. L. Ning, T. M. McQueen, and R. J. Cava. **Why Does Undoped FeSe Become a High-T_c Superconductor under Pressure?** *Phys. Rev. Lett.*, **102**:177005, Apr 2009. 56, 69

[114] Can-Li Song, Yi-Lin Wang, Peng Cheng, Ye-Ping Jiang, Wei Li, Tong Zhang, Zhi Li, Ke He, Lili Wang, Jin-Feng Jia, Hsiang-Hsuan Hung, Congjun Wu, Xucun Ma, Xi Chen, and Qi-Kun Xue. **Direct Observation of Nodes and Twofold Symmetry in FeSe Superconductor**. *Science*, **332**(6036):1410–1413, 2011. 56

[115] R Khasanov, M Bendele, K Conder, H Keller, E Pomjakushina, and V Pomjakushin. **Iron isotope effect on the superconducting transition temperature and the crystal structure of FeSe 1 x**. *New Journal of Physics*, **12**(7):073024, 2010. 56

[116] Qing-Yan Wang, Zhi Li, Wen-Hao Zhang, Zuo-Cheng Zhang, Jin-Song Zhang, Wei Li, Hao Ding, Yun-Bo Ou, Peng Deng, Kai Chang, Jing Wen, Can-Li Song, Ke He, Jin-Feng Jia, Shuai-Hua Ji, Yayu Wang, Lili Wang, Xi Chen, Xucun Ma, and Qi-Kun Xue. **Interface induced high temperature superconductivity in single unit-cell FeSe films on SrTiO3**. *arXiv:1201.5694v1*. 56

[117] Can-Li Song, Yi-Lin Wang, Ye-Ping Jiang, Zhi Li, Lili Wang, Ke He, Xi Chen, Xu-Cun Ma, and Qi-Kun Xue. **Molecular-beam epitaxy and robust superconductivity of stoichiometric FeSe crystalline films on bilayer graphene**. *Phys. Rev. B*, **84**:020503, Jul 2011. 56, 74

[118] Jiangang Guo, Shifeng Jin, Gang Wang, Shunchong Wang, Kaixing Zhu, Tingting Zhou, Meng He, and Xiaolong Chen. **Superconductivity in the iron selenide $K_xFe_2Se_2$** ($0 \leq x \leq 1.0$). *Phys. Rev. B*, **82**:180520, Nov 2010. 56, 69

[119] A Krzton-Maziopa, Z Shermadini, E Pomjakushina, V Pomjakushin, M Bendele, A Amato, R Khasanov, H Luetkens, and K Conder. **Synthesis and crystal growth of Cs 0.8 (FeSe 0.98) 2 : a new iron-based superconductor with T c = 27 K**. *Journal of Physics: Condensed Matter*, **23**(5):052203, 2011. 56

[120] Z. Shermadini, A. Krzton-Maziopa, M. Bendele, R. Khasanov, H. Luetkens, K. Conder, E. Pomjakushina, S. Weyeneth, V. Pomjakushin, O. Bossen, and A. Amato. **Coexistence of Magnetism and Superconductivity in the Iron-Based Compound** $Cs_{0.8}(FeSe_{0.98})_2$. *Phys. Rev. Lett.*, **106**:117602, Mar 2011. 56

[121] Bao Wei, Huang Qing-Zhen, Chen Gen-Fu, M. A. Green, Wang Du-Ming, He Jun-Bao, and Qiu Yi-Ming. **A Novel Large Moment Antiferromagnetic Order in K 0.8 Fe 1.6 Se 2 Superconductor**. *Chinese Physics Letters*, **28**(8):086104, 2011. 56

[122] Weiqiang Yu, L. Ma, J. B. He, D. M. Wang, T.-L. Xia, G. F. Chen, and Wei Bao. ^{77}Se **NMR Study of the Pairing Symmetry and the Spin Dynamics in** $K_yFe_{2-x}Se_2$. *Phys. Rev. Lett.*, **106**:197001, May 2011. 56

[123] A. M. Zhang, K. Liu, J. H. Xiao, J. B. He, D. M. Wang, G. F. Chen, B. Normand, and Q. M. Zhang. **Vacancy ordering and phonon spectrum of the iron-based superconductor** $\mathbf{K_{0.8}Fe_{1.6}Se_2}$. *Phys. Rev. B*, **85**:024518, Jan 2012. 56

[124] Bao Wei, Huang Qing-Zhen, Chen Gen-Fu, M. A. Green, Wang Du-Ming, He Jun-Bao, and Qiu Yi-Ming. **A Novel Large Moment Antiferromagnetic Order in K 0.8 Fe 1.6 Se 2 Superconductor**. *Chinese Physics Letters*, **28**(8):086104, 2011. 56

[125] T. Qian, X.-P. Wang, W.-C. Jin, P. Zhang, P. Richard, G. Xu, X. Dai, Z. Fang, J.-G. Guo, X.-L. Chen, and H. Ding. **Absence of a Holelike Fermi Surface for the Iron-Based** $K_{0.8}Fe_{1.7}Se_2$ **Superconductor Revealed by Angle-Resolved Photoemission Spectroscopy**. *Phys. Rev. Lett.*, **106**:187001, May 2011. 56

[126] Y. Zhang, L. X. Yang, M. Xu, Z. R. Ye, F. Chen, C. He, H. C. Xu, J. Jiang, B. P. Xie, J. J. Ying, X. F. Wang, X. H. Chen, J. P. Hu, M. Matsunami, S. Kimura, and D. L. Feng. **Nodeless superconducting gap in AxFe2Se2 (A=K,Cs) revealed by angle-resolved photoemission spectroscopy**. *Nat Mater*, **10**(4):273–277, April 2011. 56, 70

[127] Alaska Subedi, Lijun Zhang, D. J. Singh, and M. H. Du. **Density functional study of FeS, FeSe, and FeTe: Electronic structure, magnetism, phonons, and superconductivity**. *Phys. Rev. B*, **78**(13):134514, Oct 2008. 56, 57, 75, 84

[128] Chao Cao and Jian-Hui Dai. **Electronic Structure of KFe 2 Se 2 from First-Principles Calculations**. *Chinese Physics Letters*, **28**(5):057402, 2011. 56, 69, 70, 79

[129] I.I. Mazin and J. Schmalian. **Pairing symmetry and pairing state in ferropnictides: Theoretical overview**. *Physica C: Superconductivity*, **469**(9–12):614 – 627, 2009. 56, 79, 104

[130] L. Boeri, M. Calandra, I. I. Mazin, O. V. Dolgov, and F. Mauri. **Effects of magnetism and doping on the electron-phonon coupling in** $BaFe2As2$. *Phys. Rev. B*, **82**(2):020506, Jul 2010. 56

[131] Wei Wang, Jiafa Sun, and Suwen Li. **Mode softening and phononic-crystal-like behavior of FeSe**. *Applied Physics Letters*, **99**(8):082504, 2011. 56

[132] Markus Aichhorn, Silke Biermann, Takashi Miyake, Antoine Georges, and Masatoshi Imada. **Theoretical evidence for strong correlations and incoherent metallic state in FeSe**. *Phys. Rev. B*, **82**(6):064504, Aug 2010. 56, 69

[133] Hyungju Oh, Jisoo Moon, Donghan Shin, Chang-Youn Moon, and Hyoung Joon Choi. **Brief review on iron-based superconductors: are there clues for unconventional superconductivity?** *arXiv:1201.0237v1*. 69, 72, 76, 79

[134] L. Craco and S. Leoni. **Comparative study of tetragonal and hexagonal FeSe: An orbital-selective scenario**. *EPL (Europhysics Letters)*, **92**(6):67003, 2010. 69

[135] D.J. Singh and M.H. Du. **Density Functional Study of** $LaFeAsO_{1-x}F_x$**: A Low Carrier Density Superconductor Near Itinerant Magnetism**. *Phys. Rev. Lett.*, **100**:237003, Jun 2008. 69

[136] S. Lebègue. **Electronic structure and properties of the Fermi surface of the superconductor LaOFeP**. *Phys. Rev. B*, **75**:035110, Jan 2007.

[137] Chang Liu, Yongbin Lee, A. D. Palczewski, J.-Q. Yan, Takeshi Kondo, B. N. Harmon, R. W. McCallum, T. A. Lograsso, and A. Kaminski. **Surface-driven electronic structure in LaFeAsO**

studied by angle-resolved photoemission spectroscopy. *Phys. Rev. B*, **82**:075135, Aug 2010.

[138] D. H. Lu, M. Yi, S.-K. Mo, A. S. Erickson, J. Analytis, J.-H. Chu, D. J. Singh, Z. Hussain, T. H. Geballe, I. R. Fisher, and Z.-X. Shen. **Electronic structure of the iron-based superconductor LaOFeP**. *Nature*, **455**(7209):81–84, September 2008. 69

[139] Wei Li, Hao Ding, Peng Deng, Kai Chang, Canli Song, Ke He, Lili Wang, Xucun Ma, Jiang-Ping Hu, Xi Chen, and Qi-Kun Xue. **Phase separation and magnetic order in K-doped iron selenide superconductor**. *Nat Phys*, **8**(2):126–130, February 2012. 69

[140] Wang Qing-Yan, Li Zhi, Zhang Wen-Hao, Zhang Zuo-Cheng, Zhang Jin-Song, Li Wei, Ding Hao, Ou Yun-Bo, Deng Peng, Chang Kai, Wen Jing, Song Can-Li, He Ke, Jia Jin-Feng, Ji Shuai-Hua, Wang Ya-Yu, Wang Li-Li, Chen Xi, Ma Xu-Cun, and Xue Qi-Kun. **Interface-Induced High-Temperature Superconductivity in Single Unit-Cell FeSe Films on SrTiO 3**. *Chinese Physics Letters*, **29**(3):037402, 2012. 74

[141] Defa Liu, Wenhao Zhang, Daixiang Mou, Junfeng He, Yun-Bo Ou, Qing-Yan Wang, Zhi Li, Lili Wang, Lin Zhao, Shaolong He, Yingying Peng, Xu Liu, Chaoyu Chen, Li Yu, Guodong Liu, Xiaoli Dong, Jun Zhang, Chuangtian Chen, Zuyan Xu, Jiangping Hu, Xi Chen, Xucun Ma, Qikun Xue, and X.J. Zhou. **Electronic origin of high-temperature superconductivity in single-layer FeSe superconductor**. *Nat Commun*, **3**:931–, July 2012. 74, 79

[142] Shaolong He, Junfeng He, Defa Liu, Wenhao Zhang, Daixiang Mou, Yun-Bo Ou, Qing-Yan Wang, Zhi Li, Lili Wang, Lin Zhao, Shaolong He, Yingying Peng, Xu Liu, Chaoyu Chen, Li Yu, Guodong Liu, Xiaoli Dong, Jun Zhang, Chuangtian Chen, Zuyan Xu, Jiangping Hu, Xi Chen, Xucun Ma, Qikun Xue, and X.J. Zhou. **Phase Diagram and High Temperature Superconductivity at 65 K in Tuning Carrier Concentration of Single-Layer FeSe Films**. *arXiv:1207.6823v1.* 74, 76, 79

[143] Can-Li Song, Yi-Lin Wang, Ye-Ping Jiang, Lili Wang, Ke He, Xi Chen, Jennifer E Hoffman, Xu-Cun Ma, and Qi-Kun Xue. **Suppression of superconductivity by twin boundaries**. *arXiv:1203.2629v1.* 75

[144] Kai Liu, Zhong-Yi Lu, and Tao Xiang. **Atomic and electronic structures of FeSe monolayer and bilayer thin films on $SrTiO_3$**

(001): First-principles study. *Phys. Rev. B*, **85**:235123, Jun 2012. 75, 79

[145] Yuan-Yuan Xiang, Fa Wang, Da Wang, Qiang-Hua Wang, and Dung-Hai Lee. **High-temperature superconductivity at the FeSe/$SrTiO_3$ interface**. *Phys. Rev. B*, **86**:134508, Oct 2012. 75

[146] Timur Bazhirov and Marvin L. Cohen. **Spin-resolved electron-phonon coupling in FeSe and KFe_2Se_2**. *Phys. Rev. B*, **86**:134517, Oct 2012. 75, 84

[147] Daixiang Mou, Shanyu Liu, Xiaowen Jia, Junfeng He, Yingying Peng, Lin Zhao, Li Yu, Guodong Liu, Shaolong He, Xiaoli Dong, Jun Zhang, Hangdong Wang, Chiheng Dong, Minghu Fang, Xiaoyang Wang, Qinjun Peng, Zhimin Wang, Shenjin Zhang, Feng Yang, Zuyan Xu, Chuangtian Chen, and X. J. Zhou. **Distinct Fermi Surface Topology and Nodeless Superconducting Gap in a** $(Tl_{0.58}Rb_{0.42})Fe_{1.72}Se_2$ **Superconductor**. *Phys. Rev. Lett.*, **106**:107001, Mar 2011. 76

[148] T. Yildirim. **Strong Coupling of the Fe-Spin State and the As-As Hybridization in Iron-Pnictide Superconductors from First-Principle Calculations**. *Phys. Rev. Lett.*, **102**:037003, Jan 2009. 79

[149] A. Scholl, J. Stöhr, J. Lüning, J. W. Seo, J. Fompeyrine, H. Siegwart, J.-P. Locquet, F. Nolting, S. Anders, E. E. Fullerton, M. R. Scheinfein, and H. A. Padmore. **Observation of Antiferromagnetic Domains in Epitaxial Thin Films**. *Science*, **287**(5455):1014–1016, 2000. 79

[150] Lu Li, C. Richter, J. Mannhart, and R. C. Ashoori. **Coexistence of magnetic order and two-dimensional superconductivity at LaAlO3/SrTiO3 interfaces**. *Nat Phys*, **7**(10):762–766, October 2011. 79

[151] Fa Wang, Fan Yang, Miao Gao, Zhong-Yi Lu, Tao Xiang, and Dung-Hai Lee. **The electron pairing of K x Fe 2 y Se 2**. *EPL (Europhysics Letters)*, **93**(5):57003, 2011. 79, 81

[152] T. Dahm, V. Hinkov, S. V. Borisenko, A. A. Kordyuk, V. B. Zabolotnyy, J. Fink, B. Buechner, D. J. Scalapino, W. Hanke, and B. Keimer. *Nature Physics*, **5**:217, 2009. 83

[153] M. Le Tacon, G. Ghiringhelli, J. Chaloupka, M. Moretti Sala, V. Hinkov, M. W. Haverkort, M. Minola, M. Bakr, K. J. Zhou, S. Blanco-Canosa, C. Monney, Y. T. Song, G. L. Sun, C. T.

Lin, G. M. De Luca, M. Salluzzo, G. Khaliullin, T. Schmitt, L. Braicovich, and B. Keimer. *Nature Physics*, **7**:725, 2011.

[154] P. Monthoux, A. V. Balatsky, and D. Pines. *Phys. Rev. Lett.*, **67**:3448, 1991. 83

[155] D. J. Scalapino. *Rev. Mod. Phys.*, **84**:1383, 2012. 83

[156] K. Kuroki, S. Onari, R. Arita, H. Usui, Y. Tanaka, H. Kontani, and H. Aoki. *Phys. Rev. Lett.*, **101**:087004, 2008. 83

[157] S. Graser, A. F. Kemper, T. A. Maier, H.-P. Cheng, P. J. Hirschfeld, and D. J. Scalapino. *Phys. Rev. B*, **81**:214503, 2010. 83

[158] S. Doniach and S. Engelsberg. *Phys. Rev. Lett.*, **17**:750, 1966. 83

[159] N. F. Berk and J. R. Schrieffer. *Phys. Rev. Lett.*, **17**:433, 1966.

[160] J. R. Schrieffer. *Phys. Rev. Lett.*, **19**:644, 1967. 83

[161] A. Helmes, R. Grein, and M. Eschrig. *Phys. Rev. Lett.*, **106**:047003, 2011. 83

[162] E. Stenzel, H. Winter, Z. Szotek, and W. M. Temmerman. *Z. Phys. B - Condensed Matter*, **70**:173, 1988. 83

[163] E. Stenzel and H. Winter. *J. Phys. F: Met. Phys.*, **16**:1789, 1986. 83

[164] M. Springer, F. Aryasetiawan, and K. Karlsson. *Phys. Rev. Lett.*, **80**:2389, 1998. 83

[165] V. P. Zhukov, E. V. Chulkov, and P. M. Echenique. *Phys. Rev. Lett.*, **93**:096401, 2004.

[166] V. P. Zhukov, E. V. Chulkov, and P. M. Echenique. *Phys. Rev. B*, **72**:155109, 2005. 83

[167] F. Essenberger, P. Buczek, A. Ernst, L. Sandratskii, and E. K. U. Gross. **Paramagnons in FeSe close to a magnetic quantum phase transition: *Ab initio* study**. *Phys. Rev. B*, **86**:060412, Aug 2012. 83, 84

[168] Indirect evidence for strong coupling superconductivity in FeSe under pressure from first-principle calculations. **Superconductivity and Spin Fluctuations**. *arXiv:1210.2593v1*, 2012. 83, 84

[169] Timur Bazhirov, Yuki Sakai, Susumu Saito, and Marvin L. Cohen. **Importance of oxygen octahedra tilts for the electron-phonon coupling in K-doped $BaBiO_3$**. *under review at Phys. Rev. B.* 90

[170] R. J. Cava, B. Batlogg, J. J. Krajewski, R. Farrow, L. W. Rupp, A. E. White, K. Short, W. F. Peck, and T. Kometani. **Superconductivity near 30 K without copper: the Ba0.6K0.4BiO3 perovskite**. *Nature*, **332**(6167):814–816, Apr 1988. 91

[171] L. F. Mattheiss, E. M. Gyorgy, and D. W. Johnson. **Superconductivity above 20 K in the Ba-K-Bi-O system**. *Phys. Rev. B*, **37**:3745–3746, Mar 1988. 91, 97

[172] Shiyou Pei, J. D. Jorgensen, B. Dabrowski, D. G. Hinks, D. R. Richards, A. W. Mitchell, J. M. Newsam, S. K. Sinha, D. Vaknin, and A. J. Jacobson. **Structural phase diagram of the $Ba_{1-x}K_xBiO_3$ system**. *Phys. Rev. B*, **41**:4126–4141, Mar 1990. 91, 94

[173] Q. Huang, J. F. Zasadzinski, N. Tralshawala, K. E. Gray, D. G. Hinks, J. L. Peng, and R. L. Greene. **Tunnelling evidence for predominantly electron-phonon coupling in superconducting Ba1-xKxBiO3 and Nd2-xCexCuO4-y**. *Nature*, **347**(6291):369–372, Sep 1990. 91, 93, 97

[174] N. Tralshawala, J. F. Zasadzinski, L. Coffey, W. Gai, M. Romalis, Q. Huang, R. Vaglio, and K. E. Gray. **Tunneling, α^2 *F* (ω), and transport in superconductors: Nb, V, VN, Ba_{1-x} K_x BiO_3, and $Nd_{1.85}$ $Ce_{0.15}$ CuO_4**. *Phys. Rev. B*, **51**:3812–3819, Feb 1995. 91

[175] R. Kuentzler, C. Hornick, Y. Dossman, S. Wegner, R. El Farsi, and M. Drillon. **Superconductivity of Pb, K and Rb-doped BaBiO3**. *Physica C: Superconductivity*, **184**(4–6):316 – 320, 1991. 91

[176] L. F. Mattheiss and D. R. Hamann. **Electronic structure of $BaPb_{1-x}Bi_xO_3$**. *Phys. Rev. B*, **28**:4227–4241, Oct 1983. 91, 95

[177] L. F. Mattheiss and D. R. Hamann. **Electronic Structure of the High-T_c Superconductor $Ba_{1-x}K_xBiO_3$**. *Phys. Rev. Lett.*, **60**:2681–2684, Jun 1988. 95, 97

[178] C.-K. Loong, P. Vashishta, R. K. Kalia, M. H. Degani, D. L. Price, J. D. Jorgensen, D. G. Hinks, B. Dabrowski, A. W. Mitchell, D. R. Richards, and Y. Zheng. **High-energy oxygen phonon modes and superconductivity in $Ba_{1-x}K_xBiO_3$: An inelastic-neutron-scattering experiment and molecular-dynamics simulation**. *Phys. Rev. Lett.*, **62**:2628–2631, May 1989. 98

[179] C.-K. Loong, P. Vashishta, R. K. Kalia, Wei Jin, M. H. Degani, D. G. Hinks, D. L. Price, J. D. Jorgensen, B. Dabrowski, A. W. Mitchell, D. R. Richards, and Y. Zheng. **Phonon density of states and oxygen-isotope effect in** $Ba_{1-x}K_xBiO_3$. *Phys. Rev. B*, **45**:8052–8064, Apr 1992. 98

[180] M. Braden, W. Reichardt, W. Schmidbauer, A.S. Ivanov, and A.Yu. Rumiantsev. **Lattice dynamics of (Ba/K)BiO3**. *Journal of Superconductivity*, **8**(5):595–598, 1995.

[181] M. Braden, W. Reichardt, S. Shiryaev, and S.N. Barilo. **Giant phonon anomalies in the bond-stretching modes in doped BaBiO3: comparison to cuprates manganites and nickelates**. *Physica C: Superconductivity*, **378–381, Part 1**(0):89 – 96, 2002. 91

[182] D.E. Cox and A.W. Sleight. **Crystal structure of Ba2Bi3+Bi5+O6**. *Solid State Communications*, **19**(10):969 – 973, 1976. 91

[183] A. I. Liechtenstein, I. I. Mazin, C. O. Rodriguez, O. Jepsen, O. K. Andersen, and M. Methfessel. **Structural phase diagram and electron-phonon interaction in** $Ba_{1-x}K_xBiO_3$. *Phys. Rev. B*, **44**:5388–5391, Sep 1991. 91, 95, 97

[184] V. Meregalli and S. Y. Savrasov. **Electron-phonon coupling and properties of doped** $BaBiO_3$. *Phys. Rev. B*, **57**:14453–14469, Jun 1998. 91

[185] Karel Kunc and Roland Zeyher. **Electron-phonon coupling in** $Ba_{0.5}K_{0.5}BiO_3$**:** ***Ab initio*** **calculations of q = 0 phonons**. *Phys. Rev. B*, **49**:12216–12219, May 1994. 91

[186] C. Franchini, A. Sanna, M. Marsman, and G. Kresse. **Structural, vibrational, and quasiparticle properties of the Peierls semiconductor** $BaBiO_3$**: A hybrid functional and self-consistent GW + vertex-corrections study**. *Phys. Rev. B*, **81**:085213, Feb 2010. 91, 95, 97

[187] Z. P. Yin, A. Kutepov, and G. Kotliar. **Correlation-Enhanced Electron-Phonon Coupling: Applications of** GW **and Screened Hybrid Functional to Bismuthates, Chloronitrides, and Other High-**T_c **Superconductors**. *Phys. Rev. X*, **3**:021011, May 2013. 91, 92, 93, 100, 101

[188] Y Yacoby, S.M Heald, and E.A Stern. **Local oxygen octahedra rotations in Ba1xKxBiO3 and BaBiO3**. *Solid State Communications*, **101**(11):801 – 806, 1997. 92, 94

[189] L. F. Mattheiss and D. R. Hamann. **Electronic- and crystal-structure effects on superconductivity in the** $BaPb_{1-x}Bi_xO_3$ **system**. *Phys. Rev. B*, **26**:2686–2689, Sep 1982. 95

[190] A.W. Sleight, J.L. Gillson, and P.E. Bierstedt. **High-temperature superconductivity in the BaPb1-xBixO3 systems**. *Solid State Communications*, **17**(1):27 – 28, 1975. 95

[191] Antoine Georges, Gabriel Kotliar, Werner Krauth, and Marcelo J. Rozenberg. **Dynamical mean-field theory of strongly correlated fermion systems and the limit of infinite dimensions**. *Rev. Mod. Phys.*, **68**:13–125, Jan 1996. 103

[192] Carina Faber, Jonathan Laflamme Janssen, Michel Côté, E. Runge, and X. Blase. **Electron-phonon coupling in the** C_{60} **fullerene within the many-body** *GW* **approach**. *Phys. Rev. B*, **84**:155104, Oct 2011. 103

[193] Amy Y. Liu, I. I. Mazin, and Jens Kortus. **Beyond Eliashberg Superconductivity in** $MgB2$**: Anharmonicity, Two-Phonon Scattering, and Multiple Gaps**. *Phys. Rev. Lett.*, **87**(8):087005, Aug 2001. 103

[194] Hyoung Joon Choi, David Roundy, Hong Sun, Marvin L. Cohen, and Steven G. Louie. **First-principles calculation of the superconducting transition in** MgB_2 **within the anisotropic Eliashberg formalism**. *Phys. Rev. B*, **66**:020513, Jul 2002. 103

[195] Anubhav Jain, Shyue Ping Ong, Geoffroy Hautier, Wei Chen, William Davidson Richards, Stephen Dacek, Shreyas Cholia, Dan Gunter, David Skinner, Gerbrand Ceder, and Kristin A. Persson. **Commentary: The Materials Project: A materials genome approach to accelerating materials innovation**. *APL Materials*, **1**(1):–, 2013. 105